Using Satellite Observations to Address Power Asymmetries in Transboundary River Basins

Submitted by

VU Trung Dung

Thesis Advisor

Dr. Stefano GALELLI

Engineering Systems and Design

A thesis submitted to the Singapore University of Technology and Design in fulfillment of the requirement for the degree of Doctor of Philosophy

2023

PhD Thesis Examination Committee

TEC Chair:	Prof. Bikramjit Das
Main Advisor:	Prof. Stefano Galelli
Internal TEC member 1:	Prof. Lynette Cheah
Internal TEC member 2:	Prof. Nuno Ribeiro

Abstract

Engineering Systems and Design

Doctor of Philosophy

Using Satellite Observations to Address Power Asymmetries in Transboundary River Basins

by VU Trung Dung

Half of the world's land surface is covered by about 300 transboundary river basins. In many of these areas, different views on infrastructure development and management tend to result in conflicting dynamics between riparian countries, even when international water agreements are signed. Because of the natural power asymmetry between upstream and downstream countries, the socio-economic externalities of these power struggles are often sustained by the riparian communities located in the most downstream areas. Such dynamics are typically compounded by the lack of transparency on how major infrastructures are operated. In most basins, for example, there are no shared platforms providing a detailed accounting of the amount of water stored and released by large dams. An opportunity to address the problem stands in satellite observations, which provide a means to monitor the actual state of rivers and big infrastructure.

Here, we turn our attention to the Mekong River Basin—the largest transboundary river basin in Southeast Asia—where the situation of power asymmetry is emblematic of the issues faced by many transboundary basins around the world. We look, in particular, at three problems. In the first one, we leverage satellite observations to infer dam storage variations and operating rules. Specifically, we use area-storage curves (derived from a digital elevation model) and time series of reservoir water surface area, which we estimate from Landsat satellite images through a novel algorithm that removes the effects of clouds and other disturbances. In the second problem, we improve the reliability of macro-scale hydrological models by making use of the inferred reservoir operations—a highly important, but often missing, element in river basin models. we couple our hydrological model with a hydraulic model used to infer discharge time series from satellite altimetry data. With the aid of Global Sensitivity Analysis, we propose an approach to avoid the pitfall occurring when co-calibrating the two models. Finally, using the output of the two first parts (reservoir operation patterns and calibrated hydrological model), we assess the impacts on the downstream areas of the impoundment of upstream reservoirs and also use a numerical framework to devise better filling strategies for those reservoirs. The data and approaches developed in this thesis will help enrich the existing tools for water resources monitoring and management in transboundary river basins.

Publications

Journal Papers

Vu, D. T., Dang, T. D., Galelli, S., & Hossain, F. (2022). Satellite observations reveal 13 years of reservoir filling strategies, operating rules, and hydrological alterations in the Upper Mekong River basin. *Hydrology and Earth System Sciences 26*(9), 2345–2364. https://doi.org/10.5194/hess-26-2345-2022.

Vu, D. T., Dang, T. D., Pianosi, F., & Galelli, S. (2023). Calibrating macro-scale hydrological models in poorly gauged and heavily regulated basins. *Hydrology and Earth System Sciences Discussion*. https://doi.org/10.5194/hess-2023-35.

Conference Presentations

Vu, D. T., Dang, T. D., & Galelli, S. (2020). How much water is withheld in the Upper Mekong's hydropower dams?. *AGU Fall Meeting 2020*, H011-0016, 1-17 December 2020, Online.

Vu, D. T., Dang, T. D., & Galelli, S. (2021). Using space observations to monitor reservoir operations in the Lancang River. *EGU General Assembly 2021*, EGU21-8615, 19–30 April 2021, Online.

Vu, D. T., Dang, T. D., & Galelli, S. (2022). Improving the reliability of large-scale hydrological models with satellite observations. *EGU General Assembly 2022*, EGU22-481, 23-27 May 2022, Vienna, Austria.

Vu, D. T., Dang, T. D., & Galelli, S. (2022). Using satellite data to calibrate large-scale hydrological models in poorly-gauged and heavily-regulated basins. *AGU Fall Meeting 2022*, H32G-04, 12-16 December 2022, Chicago, IL, USA.

Codes

Vu, D. T. (2022). Py_Curve, Py_Mask, and Py_WSA. *Zenodo*, https://doi.org/10.5281/zenodo.6299041.

Data

Vu, D. T. (2022). E-A-S curves and monthly storage volume of 10 large dams on the Upper Mekong River. *Zenodo*, https://doi.org/10.5281/zenodo.6299041.

Related Publications

Dang, T. D., **Vu, D. T.**, Chowdhury, A. K., & Galelli, S. (2020). A software package for the representation and optimization of water reservoir operations in the VIC hydrologic model. *Environmental Modelling & Software 126*, 104673. https://doi.org/10.1016/j.envsoft.2020.104673.

Vu, D. T., Dang, T. D., & Galelli, S. (2018). Reservoir regulation could significantly influence flooding dynamics in the Chao Phraya delta. *AOGS 16th Annual Meeting*, HS02-A008, 28 July-2 August 2018, Singapore.

Acknowledgements

Conquering a PhD has been a challenging experience for me and it would not have been possible to do it without the guidance and support that I have received from many people.

First and foremost, I am extremely grateful to my advisor, Prof. Stefano Galelli for his valuable advice, continuous support, and encouragement during my 5-year PhD journey. I consider myself very lucky to have him as my PhD advisor who is always supportive and understanding. Words cannot express my gratitude to him for always being a great advisor.

I would like to express my appreciation to my Thesis Examination Committee: Prof. Bikramjit Das, Prof. Lynette Cheah, and Prof. Nuno Ribeiro for their enthusiastic involvement and insightful feedback. The valuable inputs from my Thesis Examination Committee helped me complete my PhD Thesis.

I would like to extend my sincere thanks to everyone I have collaborated with during my PhD. I am so grateful to Dr. Dang Duc Thanh (former researcher in our Resilient Water Systems Group at SUTD), Prof. Faisal Hossain (University of Washington), and Dr. Francesca Pianosi (University of Bristol) for their wonderful contributions to my publications—parts of my PhD Thesis. I am also thankful to the Professors and colleagues in the Water Development Research Group (Aalto University) and SASWE Research Group (University of Washington) for the fruitful meetings and discussions during my visiting trips—a part of my PhD program.

I gratefully acknowledge the funding received towards my PhD program from the SUTD PhD Fellowship. It has been an honor to be awarded the fellowship, which enables me to pursue my PhD without worrying about finances.

I would like to give special thanks to my two buddies in SUTD: Rachel Koh and Jin Xing Lim for walking with me on both sunny and rainy days of my PhD journey. Thanks for cheering me up when I was feeling down and making my PhD joyful and memorable. I also would like to thank my all friends who give me encouragement and entertainment after stressful studying and researching hours.

Lastly, I would be remiss in not mentioning my family. Heartfelt thanks go to my parents for their unstoppable support, to my sister and brother for taking good care of our parents when I was not around, busy with my studying, and to all members of my extended family for their encouragement. Their belief in me has kept my spirits and motivation high to overcome the challenges of my PhD.

Contents

List of Figures

List of Tables

Chapter 1

Introduction

1.1 Power asymmetries in transboundary river basins

Transboundary river basins

Transboundary river basins—sometimes referred to as international river basins—are river basins shared by two or more countries (e.g, the Colorado River Basin is shared by 2 countries, the United States and Mexico, while the Danube River Basin is shared by 19 European countries). By this definition, nearly one-half of the world's land surface is covered by more than 300 transboundary river basins, which are shared by about 150 countries (McCracken and Wolf, 2019) (see Fig. 1.1). These international rivers contribute up to 60 % of the global river flow and support the lives and livelihoods of an enormous number of people—approximately 40 % of the world's population (Wolf, Kramer, et al., 2005).

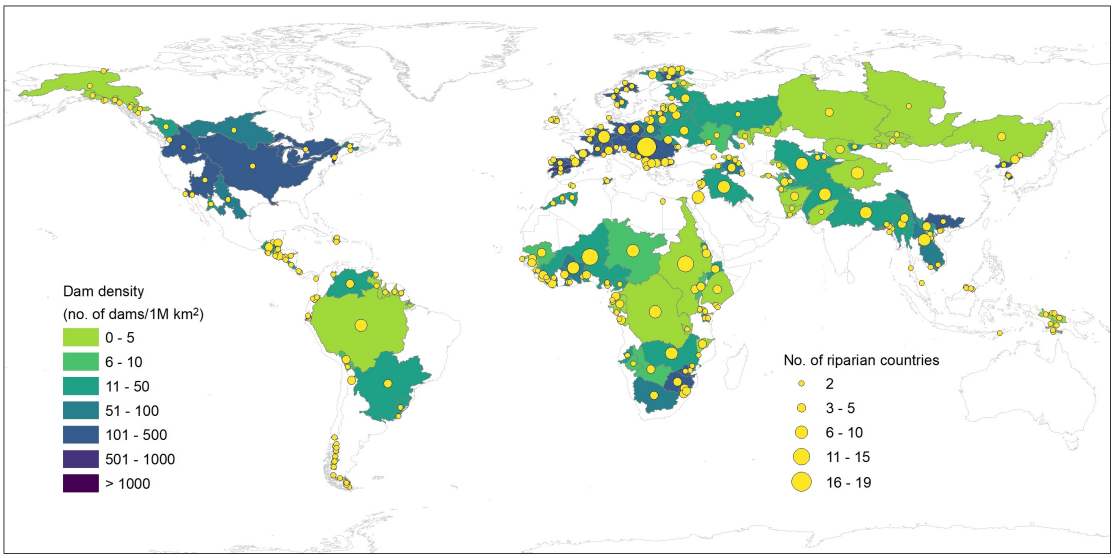

FIGURE 1.1: Transboundary river basins around the world. 311 transboundary river basins cover nearly one-half of the world's land surface and are shared by ∼150 countries. The dot size demonstrates the number of riparian countries, while the color scheme illustrates the dam density (number of dams per 1 million km^2) in each basin. Data were retrieved from McCracken and Wolf (2019).

Conflicts between riparian countries in transboundary river basins

The shared water resource from transboundary rivers is a potential source of conflicts, even leading to wars between riparian countries. Indeed, there were 1831 international water conflict cases reported during the period from 1950 to 2000 (Wolf, Stahl, and Macomber, 2003). The recent international water conflicts include those among 11 African countries (Kenya, Tanzania, the Democratic Republic of the Congo, Burundi, Rwanda, Uganda, South Sudan, Ethiopia, Eritrea, Sudan, and Egypt) over the Nile River (Abtew and Melesse, 2014), among China and 5 Southeast Asian countries (Myanmar, Thailand, Laos, Cambodia, and Vietnam) over the Mekong River (Pearse-Smith, 2014), among Turkey, Syria, and Iraq over the Euphrates-Tigris River (Hipel, Kilgour, and Kinsara, 2019), between Afghanistan and Iran over the Helmand River and the Harirud River (Amini et al., 2021), and so forth. Under the impacts of global warming (climate change), the changes in precipitation patterns and increase in evapotranspiration result in the decline in water availability in many parts of the world including transboundary river basins (Ambec, Dinar, and McKinney, 2013). At the same time, the growth of the population and economy leads to increased water demand (e.g., irrigation, hydropower production, domestic and industrial uses). These two factors, put together, could escalate the conflicts and disputes between riparian countries in transboundary river basins.

International water agreements

To reduce the likelihood of international water conflicts and also resolve existing disputes between riparian countries in transboundary river basins, the international community and intergovernmental organizations have been constructing principles for international watercourse management. The main principles consist of the equitable and reasonable utilization rule, the no-harm rule (the utilization of transboundary water in each riparian country must not harm other riparian countries), and the duty to cooperate including regular data exchanges between riparian countries (Mager, 2015). Unfortunately, it is difficult to implement such principles because of the complexity created by different locations, climates, ecosystems, economies, politics, cultures, and points of view on the use of common water sources of riparian countries (Petersen-Perlman, Veilleux, and Wolf, 2017). For example, the Convention on the Law of the Non-Navigational Uses of International Watercourses—referred to as the UN Watercourses Convention—was voted in favor by 103 countries in the General Assembly of the United Nations in 1997 (UNEP, 2002), but until now, only 40 countries have signed or consented to be bound by the agreement (UN, 2023). In the meantime, transboundary basin communities also have been building their own water treaties. However, the same difficulty is found in the implementation of those treaties. For instance, China—located in the most upstream of many transboundary rivers (e.g, the Indus, Ganges-Brahmaputra-Meghna, and Mekong rivers)—has not signed any comprehensive treaties of transboundary river basins which this country shares with other riparian countries (UN, n.d.).

Hydropower development in transboundary river basins

Despite the efforts of international and basin communities in devising international water agreements and the likelihood of escalation of conflicts and disputes over shared water resources, many countries have been constructing a huge number of hydropower dams on transboundary rivers to meet their growing electricity demand (Llamosas and Sovacool, 2021; Ly, Metternicht, and Marshall, 2022). As can be seen in Fig. 1.1, in many regions in the world such as North America, Europe, South Africa, and Southeast Asia, transboundary rivers have been heavily exploited for hydropower with a high dam density (> 50 dams per 1 million km^2). A closer look at Southeast Asia (Fig. 1.2) shows us the dense hydropower dam systems in all 4 transboundary river basins of this region (The Red River, Mekong, Salween, and Irrawaddy basins—all originating from the South of China. But it does not end here, another large number of hydropower dams is planned to join the fleet of the Mekong, Salween, and Irrawaddy basins (WLE Mekong, 2016; Schmitt et al., 2019).

Challenges in downstream countries

Power asymmetries between riparian countries—upstream countries naturally have the first access to the shared water source, affecting the flow to downstream countries—always exist in transboundary river basins. That factor along with the different points of view of riparian countries on how the transboundary water should be used and how the infrastructures on the river (e.g., hydropower dams) should be developed and managed result in the environmental and socio-economic impacts often witnessed in the riparian communities located in the most downstream areas (Warner and Zawahri, 2012). Such conflicting dynamics are typically compounded by the lack of transparency on how major infrastructures are operated. For example, there are no shared platforms providing a detailed accounting of the amount of water stored (and released) by large dams. With more hydropower dams planned to be built upstream of transboundary river basins, the downstream countries become more dependent on the flow from upstream and passive in managing their water resources due to the lack of data.

1.2 Satellite observations

Satellite observations have a wide range of applications and have been used for decades in the Earth's surface sciences. In water resources research and management, satellite observations could be used as direct or indirect measurements of most components of the hydrological cycle (e.g., precipitation, evapotranspiration, water surface extent and level of rivers and reservoirs/lakes, land surface elevation, land cover, soil moisture, etc.) (Lettenmaier et al., 2015; McCabe et al., 2017). This source of data is considered a supplement to in situ data. However, in ungauged regions or regions with no access to in situ data (e.g., in many transboundary river basins, data are not shared among riparian countries), satellite data are the only available source (Sheffield et al., 2018).

There are 3 main groups of satellite data that are popularly used in water resources research. The first and most common group is satellite images which can be used to

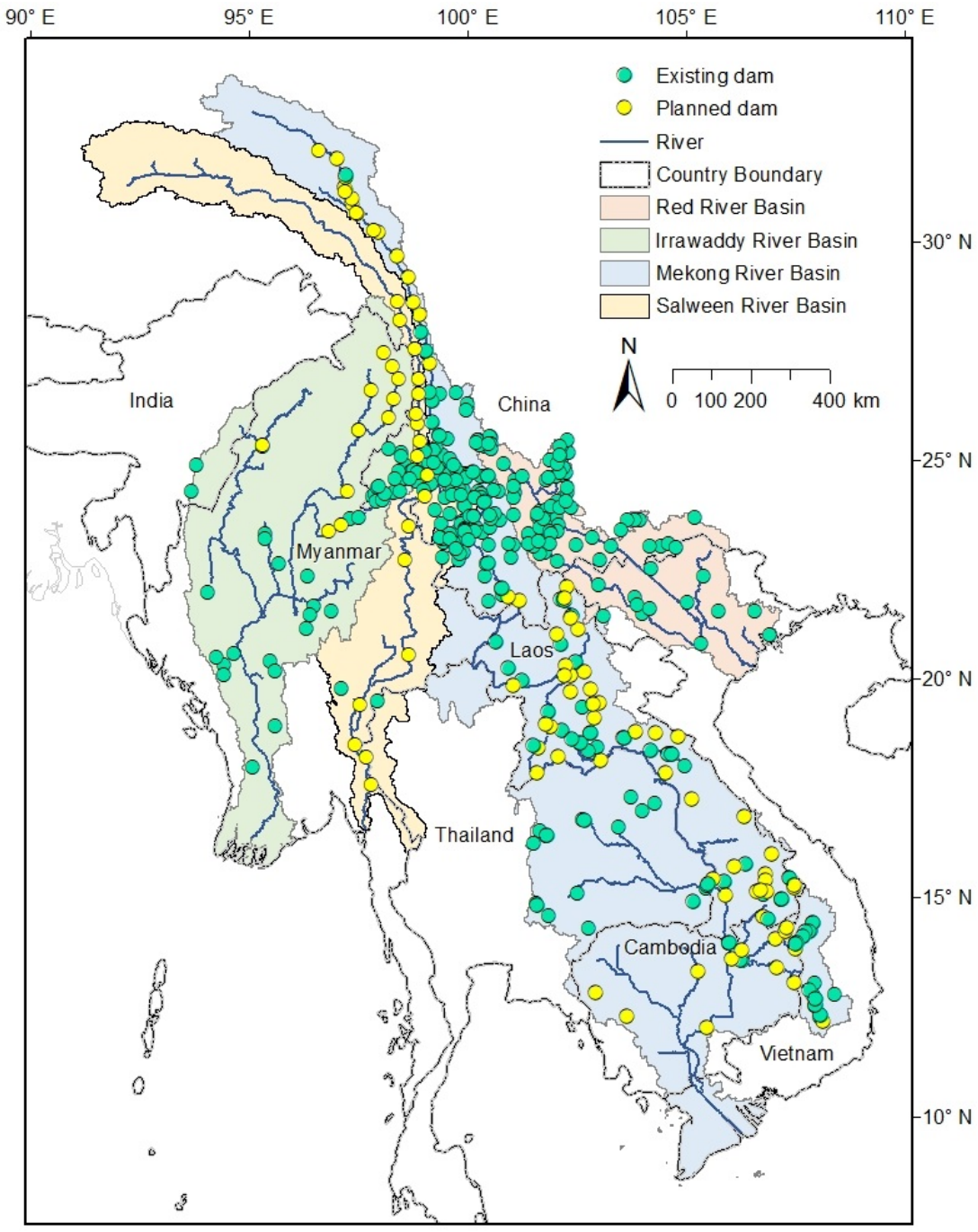

FIGURE 1.2: Hydropower development in the transboundary river basins of Southeast Asia. Data were retrieved from WLE Mekong (2016), Schmitt et al. (2019), and Wang et al. (2022).

identify the extent of objects on the Earth's surface (e.g., rivers, lakes, forests, etc.). Satellite images can be captured by optical sensors (like ordinary cameras) or Synthetic Aperture Radar (SAR) sensors (Flores-Anderson et al., 2019). Optical sensors have been used to collect images of the Earth's surface from satellites for more than 50 years. For

example, the first Landsat satellite—jointly built by the National Aeronautics and Space Administration of the U.S. (NASA) and the United States Geological Survey (USGS)—was launched in 1972. Since optical sensors use different wavelengths and collect their reflectance on the surface of objects, these sensors can provide colored (multispectral) images by synthesizing images captured by different wavelength bands, but they cannot provide information under clouds (Bevington et al., 2018). Meanwhile, SAR sensors that use radio waves to penetrate clouds can provide cloudless images. Nevertheless, SAR sensors have just been used recently (e.g., Sentinel 1 SAR was first launched by the European Space Agency (ESA) in 2014), which could be a limitation if a long observation (in the past) is required. Other specifications that determine the usability of satellite images are spatial and temporal resolutions. For instance, Moderate Resolution Imaging Spectroradiometer (MODIS) images (by NASA) have a high temporal resolution (daily) but a low spatial resolution of 250 m (Salomonson, Barnes, and Masuoka, 2006), while Landsat images have a lower temporal resolution (16 days) but a higher spatial resolution (30 m) (Bevington et al., 2018). In Fig. 1.3a-c, we illustrate an example of satellite images (i.e., Landsat 8). Panel a shows the grid of Landsat 8 images with ∼185 m x ∼170 m tiles. Panel b is a Landsat 8 image tile in natural color band combination, and panel c is a closer look where we can see 30 m x 30 m water (dark blue) and non-water pixels. We provide information on the specifications of the most common and free-accessible satellite images in Table 1.1.

The second group is satellite altimetry data which can provide information on the level of water surface (oceans, rivers, reservoirs, and lakes). Satellite altimeters estimate the elevation of objects from the traveling time of the wave pulses transmitted from satellites, reflected by the surface of objects and back to satellites. Altimeters used in this sort of mission can be either radar altimeters (e.g., Jason, Envisat, and Sentinel 3) (Vignudelli et al., 2019) or laser altimeters (e.g., ICESat) (Ryan et al., 2020). Unfortunately, satellite radar altimeters have sparse spatial coverage. For example, Jason altimetry data—a product of the National Centre for Space Studies of France (CNES) and NASA—only can be produced for water bodies that are larger than 350 m along the satellite ground track (Markert et al., 2019), which makes it not applicable to small reservoirs and narrow rives. On the other hand, satellite laser altimeters have a long revisit time. For instance, the ICESat series (by NASA) has a return period of 91 days. In Fig. 1.3e-f, we demonstrate an example of satellite altimetry data (i.e., Jason 2). Panel e shows the ground track of satellite Jason 2, and panel f shows a location (Xiaowan Reservoir in the Upper Mekong River) where Jason 2 altimetry data are available. We provide information on the specifications of the most common and free-accessible altimetry data in Table 1.1.

The last group is represented by digital elevation models (DEMs), also known as three-dimensional elevation maps. DEMs can provide information on the topography of river basins, and partial bathymetry of rivers and reservoirs. DEMs can be produced by using satellite radars to measure land elevations (e.g., the Shuttle Radar Topography Mission (SRTM) mission of NASA collected data for a near-global coverage from 11 - 22 February 2000 (USGS, 2009)) or combining information from different optical satellite images of the same object captured from different angles (e.g., the Japan Aerospace

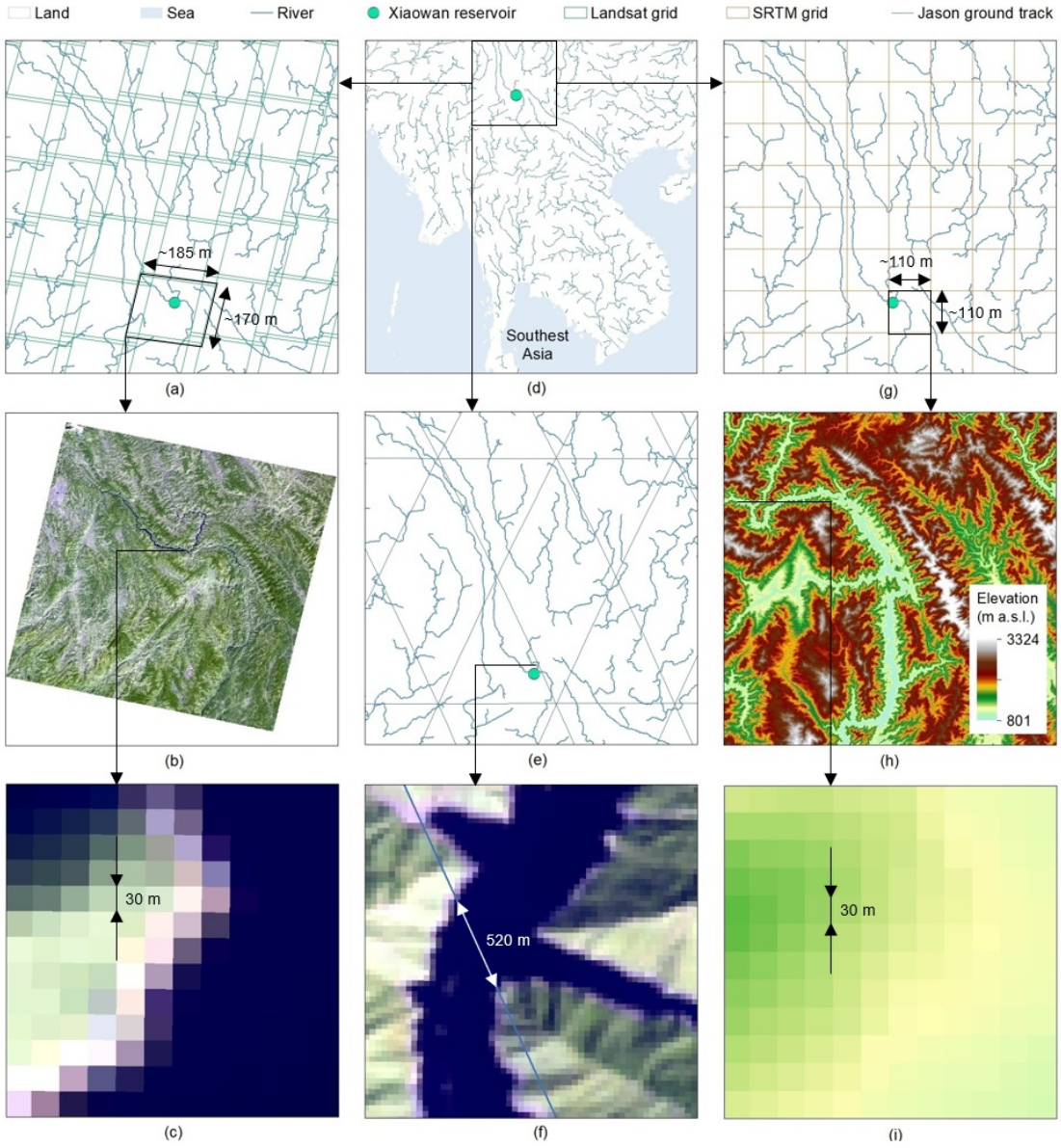

FIGURE 1.3: Examples of satellite images (Landsat 8) (a-c), altimetry data (Jason 2) (e-f), and digital elevation models (SRTM-DEM) (g-i). Panel a illustrates the grid of Landsat 8 images; panel b is a Landsat 8 image tile (∼185 m x ∼175 m) in natural color band combination, and panel c is a closer look where we can see water (dark blue) and non-water pixels (30 m x 30 m). Panel e displays the ground track of satellite Jason 2, and panel f shows a location (Xiaowan Reservoir in the Upper Mekong River) where Jason 2 altimetry data are available. Panel g demonstrates the grid of SRTM-DEM (1 arc-second); panel h is an SRTM-DEM (1 arc-second) tile (∼110 m x ∼110 m) with the color scheme representing the value of elevation (m a.s.l.), and panel i is a closer look where we can see 30 m x 30 m pixels.

TABLE 1.1: Categorization and specifications of the most popular and free-accessible satellite data.

Category		Satellite	Organization	Best spatial resolution	Temporal resolution	Operation period
Imagery	Optical	Landsat 1-3	NASA/USGS	60 m	16 days	1972-1983
		Landsat 4-5	NASA/USGS	30 m	16 days	1982-2013
		Landsat 7	NASA/USGS	30 m	16 days	1999-2022
		Landsat 8-9	NASA/USGS	30 m	16 days	2013-now
		MODIS	NASA	250 m	1 day	1999-now
		Sentinel 2	ESA	10 m	10 days	2015-now
		Sentinel 3	ESA	300 m	27 days	2016-now
	SAR	Sentinel 1	ESA	5 m	12 days	2014-2021
Altimetry	Radar	Topex/Poseidon	NASA/CNES	n/a	10 days	1992-2002
		Jason 1-3	NASA/CNES	n/a	10 days	2002-now
		ERS 1-2	ESA	n/a	35 days	1992-2003
		Envisat	ESA	n/a	35 days	2002-2010
		Sentinel 3A/B	ESA	n/a	27 days	2016-now
	Laser	ICESat 1-2	NASA	n/a	91 days	2003-now
DEM		SRTM	NASA	30 m	n/a	11-22/2 2000
		ALOS	JAXA	30 m	n/a	2006-2011

Exploration Agency (JAXA) created ALOS DEM from 3 million satellite images taken from 2006 to 2011 (Tadono et al., 2015)). Regardless of the method used, current free-accessible DEMs have a typical limitation that they cannot provide information under the water surface at the observation time. In Fig. 1.3g-i, we illustrate an example of digital elevation models (i.e., SRTM-DEM). Panel g shows the grid of SRTM-DEM (1 arc-second) with ∼110 m x ∼110 m tiles. Panel h is an SRTM-DEM (1 arc-second) tile with the color scheme representing the value of elevation (m a.s.l.), and panel i is a closer look where we can see 30 m x 30 m pixels. Find the specifications of the most common and free-accessible DEMs in Table 1.1.

Satellite data seem to be the most efficient and economical solution to address the problem of data shortage in downstream countries in transboundary river basins. However, as mentioned above, each type of satellite data has its own limitations (spatial-temporal coverage and resolution, cloud cover, and other disturbances), meaning that they cannot be used directly. Therefore, it is necessary to develop new techniques to surmount those limitations and optimize the use of this data source.

1.3 Contributions of this thesis

With a desire to address power asymmetries in transboundary river basins, in this thesis, we contribute novel methodologies to infer important information from satellite data and use those data efficiently in water resources management of the downstream communities, as well as the entire basin). Specifically, we first develop a method to derive the operations of reservoirs using satellite data. Then, we introduce a new approach, again leveraging satellite data, to calibrate hydrological models for estimating the streamflow data. The reliability of our model is improved by the inferred reservoir operations, a highly important, but often missing, element in river basin models. Finally, using the outcome of the two first parts, we evaluate the filling strategy of reservoirs upstream and also use a numerical framework to devise better filling strategies for those reservoirs. We apply our work to the Mekong River Basin where the situation of power asymmetry is emblematic of the issues faced by many transboundary basins around the world.

In Chapter 2, we leverage satellite observations to infer a 13-year time series of monthly storage variations of the 10 largest reservoirs on the mainstream of the Upper Mekong River—known as the Lancang River. In particular, we use the relationship between reservoir water level and storage volume (estimated from a digital elevation model) and time series of reservoir water surface area, which we calculated from Landsat satellite images by using a novel algorithm that removes the effects of clouds and other disturbances. We again leverage satellite radar altimetry water level data (Jason and Sentinel-3) to validate the results derived from satellite imagery for the reservoirs where altimetry water level data are available.

In Chapter 3, we couple VIC-Res (a macro-scale hydrological model setup for the Upper Mekong River Basin including the inferred reservoir operations from Chapter 2—a highly important, but often missing, element in river basin models) with a hydraulic model (based on Manning's equation) used to infer discharge time series from satellite altimetry data. Using Global Sensitivity Analysis, we find the existence of a strong relationship between the parameterization of the hydraulic model and the modeling accuracy of VIC-Res represented by a set of performance metrics we consider. The results of the sensitivity analysis help us to constrain the parameter of the hydraulic model. Finally, we carry out a calibration exercise for the hydrological model with the aid of a multi-objective optimization algorithm.

In Chapter 4, we use a simulation-optimization approach, which includes a hydrological model (VIC-Res in Chapter 3) and a multi-objective evolutionary algorithm (ε-NSGA-II) to optimize the filling strategy for the Lancang dam system. By parameterizing the filling strategy, and changing the parameters in their feasible ranges with the aid of ε-NSGA-II, we explore a large number of alternative filling strategies. Comparing the historical filling strategy (inferred from satellite data in Chapter 2) against the optimal filling strategies resulted from our experiment, we show how good/balanced the historical filling strategy is and how much upstream and downstream countries would have gained and lost if the more balanced filling strategies were used instead of

the actual strategy.

Finally, in Chapter 5, we conclude this thesis by summarizing the results of using satellite observations to address power asymmetries in transboundary river basins and discussing the future work that we can develop from this thesis.

Chapter 2

Satellite observations reveal thirteen years of reservoir filling strategies, operating rules, and hydrological alterations in the Upper Mekong River Basin

Publication

Vu, D. T., Dang, T. D., Galelli, S., & Hossain, F. (2022). Satellite observations reveal 13 years of reservoir filling strategies, operating rules, and hydrological alterations in the Upper Mekong River basin. *Hydrology and Earth System Sciences 26*(9), 2345–2364. https://doi.org/10.5194/hess-26-2345-2022.

2.1 Introduction

In many transboundary river basins, conflicting dynamics between riparian countries are typically the result of different views on infrastructure development and management (Warner and Zawahri, 2012). Such dynamics are often compounded by the lack of transparency on how major infrastructure, such as dams, is operated. The situation in the Lancang-Mekong River basin is no exception: during the past 3 decades, the basin has witnessed a rapid development of its hydropower fleet (Chowdhury, Dang, Hung T. T. Nguyen, et al., 2021), which has altered the hydrological regime (Dang, Cochrane, et al., 2016; Räsänen et al., 2017) and changed the sediment budget (Kondolf et al., 2018; Binh, Kantoush, and Sumi, 2020), thereby degrading riverine ecosystems and threatening riparian communities (Sabo et al., 2017; Soukhaphon, Baird, and Hogan, 2021). In turn, these profound and ramified changes have challenged the relation between riparian countries (Wei et al., 2021). In this water-energy management "mishmash", China plays a critical role. First, the river originates in the Tibetan Plateau and flows within the Chinese borders for about 2000 km, creating a natural power asymmetry with the other riparian countries (Kattelus et al., 2015). Second, China has built a limited number of dams—only 11 out of the 100 or more that currently punctuate the entire basin (Hecht et al., 2019). Yet, these few dams in the Upper Mekong River, or Lancang, have massive storage capacity ($\sim$42 km^3) and control a sizeable portion of the river discharge

(about 55 % of the average annual flow measured in Northern Thailand). Third, China has participated fairly weakly in transboundary water cooperation efforts, prioritizing bilateral cooperation to multi-country engagements, such as the Mekong River Commission (Kattelus et al., 2015; Williams, 2020). Fourth, China has yet to share detailed and comprehensive data on dam operations; agreements on data sharing and quality control are only at their infancy (Johnson, 2020). For these reasons, the Lancang's dams have become a source of controversy between China and downstream countries (IRN, 2002; Eyler and Weatherby, 2020; Kallio and Fallon, 2020). But to assess their actual impact and inform cooperative efforts, we must first quantify and understand how these dams have been operated.

There are at least two approaches available to tackle this challenge. The first one builds on the idea of generating data on reservoir inflow, storage, and release via simulation with a process-based hydrological-water management model, a solution recently explored for the Mekong Basin by Dang, Chowdhury, and Galelli (2020), Yun et al. (2020), and Shin et al. (2020). Naturally, this is only a partial fix, since the simulation of water reservoir storage and operations still requires some basic information on design specifications and operational strategies. The second approach relies on satellite remote sensing, which provides a means to directly observe a few key variables. Satellite altimeters, for example, provide high-resolution water level data of lakes and reservoirs (Schwatke et al., 2015; Busker et al., 2019; Biswas, F. Hossain, Bonnema, Okeowo, et al., 2019), while optical satellite images can be processed to map and detect changes in water surface area (Pekel et al., 2016; Zhao and Huilin Gao, 2018; Pickens et al., 2020). Moreover, data on water level and area can be combined with information on bathymetry (e.g., elevation–area curve) to infer the storage time series (see the review by Huilin Gao (2015)). The widespread availability of satellite data has indeed sparked research on monitoring of reservoir operations in several ungauged basins across the globe (Huilin Gao, C. Birkett, and Lettenmaier, 2012; Duan and Bastiaanssen, 2013; Bonnema, Sikder, et al., 2016; Busker et al., 2019), including the Mekong River Basin. For example, K.-T. Liu et al. (2016) used satellite radar altimetry and Landsat images to estimate the water level of two reservoirs in the Lancang (Xiaowan and Jinghong) for the period 2000–2015. Their analysis was limited to cloudless Landsat images, so the time series derived this way have an irregular temporal resolution. Shortly after, Bonnema and F. Hossain (2017) and Bonnema and F. Hossain (2019) estimated reservoir storage change for several sites of the Mekong, focusing primarily on its lower reaches.

Importantly, the aforementioned approaches and data have started to find their way into decision support systems used by the Lower Mekong countries. A first example is the Mekong Dam Monitor, an online platform for near real-time monitoring of dams developed by the Stimson Center and Eyes on Earth (`https://www.stimson.org/project/mekong-dam-monitor/`, last access: 20 January 2022). Specifically, the platform uses Sentinel 1 and 2 images to provide weekly updates of water level in the 13 dams built on the main stem—plus 14 additional reservoirs on the river tributaries (Eyler, Basist, et al., 2020). Because Sentinel 1 and 2 were launched in April 2014 and June 2015, respectively, the available time series are relatively short and do not include the filling period of the two largest reservoirs in Lancang, Nuozhadu and

Xiaowan (for additional details on the difference between the methodology used in this study and the one adopted by the Mekong Dam Monitor, please refer to Text A.1 in Appx. A). Another example is the Reservoir Assessment Tool (RAT, https://depts.washington.edu/saswe/rat_beta/, last access: 20 January 2022), an online tool for near-real-time monitoring and impact analysis of existing and planned reservoirs (Biswas, F. Hossain, Bonnema, Lee, et al., 2021). RAT uses Landsat 5 and 8 images to monitor ∼1500 reservoirs in South America, Africa, and Southeast Asia, including six in the Lancang River basin.

Notwithstanding these recent advances, a deeper understanding of dam operations in the Lancang River basin is needed to inform the downstream countries and seek cooperative solutions spanning across the entire basin. A first complexity is the lack of water level and storage time series (for each reservoir in the Lancang Basin) with adequate temporal resolution and horizon—ideally, each time series should have at least a data point per month and cover the entire life span of a given dam. Here, an important challenge lies with data availability: Landsat images are available for almost any reservoir and span more than 3 decades but are affected by clouds (Busker et al., 2019; Biswas, F. Hossain, Bonnema, Lee, et al., 2021), thereby requiring an image enhancement process (Huilin Gao, C. Birkett, and Lettenmaier, 2012; S. Zhang, Huilin Gao, and Naz, 2014; Avisse et al., 2017). Conversely, satellite altimeter observations are less subject to external disturbances. However, they either have sparse spatial coverage (satellite radar altimeters)—data are not available for all reservoirs due to their narrow ground track and orbit—or have a long revisit time (satellite laser altimeters). The ICESat series (satellite laser altimeters), for example, has a 91 d return period. Second, we need to discover the filling strategy of these dams, that is, the rate at which they have been filled. Unveiling these strategies could help understand past changes in downstream water availability and prepare contingency plans, since China is planning to build 10 more dams in the Lancang (MRC, 2020a). Third, the availability of monthly storage data is the prerequisite for any event attribution analysis on droughts and pluvials. In other words, detailed information on the operations of the Lancang's dams could help us explain whether or how they contributed to recent extreme events (Keovilignavong, T. H. Nguyen, and Hirsch, 2021).

In this study, we address the three knowledge gaps described above. To this purpose, we rely on a 30 m digital elevation model (DEM) from the Shuttle Radar Topography Mission (SRTM), satellite imagery (Landsat 5, 7, and 8), and altimetry water level data (Jason and Sentinel-3) (Sect. 2.2). particular, we use the DEM data to identify the elevation–storage and area–storage curves and process the Landsat images to generate monthly time series of water surface area for each reservoir. In this analysis, we improve the algorithm introduced by Huilin Gao, C. Birkett, and Lettenmaier (2012)—and modified by S. Zhang, Huilin Gao, and Naz (2014)—for processing cloudy images and tailor it to Landsat data. We then infer the time series of reservoir storage by combining information on water surface area and area–storage curve and validate the results using the altimetry water level data with the elevation–storage curve (Sect. 2.3). With the storage time series at hand, we unveil the filling strategies, infer the rule curves, and relate the downstream hydrological alterations to the reservoir management strategies

(Sect. 2.4). Building on this knowledge, we identify and discuss opportunities for improving the management of the Lower Mekong resources under present and future scenarios (Sects. 2.5 and 2.6).

2.2 Study site and data

2.2.1 Study site

The Mekong is a transboundary river flowing across Southwest China and Southeast Asia (Fig. 2.1a). The river originates from the Tibetan Plateau at an altitude of about 5200 m a.s.l. and flows in a northwest-southeast direction through six countries (China, Myanmar, Laos, Thailand, Cambodia, and Vietnam) before pouring into the East Vietnam Sea. The Mekong drains an area of 795 000 km^2 with an average annual discharge of approximately km^3. Its upper portion is 2140 km long and drains an area of 176 400 km^2. The high mountains and low valleys characterizing the Lancang River basin contribute to the spatial variability of precipitation, whose annual average varies from 750 to 1025 mm across the basin. Precipitation is also unevenly distributed across the year, with two distinct dry (December to May) and wet (June to November) seasons. The streamflow reflects a similar seasonal pattern (Yun et al., 2020). Although the drainage area of the Lancang River accounts for about 22 % of the total catchment area, the Lancang contributes only to 16 % of the average annual discharge of the whole Mekong River (MRC, 2009).

The advantageous topography and abundant water availability make the Lancang River basin an ideal spot for the hydropower industry (Dang, Chowdhury, and Galelli, 2020). The first dam on the mainstream of the Lancang (Manwan) began its operations in 1992, followed by Dachaoshan in 2003 and Jinghong in 2008. The two largest dams (Xiaowan and Nuozhadu) became operational in 2009 and 2013, respectively. And since 2016, at least one dam has joined the Lancang's reservoir system every year. Overall, this rapid transformation of the basin resulted in a system comprising 11 operational and 1 planned dam (Fig. 2.1b).

The design of the cascade reservoir system reflects the topographic characteristics of the basin. Specifically, the presence of narrow valleys with steep sides required the construction of high dams (see Fig. 2.2 and the list of design specifications in Appx. A Table A.1 In turn, this resulted in reservoirs with large storage capacity relative to inflow, steep banks, and long and horizontally narrow shapes. The total storage capacity is 42 170 Mm^3, about 55 % of the average annual discharge at Chiang Saen gauging station, the first downstream station with publicly available data (Fig. 2.1). These reservoirs form a long and complex cascade system, so it is only by studying it in its entirety that we can understand how storage operating patterns have evolved over the past decade.

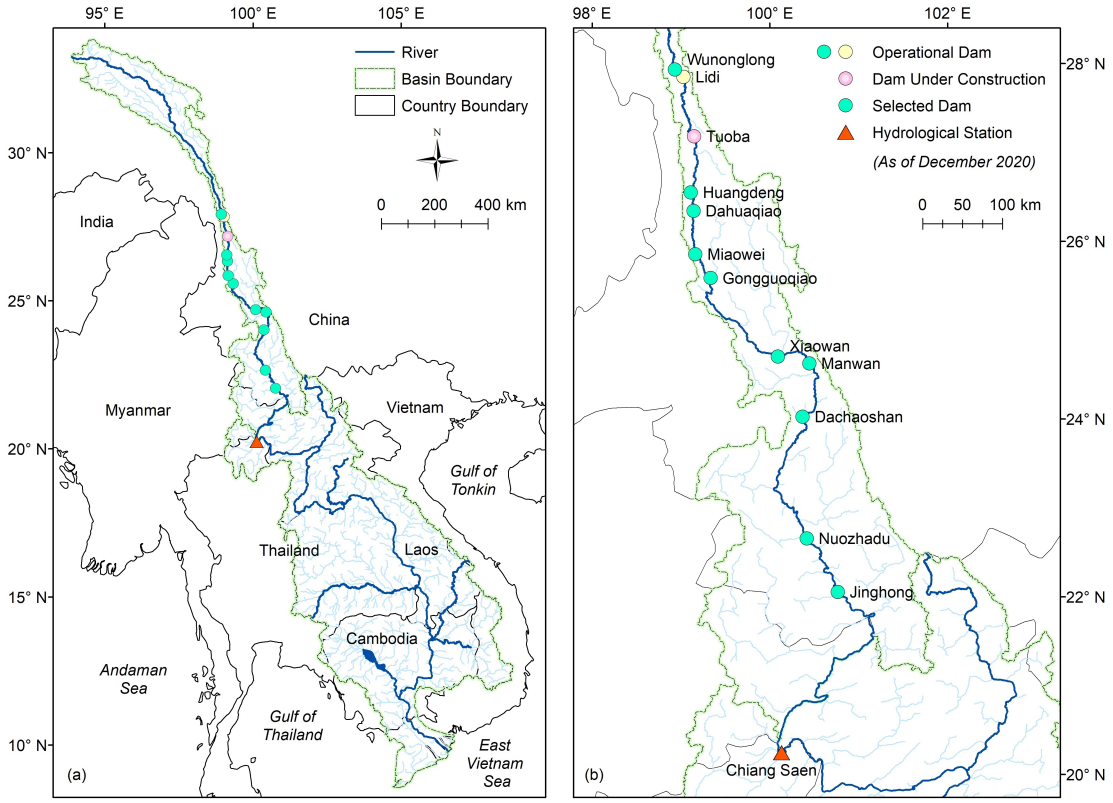

FIGURE 2.1: The Mekong and Lancang River Basins ((a) and (b), respectively). In both maps we report the location of the gauging station as well as the hydropower dams on the main stem of the Lancang. All dams were operational as of December 2020, with the exception of Tuoba, which is currently under construction. The dams analyzed in our study are denoted by a green circle.

2.2.2 Data

In this study, we focus on the 10 largest operational reservoirs (each with a volume larger than 100 Mm^3), all located on the main stem of the Lancang River. We select 2008–2020 as our study period because it includes the year of commission of most dams (8 out of 10), a choice that allows us to study their operations during the filling period as well as under regular operating conditions. Extending the temporal horizon to include the year of commission of the two remaining dams (Manwan and Dachaoshan, commissioned in 1992 and 2003) would complicate the analysis unnecessarily, since their aggregated storage capacity corresponds to only 2.14 % of the current total system capacity. For the aforementioned study period we gathered data on the digital elevation model (DEM), satellite imagery, and radar altimetry water level.

Digital elevation model

Digital elevation models contain the information on terrain elevation needed to represent reservoir bathymetry, so they are commonly used to establish the relationship

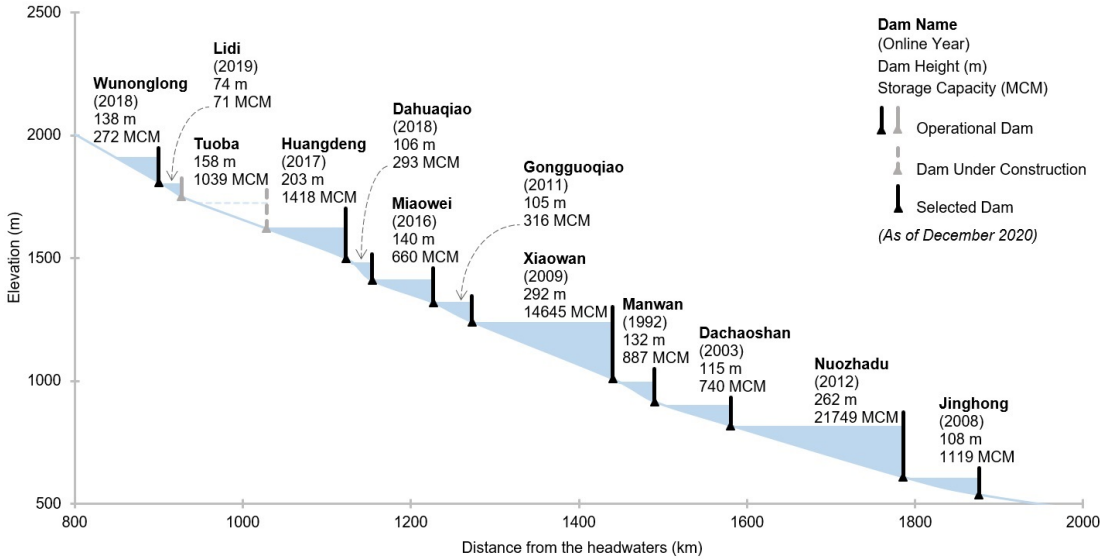

FIGURE 2.2: Cascade reservoir system on the Lancang River. Further details about the design specifications are provided in Table A.1

between water level and water surface area (Bonnema, Sikder, et al., 2016; S. Zhang and Huilin Gao, 2020). In this study, we use the global 30 m spatial resolution DEM obtained by the Shuttle Radar and Topography Mission (SRTM). The SRTM-DEM provides the terrain elevation above the water level at the observation time of the SRTM mission (February 2000) in signed integer raster format. The SRTM-DEM is the best choice for representing reservoir bathymetry on the Lancang River because of its high spatial resolution, acquisition time (9 out of 10 selected reservoirs were constructed after February 2000), and free accessibility. We note that the reservoir construction may have slightly changed the bathymetry, but these changes are negligible for our study site. That is for two reasons. First, Lancang's reservoirs have horizontally narrow and long shapes. Their length varies from about 25 km (Dahuaqiao) to about 198 km (see Fig. 2.2). Because of these characteristics, dam construction sites (typically carried out near the dam location) only affect a very small portion of the reservoir bathymetry. Second, Lancang's reservoirs have a large portion of dead storage, from about 32 % (Xiaowan) to 87 % (Wunonglong). Therefore, the reservoir bathymetry in the variation range of the reservoirs is barely affected by dam constructions.

Satellite imagery

We use images from Landsat 5, 7, and 8 to estimate the water surface area of the Lancang reservoirs. That is for four reasons. First, Landsat imagery has been collected for a long time, so it covers our study period. Second, Landsat images have a high spatial resolution (30 m), which is suitable to detect changes in the water surface area of reservoirs with long and horizontally narrow shapes, like the ones in our study site. For instance, the width (at full capacity) of Nuozhadu and Xiaowan reservoirs, the two largest reservoirs on the Lancang River, is only ∼1500 and ∼1000 m. Third, the frequency of Landsat imagery (16 d) is enough to assess the change of reservoir water

surface area with a monthly time step—a reasonable temporal resolution for reservoirs characterized by massive storage capacities (see Fig. A.1). Moreover, we can double the number of images for each month because the active period of Landsat 7 (1999–present) overlaps with the active period of Landsat 5 (1984–2013) and Landsat 8 (2013–present). Fourth, Landsat imagery has been successfully used in other studies to estimate reservoir water surface area (e.g., Duan and Bastiaanssen (2013), Avisse et al. (2017), Bonnema and F. Hossain (2017)). The images used in this study are archived from the Landsat Collection-1 Level-2 (Surface Reflectance) of the United States Geological Survey (USGS). It is also worth mentioning here that (publicly available) imagery provided by other missions, such as MODIS (Moderate Resolution Imaging Spectroradiometer) and Sentinel, may not be best suited for this study. MODIS imagery has a high frequency (twice a day) but a lower spatial resolution (250 m), which makes it unsuitable for estimating the water surface area of medium and small reservoirs or large, but horizontally narrow, reservoirs (the width of all reservoirs, except for the two largest ones, varies from 300 to 600 m). Meanwhile, Sentinel has been operational since 2015, so its temporal coverage is not sufficiently long for our analysis. Further details concerning a comparison between Landsat, MODIS, and Sentinel imagery are reported in Table 1.1.

Radar altimetry water level data

Satellite radar altimeters have been used for decades to monitor the ocean and large reservoirs and lakes (Schwatke et al., 2015)—see Table 1.1 for additional details on satellite altimeters. Because radar altimetry data from each satellite are not available for all reservoirs, we make use of all available sources of radar altimetry data previously processed into water level time series—following the methods developed by the NASA Ocean Altimeter Pathfinder Project—and published by the Global Reservoirs and Lakes Monitor (G-REALM) (C. M. Birkett et al., 2011). Specifically, we use Jason-2 (2008–2016) for Nuozhadu, Xiaowan, and Huangdeng, Jason-3 (2016–2020) for Xiaowan and Huangdeng, Sentinel-3A (2016–2018) for Nuozhadu, and Sentinel-3B (2019–2020) for Jinghong. As we shall see, the lack of radar altimetry water level data for the remaining reservoirs does not affect the conclusions of our study, since we use them only for the purpose of validating the results obtained through satellite imagery.

2.3 Methodology

Our methodology is chiefly aimed at estimating (and validating) the storage time series of each reservoir. According to this purpose, we follow three main steps, illustrated in Fig. 2.3. We begin by processing the information contained in the DEM to estimate the relationship between water level (WL) and water surface area (WSA) for each reservoir. With this relationship, also called the elevation–area (E–A) curve, we calculate the elevation–storage (E–S) curve (the relationship between WL and storage volume) and the area–storage (A–S) curve (the relationship between WSA and storage volume). Then, we estimate the WSA of each reservoir from all Landsat images available for our study period. To carry out this step, we rely on a novel variant of the WSA estimation algorithm developed by Huilin Gao, C. Birkett, and Lettenmaier (2012) and modified by S. Zhang, Huilin Gao, and Naz (2014). Finally, we use the A–S curves and WSA

time series to infer how the storage of each reservoir varied during the study period. We validate our methodology on two reservoirs located outside of the Lancang Basin: Bhumibol reservoir in Chao Phraya River basin and Ubol Ratana reservoir in Lower Mekong River basin, for which storage and water level data are publicly available (see Figs. A.2 and A.3). A detailed explanation of these steps is provided in Sect. 2.3.1 and 2.3.2. In Sect. 2.3.3 and 2.3.4, we describe the numerical approaches adopted to estimate the reservoir filling strategies and analyze the effect of reservoir operations on downstream discharge.

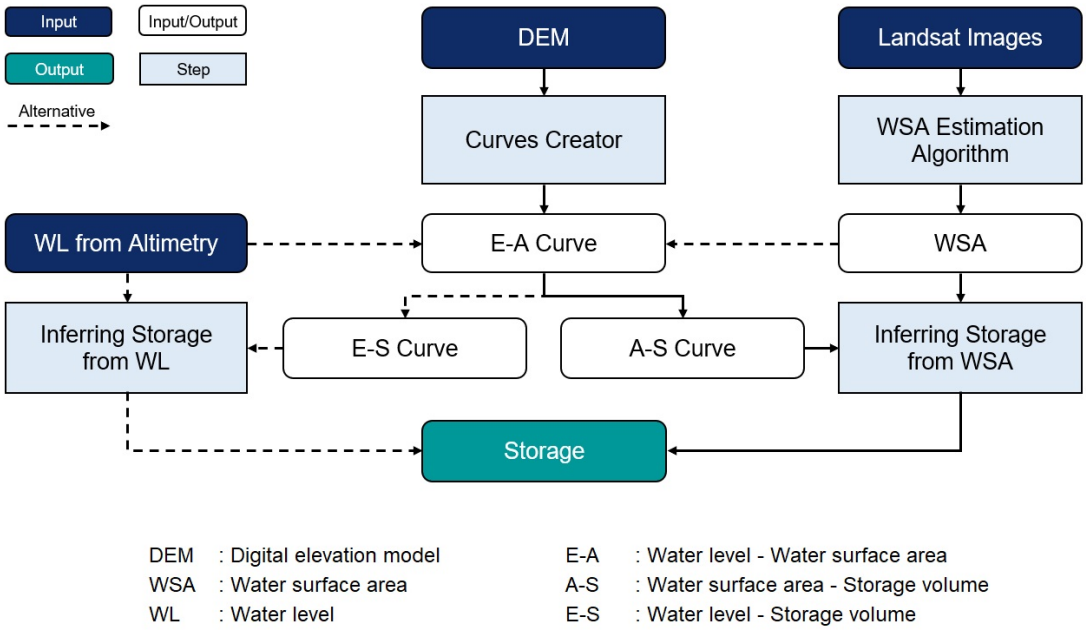

FIGURE 2.3: Flowchart representing our methodological approach. The two key steps are the calculation of the E–A, E–S, and A–S curves (from the DEM) and the estimation of the WSA (from Landsat imagery). With this information at hand, we estimate the storage time series of each reservoir. The altimetry water level data are coupled with the E–S curve to re-estimate the storage time series with independent data, thereby validating the estimation based on Landsat imagery.

2.3.1 Estimating the E-A, A-S, and E-S curves

Recall that for 9, out of 10, reservoirs, the SRTM-DEM can provide full information on bathymetry (Sect. 2.2.2). To estimate the E–A curve of these reservoirs, we first isolate the DEM data with the contour corresponding to maximum water level and dam crest line. The purpose of this step is to calculate the curve within the extent of the reservoir only and thus avoid errors due to the inclusion of surrounding areas. Then, we calculate the surface area corresponding to each 1 m elevation of the DEM. Specifically, with each elevation value (each meter) from the lowest elevation within the reservoir extent to the maximum water level, we count the number of pixels having a value equal to or

smaller than that elevation value. This is because, when water reaches that elevation, the area corresponding to those pixels is inundated. Then, we multiply the number of pixels by the pixel size (30 m × 30 m) to get the water surface area. We finally fit a fifth-degree polynomial (degree determined by trial and error) to the data points so obtained. For the remaining reservoir, Manwan, we apply the same procedure but only to the portion above the water level recorded by the SRTM. To approximate the E–A curve below that water level, we fit a fifth-degree polynomial to the part above the water surface and then extend it below the water surface, as in Bonnema, Sikder, et al. (2016) and Bonnema and F. Hossain (2017).

With the E–A curve at hand, we calculate the storage volume corresponding to each 1 m elevation of the DEM. This operation is carried out using the following trapezoidal approximation (Huilin Gao, C. Birkett, and Lettenmaier, 2012; Bonnema and F. Hossain, 2019; Li et al., 2019; Tortini et al., 2020):

$$V_i = \sum_{j=l+1}^{i} (A_j + A_{j-1})(E_j - E_{j-1})/2, \tag{2.1}$$

where V_i is the storage volume corresponding to the water level E_i and water surface area A_i, and l denotes the lowest elevation of the reservoir bathymetry (i.e., $A_l = 0$). The trapezoidal approximation is used here instead of a direct calculation from the DEM because the latter is not applicable to Manwan—while it is desirable to minimize the differences in data processing for all reservoirs. In addition, with the E–A curves validated by water level observations (from altimetry data) and water surface area (from Landsat images), we can confidently develop the E–S and A–S curves from the E–A curves using the trapezoidal approximation (recall we do not have observed storage data to validate the E–S and A–S curves estimated directly from the DEM). To strengthen the rationale for using the trapezoidal approximation, we compare the results obtained with the two methods. The differences in storage corresponding to each water level in the variation range are not more than 1 % (for Jinghong, Miaowei, Huangdeng, and Wunonglong) and 2 % (for Nuozhadu, Dachaoshan, Xiaowan, Gongguoqiao, and Dahuaqiao). The detailed comparisons for Nuozhadu and Xiaowan reservoirs can be found in Table A.2 and Fig. A.4. Finally, we use the data points on storage volume to fit the A–S and E–S curves. All aforementioned operations are carried out in Python 3.7 with the aid of the *OSGeo* library.

2.3.2 Inferring the water surface area

Water surface data can be inferred from Landsat images by classifying each pixel with either a single spectral band (e.g., near-infrared band) or a spectral index calculated from multiple bands (see Table A.3 for a list of the most common indices). In general, the use of a single spectral band reduces the computational requirements (Li et al., 2019), but spectral indices tend to provide more robust results (K.-T. Liu et al., 2016). Whatever the method used, one key challenge with Landsat images stands in the presence of clouds, cloud shadow, and no-data pixels (for Landsat 7), which may lead to a misclassification of water pixels and the consequent underestimation of the water surface area. To handle this problem, we use a novel variant of the WSA estimation

algorithm introduced by Huilin Gao, C. Birkett, and Lettenmaier (2012) and S. Zhang, Huilin Gao, and Naz (2014), originally conceived to extract water surface area from the normalized difference vegetation index (NDVI) layer—which is included in the 250 m resolution global Terra MODIS vegetation indices (MOD13Q1), a level-3 MODIS product provided by NASA.

Like the modified version by S. Zhang, Huilin Gao, and Naz (2014), our algorithm consists of two main phases: mask creation and water classification improvement, illustrated in Fig. 2.4 with light blue and light green boxes. In the first phase, the cloudless images are processed together to create two products: the expanded mask and zone mask. The two masks are then used in the second phase, where the Landsat images are individually processed to obtain the water surface area corresponding to the collection time of each image. The major modifications with respect to the version by S. Zhang, Huilin Gao, and Naz (2014) are the selection of cloudless images (Step 1.1) and identification of additional water zones (Step 2.5), two modifications needed to ensure that the algorithm performs well with Landsat images (instead of the NDVI layer of MOD13Q1). Further details for each phase and step are provided below.

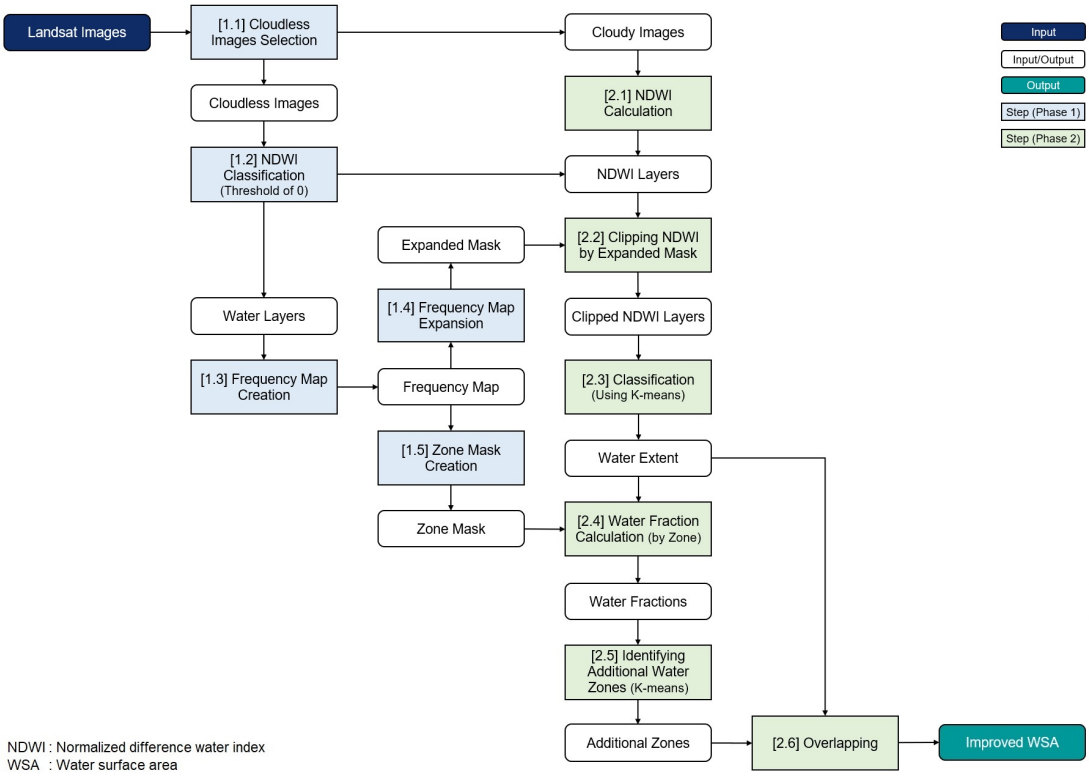

FIGURE 2.4: WSA estimation algorithm. The first phase is aimed at the creation of the expanded mask and zone mask, while the second phase focuses on the processing of each image to yield the water surface area.

(1.1) Selection of cloudless images. Cloudless images are the ones that do not contain clouds or contain very little clouds on the reservoir surface extent. For our application,

we define a cloudless image as an image with less than 20 % of cloud cover on the maximum reservoir surface extent. To identify these images, we use the BQA band (the band of quality assessment), which contains the information on cloud pixels. As we shall see, working on a subset of cloudless Landsat images is necessary to preserve the quality of the frequency map and masks produced in the next steps. Note that the version by S. Zhang, Huilin Gao, and Naz (2014) did not include this step because cloud effects are partially removed from the NDVI layer in MOD13Q1 (Didan and Munoz, 2019). This is the result of selecting the best available pixel value (the low clouds and the highest NDVI value) from all daily acquisitions within a 16 d period.

(1.2) NDWI-based classification. To classify the water and non-water pixels, we use the normalized difference water index (NDWI) with a threshold value equal to 0. The choice of index and corresponding threshold is based on a preliminary analysis, in which we compared the performance of NDWI, NDVI, and MNDWI (modified normalized difference water index) for all 10 reservoirs. The results of Xiaowan and Nuozhadu reservoirs, reported in Figs. A.5 and A.6 for 60 cloudless Landsat images for each reservoir, show that the NDWI-based classification matches the maximum water extent reported in the Maximum Water Extent dataset, developed by the European Commission's Joint Research Centre (Pekel et al., 2016). On the other hand, NDVI and MNDWI tend to provide less reliable results. As for the threshold value, 0.05 and 0.1 (for NDWI) tend to lead to an underestimation of the water pixels, since the total number of times a water pixel is correctly classified as water is less than 60. We also manually checked the obtained water layers with the true-color Landsat images for a number of images before making our decision of using NDWI. The NDWI layers calculated this way are subsequently used in Step 2.2.

(1.3) Frequency map creation. To create the frequency map, we first calculate the percentage of times in which a pixel is classified as water (based on its NDWI value) in all selected cloudless images. This operation is carried out for all pixels within the bounding box of the reservoir extent. Then, we create the frequency map by selecting the pixels with frequency larger than 0. This step is illustrated in Fig. 2.5a, b.

(1.4) Frequency map expansion. We expand the frequency map by buffering it with three additional pixels; in other words, we add three pixels around the peripheral water pixels (see Fig. 2.5a, b). The expansion is aimed to ensure that no possible water pixels are missed out. This 90 m buffer around the nominal shoreline is deemed sufficient for our case study, since reservoirs in the Lancang are located in steep terrains, where the storage is controlled by elevation more than area. The expanded frequency map is used in Step 2.2 to clip the NDWI layer; hereafter, we refer to it as the expanded mask.

(1.5) Zone mask creation. In the last step of Phase 1, we convert the frequency map into a 50-zone mask. As illustrated in Fig. 2.5c, the i-th zone contains the pixels classified as water with a frequency greater than $2 \cdot (i-1)$ % and less than or equal to $2 \cdot i$ % (with $i = 1, \ldots 50$). For example, Zone 1 contains the pixels classified as water from 0 % to 2 % of the time, while Zone 2 contains those classified as water from 2 % to 4 % of the time. At the end of this phase, we obtain the two inputs for the next phase, that is, the

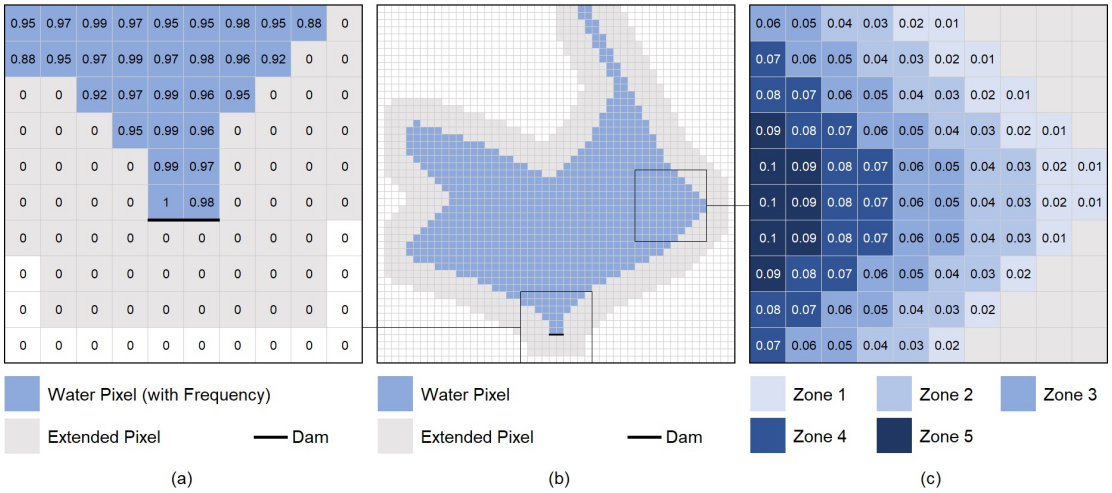

FIGURE 2.5: Examples of a frequency map (a, b), expanded mask (a, b), and zone mask (c).

expanded mask and zone mask.

(2.1) NDWI calculation. Here, we calculate the NDWI index for the remaining Landsat images—with clouds, cloud shadow, and no-data pixels—and pass them to the next step in the form of a raster layer for each image. Note that the goal of this second phase is to improve the water surface classification of the images, so as to maximize the number of data points available for our study period, especially for the monsoon season when Landsat observations are heavily affected by clouds. Failing to improve the cloudy images can make the water surface area estimates inaccurate.

(2.2) Clipping the NDWI layer by the expanded mask. The NDWI raster layer obtained in Steps 1.2 and 2.1 is clipped by the expanded mask created in Step 1.4.

(2.3) k-means-based classification of the water pixels. Because of the presence of clouds, and other disturbances, the of use of the same NDWI threshold (equal to 0) in all Landsat images may lead to overestimation or underestimation errors of the water surface area. To find NDWI thresholds for each Landsat image, we resort to k-means clustering. Specifically, we set k equal to 3 (a value found by trial-and-error) and apply k-means clustering to all pixels in the NDWI layer (Fig. 2.6a). Water pixels tend to fall into the cluster with the highest NDWI value because the NDWI of water pixels has a higher value than the one of non-water pixels. Results are verified by manually checking the classified water layer with true-color Landsat images.

(2.4) Water fraction calculation (by zone). The zone mask created in Step 1.5 is used here to divide the water extent layer (obtained in the previous step) into 50 zones. For the i-th zone, we define the water fraction p_i as follows:

$$p_i = n_i/N_i, \ i = 1, 2, ..., 50, \tag{2.2}$$

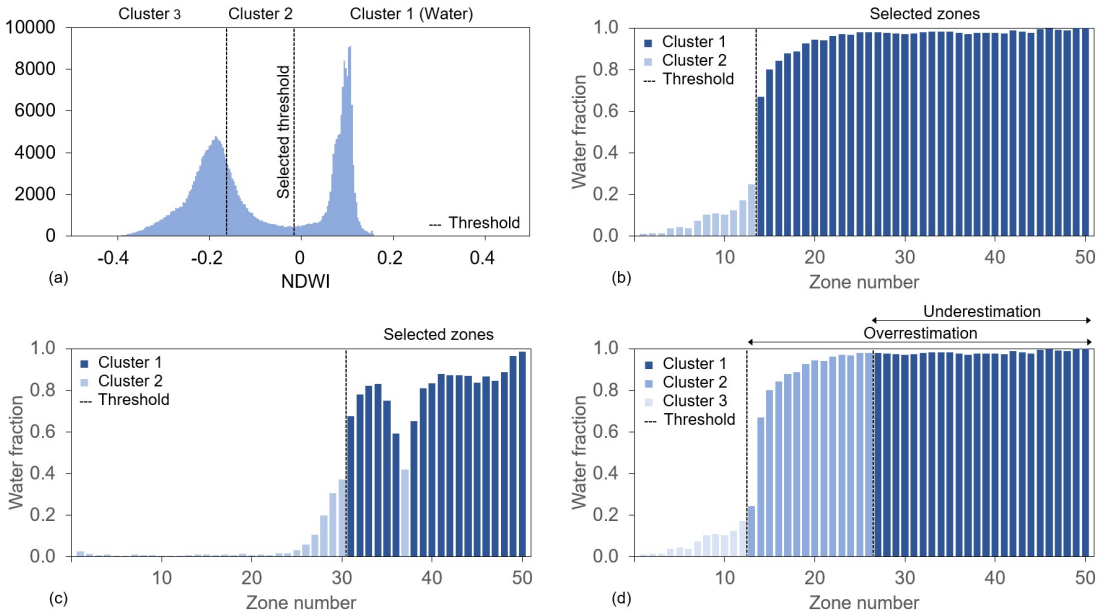

FIGURE 2.6: Illustration of the k-means classifications used in Steps 2.3 and 2.5. Panel (a) shows the water pixels classification based on NDWI values (Step 2.3), while panels (b,c) show the identification of additional water zones based on two clusters (Step 2.5). Panel (d) illustrates the issues that raise when using three clusters in Step 2.5.

where p_i represents the ratio between the number n_i of pixels classified as water in zone i (with the NDWI-based k-means clustering) and the total number N_i of pixels in zone i (retrieved from the zone mask). The information provided by the water fraction of each zone is used in the next step to improve the water pixel classification.

(2.5) Identification of additional water zones. We improve the classification of water pixels by identifying the additional water zones based on their water fraction. To do so, we resort again to the k-means clustering algorithm. Moreover, because of the continuity of water extent (water expands from higher frequency to lower frequency zones), we also take into account the zone number (or frequency value). Then, we formulate a clustering problem in a two-dimensional space constituted by water fraction and zone number. We solve the clustering problem with a value of k equal to two, found by trial and error. Fig. 2.6b and c shows two examples with k=2, while Fig. 2.6d reports an example for an unsuitable value of k. The lowest zone in the higher cluster (zone 14 in Fig. 2.6b and zone 31 in Fig. 2.6c) is the threshold above which zones are converted to water pixels. The reason for converting all pixels from the threshold zone onwards to water pixels is that the pixels in the same zone have the same (or very similar) inundation probability, and, at each observation time, they fall into one of two scenarios: (1) they are both non-water pixels, or (2) they are both water pixels (even when the water fraction of that zone is less than 100 %, due to cloud cover). Naturally, there can be a small error from the threshold zone. For example, Zone 14 in Fig. 2.6b contains pixels with 26 %-28 % inundation probability, but sometimes, the threshold of inundation probability is not exactly 26 % (e.g., 26.5 %, 27 %, ...). Note that we could increase

the performance by dividing the frequency map into a larger number of zones, but this would require a larger number of cloudless images. This step represents the second modification of the original WSA estimation algorithm, which uses a quality parameter not suitable for Landsat images – since the cloud effects are not mitigated, unlike the NDVI layer in MOD13Q1.

(2.6) Overlapping. Finally, the layer of additional water pixels is overlapped on the layer of water extent obtained in Step 2.3. The final output is the improved water classification for each image characterized by cloud cover or other disturbances. All the aforementioned operations are carried out in Python 3.7 with the aid of the *OSGeo* and *SKLearn* libraries.

2.3.3 Inferring the reservoirs' filling strategies

Determining the filling strategy of a reservoir means deciding the rate with which the reservoir is filled and, therefore, the fraction of inflow that is retained on a periodic basis—monthly, in our case. The problem is formalized by the following mass balance equation:

$$S_t = S_{t-1} + \theta \cdot Q_t - E_t, \tag{2.3}$$

where S_t is the reservoir storage at time t, Q_t is the inflow volume in the interval $(t-1, t]$, E_t is the evaporation loss in the interval $(t-1, t]$, and θ is a parameter varying between 0 and 1 and expressing the fraction of inflow volume retained by the reservoir. In our case, the goal is to determine the value of θ (in each month) for Nuozhadu and Xiaowan during the periods 2012-2013 and 2009-2010, respectively.

Observed inflow data are not available, so we resort to modeled ones. Specifically, we use daily inflow data simulated by VIC-Res (Dang, Chowdhury, and Galelli, 2020; Dang, Vu, et al., 2020), a variant of the variable infiltration capacity (VIC) model—a large-scale, semi-distributed hydrological model first developed by Liang et al. (2014). Similarly to VIC, VIC-Res contains a rainfall–runoff module and a routing module. In the first module, the study region is organized as computational cells with a customizable cell size (0.0625° in our case), in which key hydrological processes (evapotranspiration, infiltration, baseflow, and runoff) are calculated as a function of hydrometeorological forcings (precipitation, temperature, wind speed, etc.) and soil parameters. Then, the routing module routes the simulated runoff and baseflow throughout the river network using the linearized Saint-Venant equation (Lohmann, Nolte-Holube, and Raschke, 1996; Lohmann, Raschke, et al., 1998). In VIC-Res, the routing process includes a detailed representation of water reservoir operations: for each reservoir in a given study site, the model calculates the mass balance and release, with the latter determined by operating rules or predefined release time series. VIC-Res has been tested on several sites, including the Lancang River basin (over the period 1996–2005). In particular, Dang, Chowdhury, and Galelli (2020) reported the results of model calibration with observed discharge at Chiang Saen station and model validation with observed discharge at Jiuzhou station, located right upstream of Xiaowan reservoir.

Here, we use the same VIC-Res model, which we force with rainfall and temperature (maximum and minimum) data retrieved from CHIRPS-2.0 and ERA5 dataset. Land use and cover data were obtained from the Global Land Cover Characterization dataset, while the soil data were extracted from the Harmonized World Soil Database. The monthly leaf area index and albedo were derived from the Terra MODIS satellite images, which provide changes in canopy and snow coverage over time. The flow direction map used by VIC-Res is based on the SRTM-DEM. Since Dang, Chowdhury, and Galelli (2020) considered the dams built before 2005 and used the rule curves proposed by Piman et al. (2013), we slightly adapt the model to handle two challenges for our current study: (1) consider more reservoirs (all dams on the mainstream built until 2013) and (2) leverage the actual storage data retrieved from satellite data. To set up VIC-Res in our study, we therefore proceeded as follows. For each reservoir, we take data on inflow (simulated), storage (estimated from the satellite data), and evaporation (simulated using the estimated water surface area and evaporation rates calculated with the Penman equation). We then invert the mass balance equation to calculate the release, which is used as input to VIC-Res to simulate the storage dynamics of each reservoir. The process is repeated sequentially—starting with the most upstream dam—so as to ensure that the cascading impacts of dams are captured correctly. To ensure the reliability of this analysis, we extend the model validation at Chiang Saen for the filling period of Nuozhadu and Xiaowan (2009–2013); see Fig. A.7. The comparison between modeled and simulated storage is reported in Fig. A.8.

2.3.4 Indicators of hydrological alteration

The availability of storage data also allows us to decipher the impact of dam operations on downstream (measured) discharge. To do that, we calculate two time-varying indicators of hydrological alteration (I_1 and I_2). I_1 represents the fraction of the natural flow retained in the reservoir system for each month in which the system is storing water (i.e., when $\Delta S_t = S_t - S_{t-1} > 0$). I_2 represents the fraction of the actual flow released from the reservoir system for each month in which the system is releasing water (i.e., $\Delta S_t < 0$). I_1 and I_2 are calculated as follows:

$$I_{1,t} = \frac{\Delta S_t}{\Delta S_t + Q_t}, \tag{2.4}$$

$$I_{2,t} = \frac{\Delta S_t}{Q_t}, \tag{2.5}$$

where Q_t is the observed discharge volume downstream of the reservoir system (at Chiang Saen) in month t. Note that the denominator in Eq. (2.4) approximates the natural flow in month t (it is the sum of actual discharge and volume of water retained upstream in a given time interval).

2.4 Results

We begin this section by reporting the results of the analysis of DEM and satellite imagery, that is, the E–A, A–S, and E–S curves (Sect. 2.4.1) and water surface area (Sect. 2.4.2). We then present the storage time series of each reservoir, the information we use

to retrieve the dam operating policies under filling and steady-state conditions (Sect. 2.4.3). Finally, we leverage these results to analyze the effect of reservoir operations on downstream discharge (Sect. 2.4.4).

2.4.1 E-A, A-S, and E-S curves

The E–A curves of Nuozhadu and Xiaowan reservoirs are illustrated in Fig. 2.7 (panels a and d), where the blue circles represent the data points derived from the DEM, and the light blue lines are the fifth-degree polynomials fitted to them. Note that both curves correctly intersect the point identified by maximum water level and maximum water surface area, retrieved from Do et al. (2020). A similar evaluation is carried out for the A–S and E–S curves (Fig. 2.7, panels b, c, e, f), but this time using design specifications on full storage (A–S and E–S curves) and dead storage (E–S curves).

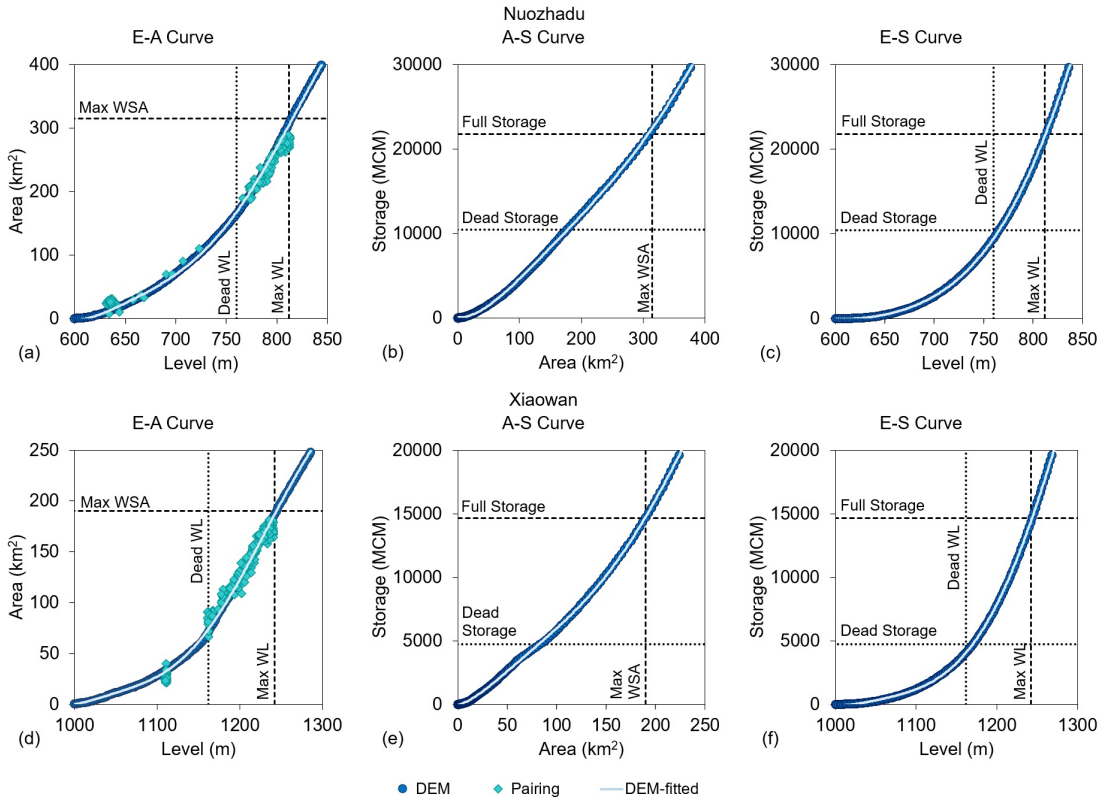

FIGURE 2.7: E–A, A–S, and E–S curves of Nuozhadu (a–c) and Xiaowan (d–f) reservoirs. The curves are represented by light blue lines, which are fitted to the data points (blue circles) derived from the DEM data. Note that the curves intersect the points identified by maximum water level, maximum water surface area, and full-storage volume (dashed lines) as well as those identified by dead water level and dead-storage volume (dotted lines). The cyan diamonds reported in panels (a) and (d) correspond to observations of water level and surface area obtained from altimetry data and Landsat imagery.

We carry out an additional validation of the E–A curves by comparing them against observations of water level and surface area obtained from radar altimetry data and Landsat imagery. These observations, illustrated in Fig. 2.7a and d by cyan diamonds, follow the curves identified through the DEM closely. Naturally, the cyan points are primarily concentrated between the dead and maximum water levels, which denote the normal range of operating conditions. As we shall see later, points below the dead water level correspond to the dam filling period.

The E–A, A–S, and E–S curves of the remaining eight reservoirs are reported in Figs. A.9 and A.10. Apart from the curves of Jinghong and Huangdeng, which are evaluated using the radar altimetry water level, the curves of the other reservoirs can only be evaluated by comparing them against the design specifications reported by Do et al. (2020). Such an evaluation is only partially successful, since we did not find a perfect match between curves and design specifications for Jinghong, Gongguoqiao, Miaowei, Dahuaqiao, and Wunonglong reservoirs. Considering that the procedure used to estimate the curves has been successfully employed in several studies (Bonnema, Sikder, et al., 2016; Bonnema and F. Hossain, 2017; S. Zhang and Huilin Gao, 2020), we suspect that the reason behind the mismatch may lie with the information on dam design specifications available to the public. In turn, this reinforces the need for research aimed to retrieve data on large-scale infrastructure in transboundary river basins. We also note that this source of uncertainty does not severely affect our study, since those five reservoirs account for a small fraction of the total system's storage (2.36 %, 0.74 %, 1.55 %, 0.69 %, and 0.64 %, respectively).

2.4.2 Water surface area

Recall that the WSA estimation algorithm builds on the idea of using cloudless images to create the expanded mask and zone mask, which are then employed to correct the classification of water pixels in images affected by clouds and other disturbances. In our case, such improvement is needed for 56 % of the 3004 Landsat images available for our study period (the number of usable images increases from 26 % to 82 %). As one might imagine, the classification correction is particularly important during the wet season, when cloud cover is more frequent—the number of usable images increases by 54 % of 1770 images (from 30 % to 84 %) in the dry season and 58 % of 1234 images (from 21 % to 79 %) in the wet season. The performance of the algorithm for each reservoir is summarized in Table A.4.

The WSA time series of Nuozhadu and Xiaowan reservoirs are reported in Fig. 2.8. The first result to note is the stark change in the WSA values before (light blue points) and after (cyan points) the classification improvement. The time series of corrected WSA values also starts to reveal the reservoirs' operating patterns: the sharp increase beginning in 2012 (Nuozhadu) and 2009 (Xiaowan) denotes the starting point of the reservoir filling period, while the large, annual, fluctuations suggest the presence of a broad range of operating conditions – the maximum surface area is reached only at the end of the wet season, while the rest of the year seems to be used to fill in and empty the reservoirs. In Sect. 2.4.3, wwill see how such variability translates into storage patterns.

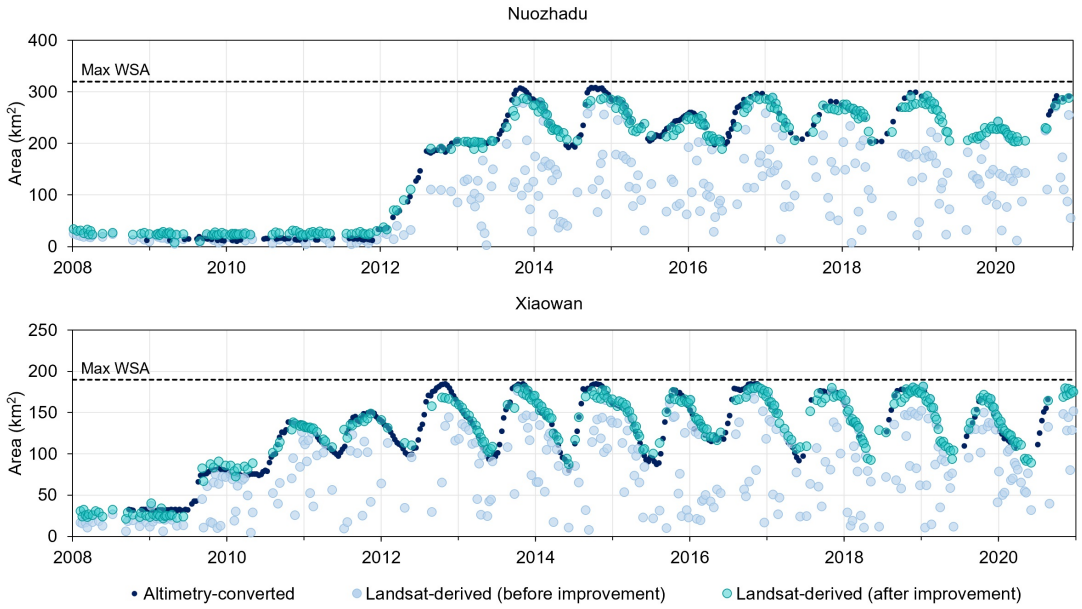

FIGURE 2.8: Water surface area of Nuozhadu (a) and Xiaowan (b) reservoirs. Note the drastic difference in WSA values before (light blue points) and after (cyan points) the classification improvement. The corrected values of WSA are well in agreement with those obtained through altimetry water level data and E–A curves (dark blue points).

To evaluate the results obtained with Landsat imagery, we leverage the radar altimetry water level data and E–A curves to obtain two independent WSA time series. As shown in Fig. 2.8, both modeling approaches provide very similar results. The same outcome can be seen in the WSA time series of Huangdeng and Jinghong reservoirs (see Fig. A.11). We also provide a quantitative comparison of Landsat-derived and altimetry-converted WSA for all four reservoirs mentioned above (see Table A.5). With this additional analysis we therefore serve two purposes: scrutinize the WSA values for the main reservoirs and empirically validate the approach based on Landsat imagery, the only one available for the remaining reservoirs.

2.4.3 Reservoir storage

A history of reservoir storage variations

Using the information on reservoir curves and water surface area described above, we estimate the storage time series of each reservoir as well as their aggregated value (Fig. 2.9). Note that the number of usable images per month is not the same. To have an evenly spaced time series of storage, we choose one WSA value (maximum value) for each month to infer the reservoir storage. The latter (dark blue line) portrays a history of rapid transitions, characterized by two major tipping points: the commission of Xiaowan and Nuozhadu reservoirs. After the commission of Xiaowan, we note a steady increase in the total storage (see the period between mid-2009 and 2012), an increase that becomes even more pronounced after the commission of Nuozhadu, in 2012. It is

indeed only after the filling of both reservoirs is completed, in 2014, that the total storage time series begins to exhibit a more cyclostationary behavior—the reservoir system is filled during the monsoon season and emptied thereafter. The construction of a few additional dams during the period 2016–2018 does not seem to dramatically affect this pattern. In fact, the remaining eight reservoirs appear to maintain a more constant storage (Fig. A.12).

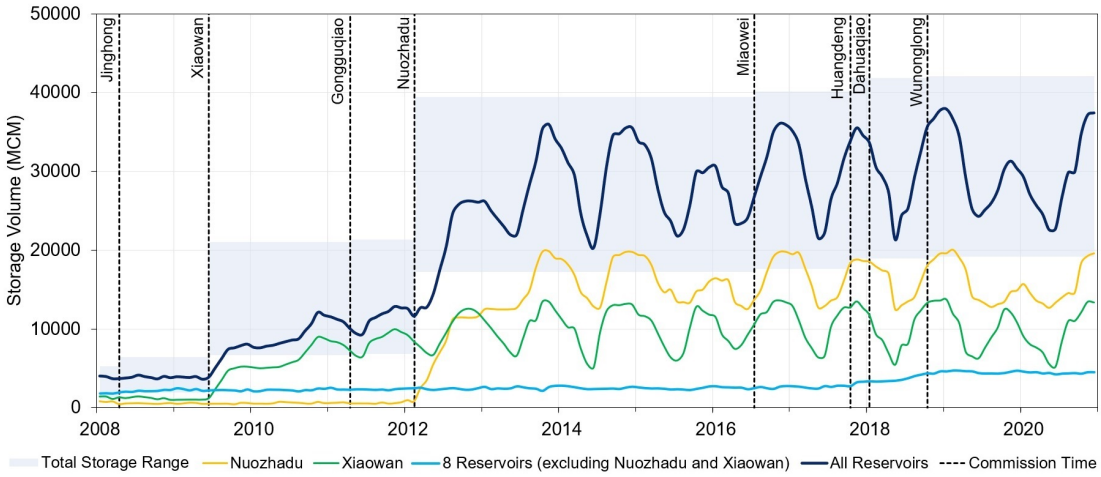

FIGURE 2.9: Storage variations of the Lancang reservoir system. The blue shaded area represents the range of variability of the total system's storage (between dead- and full-storage volume), while the actual storage dynamics are represented by the dark blue line. The storage dynamics of Nuozhadu, Xiaowan, and the remaining eight reservoirs are illustrated by the yellow, green, and blue lines. The vertical dashed lines denote the year of commission of each reservoir. Note that Manwan and Dachaoshan began operations in 1992 and 2003, respectively. We provide the storage time series of each individual reservoir in Fig. A.12.

Two key additional elements are revealed when comparing the total storage dynamics against its potential range of variability, that is, the space between the aggregated dead and full storage (blue shaded area). First, the operators do not seem to use the entire storage at their disposal—dead- and full-storage levels were never reached throughout the study period. A plausible explanation for this management strategy may be sought in the need of avoiding further disputes with downstream countries (Eyler and Weatherby, 2020) or alleviating hydropower curtailment (B. Liu et al., 2018). Second, the reservoir system was used at only half of its capacity in 2015–2016 and 2019–2020, with Nuozhadu reservoir playing a key role (yellow line). As we shall see in Sect. 2.4.4, this may be the result of persistent dry conditions (Yuanhe Yu et al., 2020; Ding and Hui Gao, 2020), rather than a response to the aforementioned socio-technical drivers.

Filling strategies and operating rules

In Fig. 2.10, we focus on the filling strategies and operating rules of Nuozhadu and Xiaowan: panels (a) and (b) show the values of θ (the parameter expressing the fraction of inflow volume retained by the reservoir), while panels (c) and (d) illustrate storage

volume (dark blue line), simulated inflow (green line), and storage change (light blue line)—that is, $S_t - S_{t-1}$, expressing the rate with which the reservoir is filled. The figure suggests that the operators adopted similar filling strategies: both reservoirs were filled in about 2 years (regardless of the different capacities), with the first wet season used to meet the dead storage and the second wet season used to double the storage volume. Interestingly, results indicate that the annual value of θ was kept constant during the filling period. For Nuozhadu, the operators retained 23 % of the annual inflow volume (for both years); for Xiaowan, that value was kept to 17 % and 15 %. Note that these are extremely large values: retaining 23 % of the annual inflow volume to Nuozhadu means storing roughly 9880 Mm^3, ∼12 % of the average annual discharge at Chiang Saen. The filling strategy of the remaining reservoirs is different: because they have smaller storage capacity—relative to inflow—they are filled in a few months (Fig. A.12).

By looking at the storage data of Nuozhadu and Xiaowan during normal operating conditions (i.e., once the filling is completed), we can get a few additional insights about the current management strategies (Fig. 2.10e, f). The first thing to note is the emergence of the seasonal patterns mentioned in the previous section; reservoirs are emptied during the pre-monsoon season and filled in thereafter. Second, the envelope of variability is rather broad, meaning that operators can deviate from the long-term pattern represented by the bolded red line. Such deviations are common throughout the entire Mekong Basin (see Bonnema and F. Hossain (2017) and Bonnema and F. Hossain (2019)) and are caused by inter-annual variability in discharge triggered by oceanic drivers (Hung T T Nguyen et al., 2020). Finally, the analysis confirms that Nuozhadu and Xiaowan have not yet been used at their full capacity. However, this is enough to keep the storage of the other reservoirs within a narrower range (Fig. A.13).

2.4.4 Impacts of reservoir operations on downstream discharge

Having established how the reservoirs in the Lancang River basin have been filled in and operated, we can finally explain their time-varying influence on the discharge measured at Chiang Saen (Sect. 2.2.1). The graphical analysis of total storage and discharge (Fig. 2.11c) highlights the stark changes in the flow regime in response to the increase in upstream storage. The flow regime changed drastically in late 2013, when the filling of Xiaowan and Nuozhadu was completed. By discharging water during the dry season and retaining it in the wet season, the hydropower dams largely increase low flows and decrease high flows (Table A.6). For example, the mean of the annual peak discharge decreased from 11 157 (1990–2008) to 6186 $m^3\ s^{-1}$ (2013-2020) (-45 %) while the mean of the annual lowest discharge grew from 638 to 1003 $m^3\ s^{-1}$ (+57 %). Similar figures are found for other statistics (Table A.6). We can also note a macroscopic change in the seasonal discharge pattern, from ample annual fluctuations to more rapid flow changes. All these observations are confirmed by the wavelet analysis reported in Fig. A.14.

As shown in Fig. 2.11b, the degree of flow alteration at Chiang Saen caused by the Lancang's dams increased significantly over time with three distinct stages: the first stage (before Xiaowan reservoir began operating), the middle stage, and the last stage (after Nuozhadu reservoir began operating). That means the range of variability of I_1

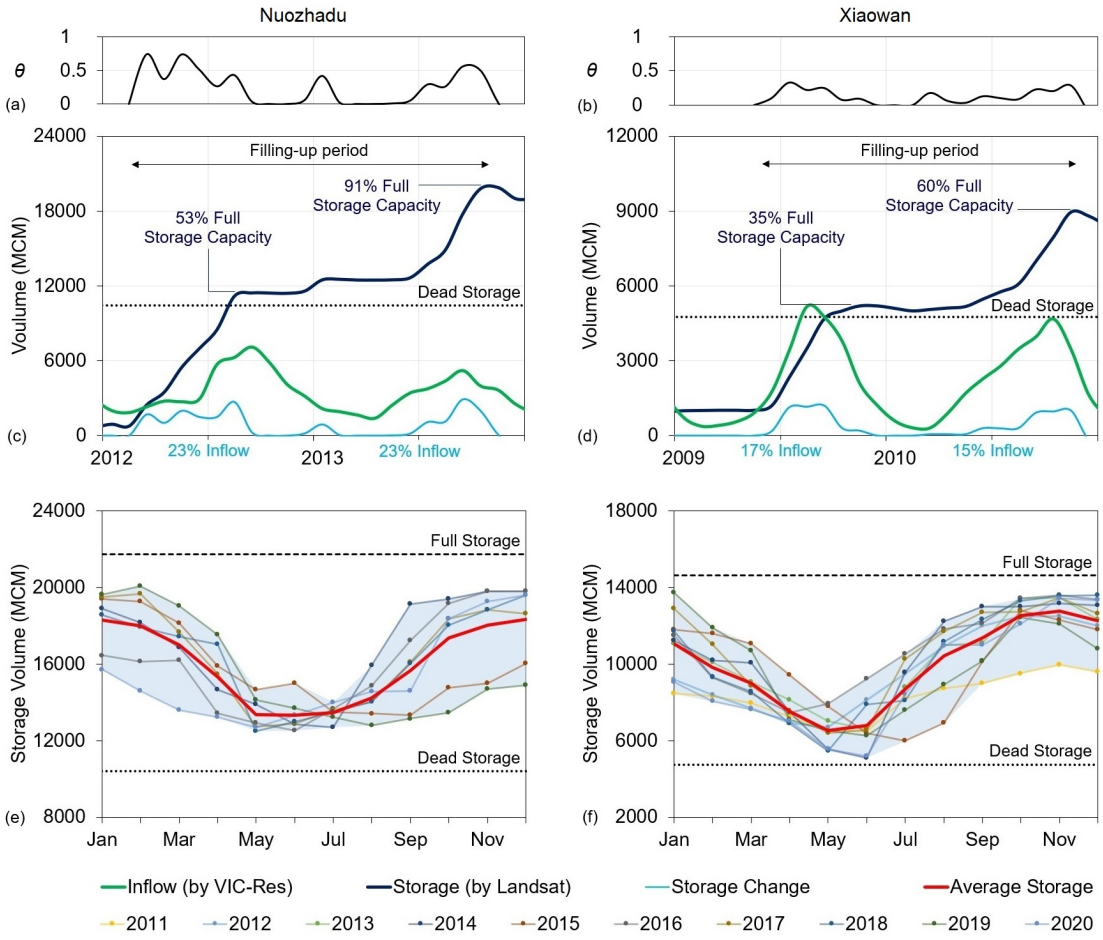

FIGURE 2.10: Filling strategies (a, b, c, d) and rule curves (e, f) of Nuozhadu (a, c, e) and Xiaowan (b, d, f) reservoirs. Panels (a) and (b) show the values of θ. In panels (c) and (d), the storage volume (dark blue line) is derived from DEM and Landsat data, while the inflow to the reservoir (green line) is calculated with the VIC-Res hydrological model. The storage change (light blue line) is defined as the difference in storage volume between two consecutive months. In panels (e) and (f), each line with circle makers illustrates the storage volume of a given year. The bolded red lines represent the average monthly storage volume, considered representative of the rule curves. All data visualized here have a monthly resolution.

(in black color) and I_2 (in red color) increased over time: [0, 0.04] and [-0.10, 0] in the first stage, [0, 0.20] and [-0.44, 0] in the second stage, and finally, [0, 0.50] and [-0.91, 0] in the last stage. With the number of reservoirs increasing rapidly in the last decade, the downstream discharge became increasingly controlled by dam operations.

By bringing the monthly precipitation anomalies (for the Lancang River basin) into the overall picture (Fig. 2.11a), we can better understand how dam operations partially contributed to downstream droughts and pluvials. A case in point is the drought in

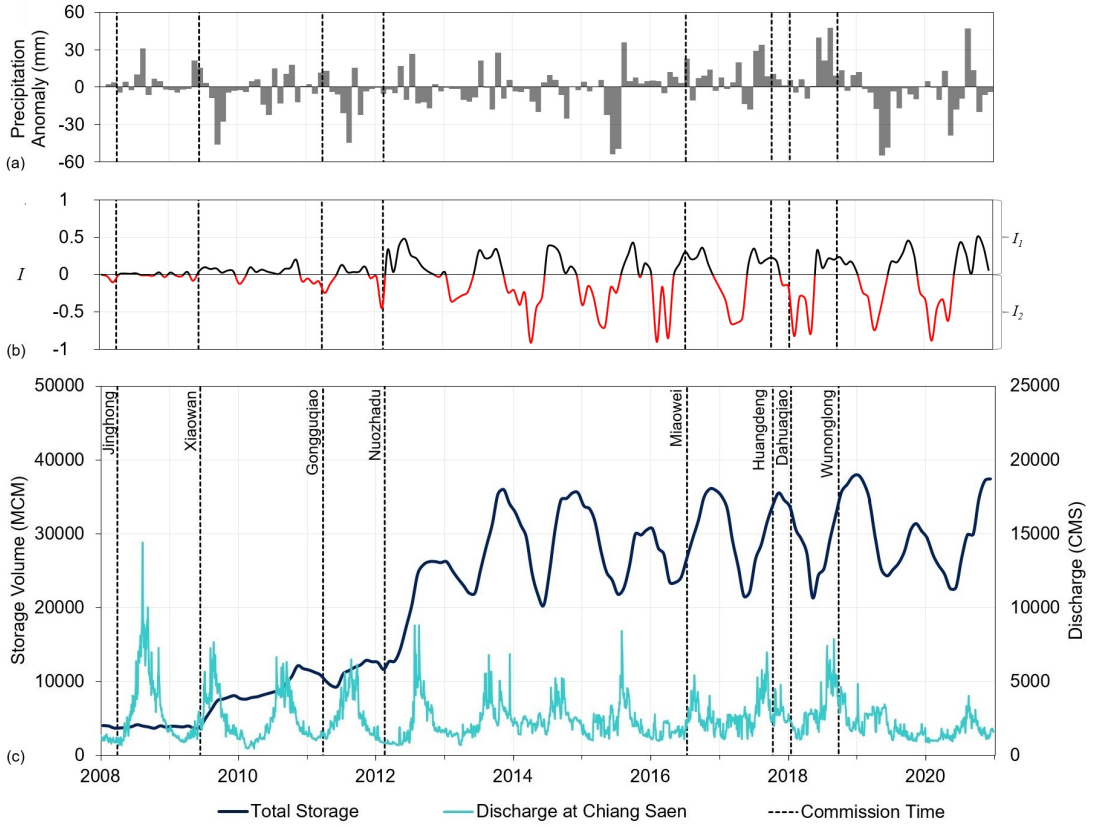

FIGURE 2.11: Impacts of reservoir operations on downstream discharge. Panel (a) shows the monthly precipitation anomaly in the Lancang River basin, calculated from the CHIRPS-2.0 dataset. Panel (b) represents the two indicators of hydrological alteration on discharge at Chiang Saen: I_1—the fraction of the natural flow retained in the reservoir system for each month in which the system is storing water—in black color, and I_2—the fraction of the actual flow released from the reservoir system for each month in which the system is releasing water—in red color. In panel (c), the bolded dark blue line represents the total storage of the reservoir system, while the cyan line represents the observed discharge at Chiang Saen.

the period 2019–2020. The monthly precipitation anomalies show that, in the wet season of 2019, the Lancang River basin received less precipitation, especially in May and June (around 50 mm less than the average for those months). However, the values of I1 indicate that the reservoir system kept retaining part of the inflow during the central months of the year (up to about 46 % in October). Because of such a combination of meteorological drought and dam operating strategies, the downstream area underwent a critical dry period, with Chiang Saen gauging station recording extremely low flows during the summer months (MRC, 2020b). The release of water during the subsequent dry season only partially alleviated the effect of the ongoing drought, since the negative precipitation anomaly persisted until mid-2020. Importantly, the 2019–2020 data suggest that the dam operating strategy was not largely affected by the meteorological conditions: the Lancang dams currently store about 46 % of the estimated natural

flow during the wet season (regardless of the monsoon's intensity) and then discharge it during the dry one, controlling up to 89 % of the dry-season flow—a pattern that has emerged since Xiaowan and Nuozhadu became fully operational. These results also highlight the importance of emergency releases from the upstream reservoirs, such as those that were implemented in 2016 (Tiezzi, 2016; Hecht et al., 2019). In regard to those emergency releases, it should be noted that the 2016 drought had much smaller magnitude than the 2019–2020 one and that the drought occurred during the first half of the year, when the reservoir system was releasing water following its normal operations. In sum, the availability of (inferred) storage data can help us put droughts, emergency releases, and pluvials into a broader perspective. Yet, such analyses should ideally be complemented by more significant data-sharing efforts among all riparian countries, a point that was recently reinforced by Keovilignavong, T. H. Nguyen, and Hirsch, 2021.

2.5 Discussion

Our study produced a monthly storage time series for each of the 10 large reservoirs built in the Lancang River basin during the past decades. These time series describe the evolution of a massive dam cascade system and highlight the pivotal role played by Xiaowan and Nuozhadu reservoirs. Taken together, the two reservoirs can make up to $\sim$ 85 % of the total system's storage in the Lancang, therefore largely controlling water availability in Northern Thailand and Laos. Bespoke information on their operating rules—ideally combined with real-time storage monitoring—is of paramount importance for many downstream socio-economic sectors. Consider, for instance, the Laotian hydropower industry, the largest regional exporter of electricity: since the construction of Xayaburi dam (1285 MW) on the main stem of the Mekong, part of the national hydropower production has depended on the state of the Lancang's reservoirs. Detailed information on their storage and operating rules could therefore be incorporated into Laos' energy system models (Chowdhury, Dang, Bagchi, et al., 2020), so as to address the asymmetric relation between China and Laos. Moving downstream, another sector that could benefit from our study is the Mekong's wetlands, a major biodiversity hotspot that is home to a multi-billion-dollar fishing industry (Arias et al., 2014; Dang, Cochrane, et al., 2016). Again, information on the state of the Lancang's reservoirs could help inform the operations of the many downstream dams, thereby helping implement release strategies that are less harmful for the environment(Sabo et al., 2017). In sum, the inferred rule curves could be used to predict outflow from the Lancang's reservoir system and adapt the operations of downstream dams.

Our analysis also provides a detailed description of the filling strategy of Nuozhadu and Xiaowan. We now know that both reservoirs reached steady-state operations in about 2 years by retaining from 15 % to 23 % of the annual inflow volume. This information is necessary to explain past anomalies in downstream water discharge and, most important, to prepare for future infrastructural changes in the Lancang's dam cascade system. China is already building a new dam (Tuoba: 1039 Mm^3) and planning the construction of 10 additional ones (MRC, 2020a). All these dams are rather large (e.g., Ru Mei: 13 385 Mm^3, Ban Da: 12 902 Mm^3, Gu Xue: 10 127 Mm^3), and taken together, they have a total storage capacity of about 64 950 Mm^3 (Schmitt et al., 2019). If the same filling strategies were to be implemented again, downstream countries should

expect a temporary, yet substantial, decrease of water availability but could also design adaptation and emergency plans. For example, Laos or Cambodia could decide to temporarily change their water management strategies when a new dam becomes operational in the Lancang. Naturally, information on the past filling strategies could also be used when negotiating the filling of new dams—as for the case of the Grand Ethiopian Renaissance Dam (Y. Zhang, Erkyihum, and Block, 2016; Basheer et al., 2020)—a more desirable and cooperative policy that does not seem to be on the horizon.

In many ungauged or disputed river basins, like the Mekong, the characterization of hydrological alterations is typically based on "static" indicators that relate the storage capacity to the average annual discharge volume (Günther Grill, Dallaire, et al., 2014; Günther Grill, Lehner, et al., 2015). By coupling actual storage time series with discharge data, we can go beyond this first, fundamental, characterization and provide a gateway for a more nuanced understanding of how, and when, reservoir operations affect downstream hydrological processes (Bonnema and F. Hossain, 2017). In that regard, our results for the Lancang indicate that the fraction of natural flow actively controlled by dams (in Northern Thailand and Laos) changes on a monthly basis: reservoirs hold up to $\sim$ 50 % of the natural flow during the wet season and control almost 89 % of the dry season flow coming out of Lancang. Interestingly, we also found that this periodic pattern is not much affected by the hydrometeorological conditions—like the 2019-2020 drought—partially explaining the complaints and fears of the downstream countries (Eyler and Weatherby, 2020).

From a more technical perspective, another research area that might be influenced by our results is the development of large-scale hydrological models for the Mekong Basin. Hydrologists are indeed increasingly interested in the representation of water reservoir storage and operations, a modeling problem that has long relied on generic reservoir release schemes (Hanasaki, Kanae, and Oki, 2006). Recent research has shown that the nuances of operations at individual dams are better captured by hydrological models when building on high-resolution data available for each dam (Turner, Doering, and Voisin, 2020). In this regard, we believe our storage and water level time series provide an opportunity for testing and improving the many hydrological models developed for the Mekong Basin (Hoang et al., 2019; Yang Yu et al., 2019; Dang, Chowdhury, and Galelli, 2020; Yun et al., 2020; Shin et al., 2020; Do et al., 2020). A complementary research direction is the creation of additional datasets for other key variables, such as water temperature or suspended sediment concentrations, which can also be observed, or inferred, from satellite observations (Beveridge, F. Hossain, and Bonnema, 2020; Bonnema, F. Hossain, et al., 2020; Ahmad et al., 2021).

Like any other numerical modeling study, this work also builds on a few modeling assumptions that are worth being discussed. First, the storage time series we developed have a monthly resolution. As shown in Fig. A.1, this resolution is sufficient to study reservoir storage dynamics in the Lancang—as well as their impacts on downstream discharge—but it is undoubtedly that the availability of weekly or daily data would further expand the scope of research on transboundary basins. Daily data could be used, for instance, to study the nuances of emergency releases or sudden changes in river discharge. Second, Landsat images provide the best compromise of spatiotemporal resolution and time span, but they do require an image enhancement process. The

development of WSA algorithms is an area warranting further research, since studying dams built in the past decades must almost necessarily build on Landsat images. This is a nonnegligible factor when considering that many dams have been recently constructed in the tropics, where cloud cover is common during the rain season. Third, the analysis of reservoir filling strategies requires the use of modeled discharge, a problem that could be avoided if riparian countries shared river discharge data. The model validation suggests that the characterization of the filling strategies is not affected by the use of a model, which, importantly, is directly driven by inferred storage data. As mentioned, above the integration of such data with process-based hydrological models is a very active research area that will hopefully lead to even more accurate models.

Looking forward, we should aim at repeating studies like this one at the scale of the entire river basin. Doing that would create a pathway to a robust attribution analysis of the recent droughts that have affected the Mekong countries. It should be noted that such analysis is probably not yet within our reach: we know how runoff generation is spatially distributed (Shin et al., 2020), and we are gathering information on the operations of many reservoirs (Biswas, F. Hossain, Bonnema, Lee, et al., 2021), but we still have limited data on other anthropogenic interventions that arguably affect the overall water balance, such as irrigation activities in the western part of the basin. In turn, this reiterates the need for high-resolution data spanning across countries and socio-economic sectors.

2.6 Conclusions

In just a few decades, the Mekong River basin has undergone a rapid infrastructure development that has fostered economic growth but also damaged the environment and challenged the relation between riparian countries. A change in this status quo means conceiving cooperative water–energy policies that span across countries and socio-economic sectors (Schmitt et al., 2019; Siala et al., 2021). Aside from the political will, an important piece of the puzzle is the availability of open-source datasets that describe how big infrastructures have been operated. Since agreements on data sharing only provide piecemeal information (Johnson, 2020), the use of satellite imagery appears to be the only way to create unbiased observations available to the research community and local stakeholders. In this regard, our work complements the existing efforts for the region, bringing us one step closer to a complete understanding of China's management strategies for the Lancang's dams. Importantly, the lessons learned here could be readily applied to other transboundary river basins, where the lack of information on existing and planned dams is a major obstacle to open science and institutionalized cooperation.

Chapter 3

Calibrating macro-scale hydrological models in poorly gauged and heavily regulated basins

Publication

Vu, D. T., Dang, T. D., Galelli, S., & Hossain, F. (2022). Satellite observations reveal 13 years of reservoir filling strategies, operating rules, and hydrological alterations in the Upper Mekong River basin. *Hydrology and Earth System Sciences 26*(9), 2345–2364. https://doi.org/10.5194/hess-26-2345-2022.

3.1 Introduction

The past few years have witnessed an increase in the implementation of hydrological models to extensive domains, from large basins to the global scale (Döll et al., 2008; I. Haddeland et al., 2014; Nazemi and Wheater, 2015a; Nazemi and Wheater, 2015b; Bierkens, 2015). Such increase is driven by a variety of downstream applications, such as quantifying the potential impact of climate change on water resources (Vliet et al., 2016), characterizing the relationship between climate, water, and energy (Chowdhury, Dang, Hung T. T. Nguyen, et al., 2021), or predicting extreme events over multiple time scales (Vegad and Mishra, 2022). A fundamental point to consider is that the successful implementation of macro-scale models is often challenged by two problems. First, we often lack long and reliable time series of in situ observations of key hydrological processes, e.g., evapotranspiration, runoff, discharge (Hrachowitz et al., 2013). Second, there is also a lack of information and data on how hydraulic infrastructures are operated; a matter that we have only recently started to address (Vu et al., 2022; Steyaert et al., 2022). This is another important issue, since hydraulic infrastructures, such as dams, are ubiquitous and can heavily affect hydrological processes (Ingjerd Haddeland, Skaugen, and Lettenmaier, 2006; G. Grill et al., 2019). Importantly, both problems are exacerbated in transboundary river basins, where access to data is particularly difficult. This modelling backdrop creates a wealth of pitfalls for model calibration, with potential unintended consequences on the downstream applications of macro-scale hydrological models.

Looking at river discharge—the variable with respect to which macro-scale hydrological models are often calibrated—one easily notes that model calibration in poorly

gauged basins mostly relies on making the best of the available gauged data. In other words, the model calibration process is carried out by leveraging discharge data where they are available (e.g., Shin et al. (2020), Galelli et al. (2022), and Chuphal and Mishra (2023)). Naturally, doing so potentially leads to inadequate model calibration for the ungauged regions of a large basin. Other studies have explicitly dealt with the lack of discharge time series by inferring them from satellite data. As shown in Fig. 3.1, these studies can be categorized into two groups. One builds on the idea of first using in-situ data to develop a hydraulic model (accounting for the relationship between discharge and water level and/or river width) for estimating river discharge, and then using these estimates to carry out the model calibration (panel a) (e.g., Khan et al. (2012) and Tarpanelli et al. (2022)). Yet, this approach may still partially rely on in-situ data; hence, the solution for calibrating hydrological models in poorly gauged basins is often limited to the second approach (panel b), in which both models are calibrated concurrently (e.g., G. Liu et al. (2015), Sun et al. (2018), and Huang et al. (2020)). Here, a potential pitfall stands in the fact that estimation errors characterizing the first part (discharge estimation) may in turn affect the hydrological model, and vice versa. In other words, co-estimating the parameters of the hydraulic and hydrological models may bias their calibration, ultimately compromising their reliability. Considering the increasing number of remote-sensed discharge observations that could support such analyses (Birkinshaw et al., 2010; Papa et al., 2012; Biancamaria, Lettenmaier, and Pavelsky, 2016), it is paramount to explore the pitfalls that could affect the model calibration process.

In this study, we thus develop and demonstrate a workflow to investigate three chief questions: (1) Does the joint calibration of hydraulic and hydrological models create any reliability issues? (2) In particular, to what extent is the hydrological model accuracy influenced by the parameterization of the hydraulic model? (3) How can we make the calibration exercise less prone to potential pitfalls? We answer these questions for an implementation of the VIC-Res hydrological model for the Upper Mekong River Basin (Dang, Chowdhury, and Galelli, 2020), an area characterized by the unavailability of discharge observations as well as major hydrological alterations caused by dam development (Hecht et al., 2019). To generate discharge time series for the calibration of VIC-Res, we use satellite altimetry data and a hydraulic model (based on the Manning's equation) that is also identified from satellite data. In our framework, we first use Global Sensitivity Analysis to demonstrate the existence of a pronounced co-dependence between the parameterization of the hydraulic model and the modelling accuracy of VIC-Res. To break this co-dependence, we leverage the results of the sensitivity analysis to constrain the parameterization of the hydraulic model and thus safely inform the calibration of VIC-Res, which is ultimately carried out using a multi-objective optimization approach.

3.2 Study site, model domain, and gauging stations

In this section, we provide information on our study site, the spatial domain of the hydrological model, and the availability of observed and remote-sensed discharge data.

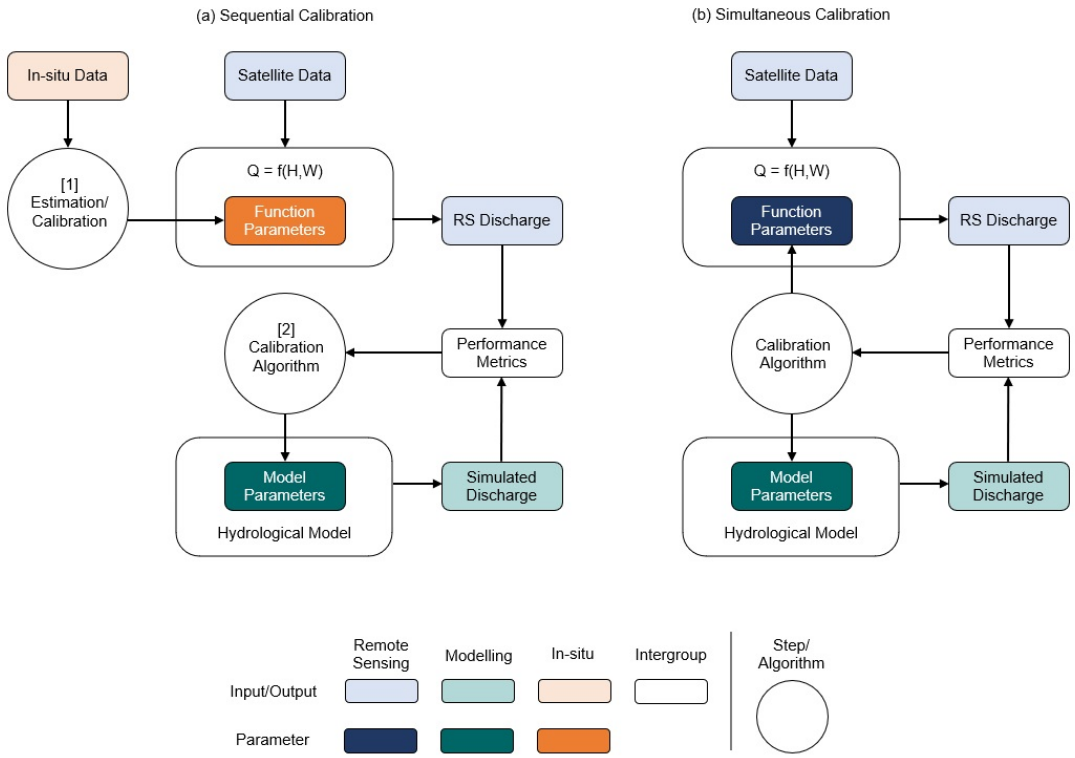

FIGURE 3.1: Two approaches to the calibration of macro-scale hydrological models with discharge data retrieved from satellite data. With the sequential calibration, the discharge data are first estimated using a hydraulic model linking water level (H) and/or river width (W) to discharge (Q), and then used to calibrate the hydrological model (a). With the second approach, both models are calibrated simultaneously (b).

3.2.1 The Lancang-Mekong River Basin

Spanning an area of about 795 000 km^2, the Mekong River Basin is the largest transboundary basin in Southeast Asia. The river is 4350 km long and stretches in a northwest-southeast direction from the Tibetan Plateau (approximately 5200 m a.s.l.) to the East Vietnam Sea (Fig. 3.2a). The basin can be roughly divided into two parts, namely the Upper Mekong (also known as the Lancang, in China) and the Lower Mekong, which is shared by five countries (Myanmar, Thailand, Laos, Cambodia, and Vietnam).

The Lancang accounts for 45 % of the river length, 21 % of the catchment area, and 16 % of the annual discharge of the entire Mekong (MRC, 2009). The complex topography of the Lancang Basin (high mountains and low valleys) contributes to the uneven spatial distribution of precipitation, which ranges from 600 mm/year in the Tibetan Plateau to 1700 mm/year in the mountains of Yunnan. Meanwhile, the monsoonal climate causes an uneven temporal distribution of precipitation, with 70 %-80 % of precipitation arriving in the wet season (June to November) (Yun et al., 2020).

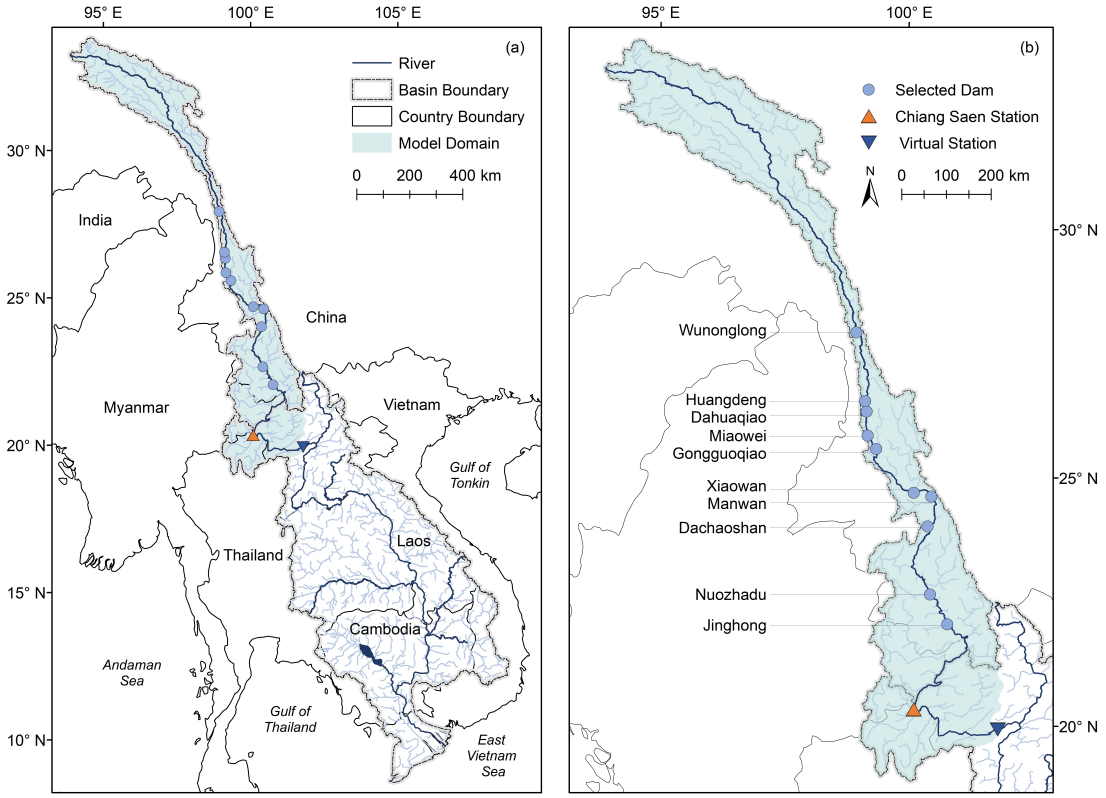

FIGURE 3.2: The Mekong River Basin (a) and the Lancang River Basin (b). In both panels, we illustrate the location of the gauging station (Chiang Saen), virtual gauging station, and ten large hydropower dams on the main stem of the Lancang with a volume larger than 100 million m^3 each, all included in the hydrological model. All dams are operational as of December 2020. The light green area is the spatial domain of the hydrological model.

Because of the advantageous topography and abundant water availability, the Lancang River Basin has become a hotspot for hydropower development. Indeed, the Lancang dam system—developed during the past three decades—consists of more than 35 hydropower dams (WLE Mekong, n.d.), including 10 large dams on the main stem with a volume larger than 100 MCM (Million Cubic Meters) each (see their location in Fig. 3.2b and specifications in Table A.1). The system has a total capacity of more than 42 000 MCM and can control up to 55 % of the annual flow to Northern Thailand and Laos. The Lancang River Basin is an excellent example of a transboundary and heavily regulated river with limited information on dam operations: initiatives on the sharing of year-round water data are still in their infancy (Johnson, 2020), so the only data available to the public are those retrieved from satellite data (e.g., Bonnema and F. Hossain (2017), Biswas, F. Hossain, Bonnema, Lee, et al. (2021), and Vu et al. (2022)). Time series of river discharge measured within China's political boundaries are not available.

3.2.2 Model domain and study period

The spatial domain of our hydrological model is the light green area illustrated in Fig. 3.2. This domain corresponds to the Lancang Basin (namely the area falling within China's political boundaries), plus an additional area spanning across Myanmar, Thailand, and Laos. Note that the domain of hydrological models focusing on the Lancang is typically 'closed' at Chiang Saen (e.g., Dang, Chowdhury, and Galelli (2020)), where the first gauging station with publicly-available data is located. Here, we slightly extend the domain so as to account for the location of a virtual gauging station (see Sect. 3.2.3). The simulation period goes from 2009 to 2018 and thus comprises the main development of the Lancang reservoir system, including the filling period of the two largest reservoirs, Xiaowan and Nuozhadu, which account for ∼85 % of the total system's storage (Vu et al., 2022).

3.2.3 Gauging stations

As mentioned above, the first gauging station with publicly-available data is Chiang Saen, located in Northern Thailand, about 350 km from Jinghong dam (Fig. 3.3). Daily water level and discharge at the station have been collected since 1990 by the Mekong River Commission (MCR) and are available on its online data portal (https://portal.mrcmekong.org/). Since we developed a methodology for calibrating models in ungauged river basins, these data are used only for model validation.

To infer the discharge time series needed for model calibration, we sought for locations around Chiang Saen where altimetry water level data are available (Fig. 3.3). From these data, one can try to infer the river discharge. These data are collected by multiple satellites (i.e., EnviSat, Jason-2/3, and Sentinel-3A) and are available in the Database for Hydrological Time Series of Inland Waters (DAHITI, https://dahiti.dgfi.tum.de/). In this study, we choose the location 1422 (Jason-2/3)—about 280 km downstream of Chiang Saen—as our *virtual* gauging station (virtual station hereafter). This is because of two reasons. First, the temporal coverage of data at the chosen location covers our study period (see the bottom panel in Fig. 3.3). Second, the temporal resolution of Jason-2/3 (10 days) is finer than the one of EnviSat (35 days) and Sentinel-3A (27 days). It is also worth noting that another database, HydroWeb (https://hydroweb.theia-land.fr/), provides (Sentinel-3A/B) altimetry water level data for a number of locations in our study site. However, these data have the same temporal resolution and coverage of the Sentinel-3A data provided by DAHITI, which makes them unsuitable for our study.

3.3 Methodology

The numerical framework developed for our study consists of two main modelling components, illustrated in Fig. 3.4. We model the hydrological processes within the Lancang Basin with VIC-Res, whose routing module includes an explicit representation of reservoir operations (Sect. 3.3.1). The discharge data at the virtual station used to calibrate VIC-Res are generated by a second model, namely a rating curve based on the Manning's equation (Sect. 3.3.2). In our approach, we first use Global Sensitivity Analysis to explore the relationship between the parameterization of the rating

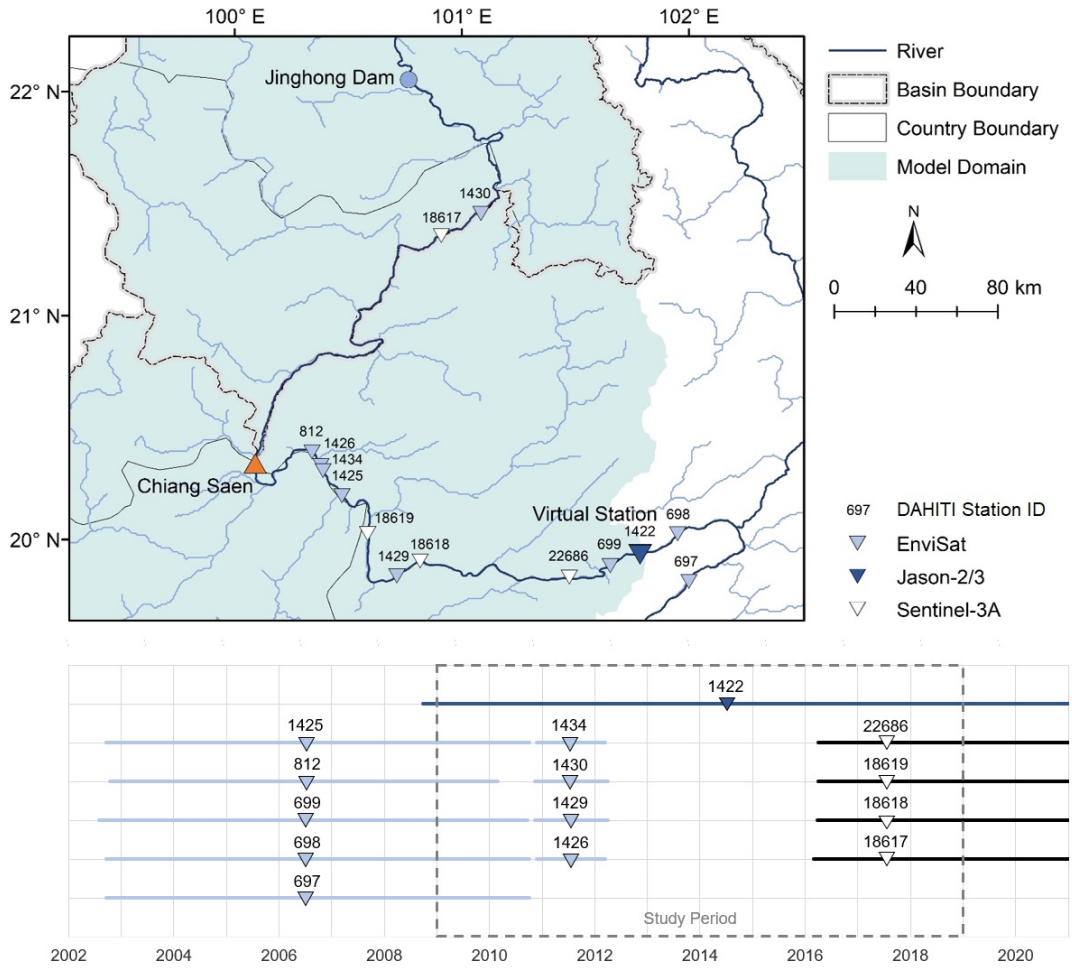

FIGURE 3.3: Gauging stations in our study site. The upper panel illustrates the location of Chiang Saen and the virtual station. The map also shows the locations in which altimetry water level data are available. The data are collected by multiple satellites—namely EnviSat (light blue triangle), Jason-2/3 (dark blue triangle), and Sentinel-3A (white triangle)—and are processed by DAHITI. The number above each triangle corresponds to the station ID in DAHITI. The bottom panel illustrates the temporal coverage of data in each location, constrained by the operational period of the satellites. Only data at the location 1422 (Jason-2/3) have a temporal coverage covering our study period.

curve and the accuracy of VIC-Res (Section 3.3.3). Then, we use the knowledge gained through the sensitivity analysis to calibrate and validate VIC-Res.

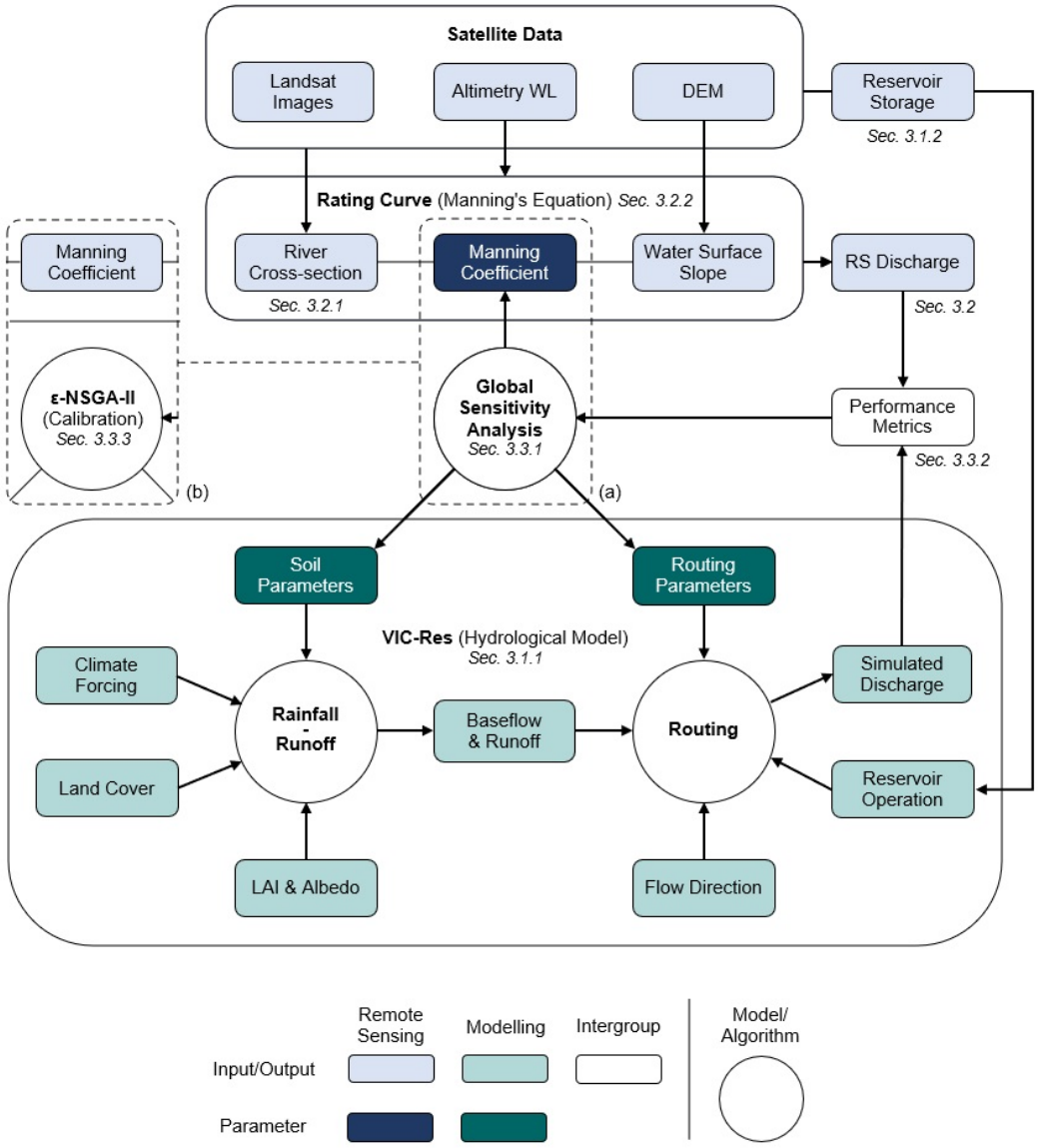

FIGURE 3.4: Flowchart illustrating our numerical framework. The VIC-Res model (green boxes) includes a rainfall-runoff and a routing module. The latter explicitly simulates reservoir operations using data retrieved from satellite observations. The discharge data used to calibrate VIC-Res are estimated from altimetry water levels through a rating curve, which is based on Manning's equation and developed using multiple satellite data (Landsat images, altimetry water level, and DEM). All remote sensing items are represented by blue boxes. The relationship between the parameterization of the Manning's equation (dark blue box) and the performance of VIC-Res is assessed and quantified via Global Sensitivity Analysis (a). Based on the results of the sensitivity analysis, we then set a value of the Manning's coefficient and calibrate the parameters of VIC-Res using the ε-NSGA-II algorithm (b).

3.3.1 Modelling hydrological processes and reservoir operations

Hydrological model

The hydrological model used in this study is VIC-Res (Dang, Chowdhury, and Galelli, 2020), a novel variant of VIC, which is a macro-scale, semi-distributed hydrological model developed by the University of Washington (Liang et al., 2014). Both VIC and VIC-Res consist of two modules, namely a rainfall-runoff and a routing module (Fig. 3.4). In the rainfall-runoff module, the study region is divided into computational cells with a customizable cell size (0.0625° in this study). For each cell, the key hydrological processes (evapotranspiration, infiltration, baseflow, and runoff) are calculated as a function of various inputs, including climate forcing (e.g., precipitation, temperature, wind speed), land cover, Leaf Area Index, and albedo. In the routing module, simulated baseflow and runoff produced by the first module are routed throughout the river network, with the routing process modelled by the linearized Saint-Venant equation (Lohmann, Nolte-Holube, and Raschke, 1996; Lohmann, Raschke, et al., 1998).

Improving on the VIC model, VIC-Res includes an explicit representation of water reservoir operations. For each reservoir in the study region, the model solves the storage mass balance and calculates the reservoir release. Specifically, we leverage information on modeled inflow and estimated storage (see Sect. 3.3.1). These two variables are combined with information on evaporation (simulated using the estimated water surface area and evaporation rates calculated with the Penman equation) to invert the mass balance equation, yielding the reservoir release. Additional details on VIC-Res, including alternative approaches to reservoir operations, are described in Dang, Vu, et al. (2020).

In our VIC-Res model, we calibrate 7 soil parameters and 2 routing parameters (see Table 3.1). The soil parameters controlling the rainfall-runoff process are b, D_{max}, D_S, W_S, c, d_1, and d_2. To be more specific, the parameter b is the VIC curve parameter, which determines the infiltration capacity and surface runoff amount generated by each cell (Ren-Jun, 1992; Todini, 1996). In particular, higher values of b produce less infiltration and more surface runoff. D_{max}, D_S, W_S, and c are the baseflow parameters, which influence the shape of the baseflow curve (Franchini and Pacciani, 1991). Specifically, D_{max} is the maximum velocity of baseflow, D_S is the fraction of D_{max} at which non-linear baseflow begins, while W_S is the fraction of maximum soil moisture at which non-linear baseflow begins. The parameter c is the exponent used in the baseflow curve. d_1 and d_2 are the thickness of the two soil layers. Thicker layers increase the water storage capacity, and hence increase the evaporation losses. Thicker soil layers also delay the seasonal peak flow. The routing parameters are flow velocity (v) and flow diffusion (d_f).

The data used in our VIC-Res model consist of climate forcing data, land use and cover, Leaf Area Index (LAI), albedo, flow direction, and time series of reservoir storage volume. Climate forcing data include daily precipitation data retrieved from the CHIRPS-2.0 dataset, daily maximum and minimum temperature, and wind speed (retrieved from the ERA5 dataset). We collect land use and cover data from the Global Land Cover Characterization (GLCC) dataset, and soil data from the Harmonized World Soil Database (HWSD). Monthly LAI and albedo are derived from the Terra MODIS

TABLE 3.1: Soil parameters controlling the rainfall-runoff process and routing parameters in VIC-Res. The last column shows the range of each parameter considered in this study, also adopted in previous studies (e.g., Dan et al. (2012), Park and Markus (2014), Xue et al. (2015), and Wi et al. (2017)).

Parameter		Unit	Description	Range
Soil	b	-	Variable Infiltration Capacity curve parameter	(0, 0.9]
	D_{max}	mm/d	Maximum velocity of baseflow	(0, 30]
	D_S	-	Fraction of D_{max} where non-linear baseflow occurs	(0, 1)
	W_S	-	Fraction of maximum soil moisture where non-linear baseflow occurs	(0, 1)
	c	-	Exponent used in baseflow curve	[1, 3]
	d_1	m	Thickness of the upper soil layer	[0.05, 0.25]
	d_2	m	Thickness of the lower soil layer	[0.3, 1.5]
Routing	v	m/s	Flow velocity	[0.5, 5]
	d_f	m^2/s	Flow diffusion	[200, 4000]

satellite images, while the flow direction is calculated from the SRTM-DEM data. The monthly time series of reservoir storage volume are reconstructed from satellite data, as explained next.

Reservoir operations

To capture the actual operations of reservoirs, we use monthly time series of reservoir storage volume reconstructed from satellite data by Vu et al., 2022. Specifically, the time series of reservoir storage volume are obtained from Landsat images (Landsat 5 available from 1984 to 2013, Landsat 7 from 1999 to 2022, and Landsat 8 from 2013 to present) and a digital elevation model (SRTM-DEM). The time series are created through three steps. First, the relationship between water surface area and storage volume (the area–storage curve) for each reservoir is calculated from DEM data. Then, the reservoir water surface area is estimated from Landsat images by a water surface area estimation algorithm that removes the effects of clouds and other disturbances (Huilin Gao, C. Birkett, and Lettenmaier, 2012; S. Zhang, Huilin Gao, and Naz, 2014). Finally, the storage volume is inferred from the water surface area through the area–storage curve. The results obtained from Landsat images are validated with altimetry water levels (Jason 2 available from 2008 to 2016, Jason 3 from 2016 to present, and Sentinel 3 from 2016 to present) for the reservoirs where altimetry water levels are available. Since the VIC-Res model adopts a daily simulation time step, the monthly time series of reservoir storage volume is interpolated to daily values.

3.3.2 Inferring discharge data

To handle the lack of discharge data for model calibration, we again resort to satellite data. Specifically, we convert altimetry water levels (Jason 2/3) to discharge through a rating curve specified for the location of the virtual station (see Fig. 3.4). The rating curve (i.e., Manning's equation) is identified based on the information on river cross-section and water surface slope at the virtual station, which are also derived from satellite data.

River cross-section

We construct the river cross-section at the virtual station by using multiple satellite products (see Fig. B.1a). First, we use a digital elevation model (SRTM-DEM), which has a spatial resolution of 30 m, to obtain the portion of the cross-section above the water level at the observation time of the SRTM satellite (February 2000). To extend the information available to estimate the river cross-section, we then pair data on river widths at the virtual station with the corresponding water levels (temporal nearest observations of two satellites that provide river widths and water levels) (Bose et al., 2021). River widths are estimated from the water pixels—classified from Landsat images based on Normalized Difference Water Index (NDWI)—along the river cross-section. NDWI is calculated using the Green and Near-infrared bands of Landsat images (NDWI = (Green band - Near-infrared band)/(Green band + Near-infrared band)) (Zhai et al., 2015). All these bands have a spatial resolution of 30 m. Meanwhile, the water level data are processed from Jason-2/3 altimetry satellite data provided by DAHITI. Finally, for each river bank, we use a regression model (sixth-degree polynomial) which is the best fit to the data points obtained from the two first steps. The two models help us extrapolate the portion of the river cross-section under the lowest water level observed by the satellites. It is worth noting that the approach works best for river banks in natural conditions, where it is possible to infer the relation between river widths and water levels. It would be challenging to apply this approach at Chiang Saen, for example, where the river banks have been engineered.

Rating curve

We construct the rating curve at the virtual station with the Manning's equation (Eq. 3.1):

$$Q = \frac{A^{5/3} S^{1/2}}{P^{2/3} n}, \tag{3.1}$$

where Q, A, and P are discharge, river cross-section area, and wet perimeter corresponding to the water depth D (see Fig. B.1b). As explained next, A and P are calculated from the river cross-section for different values of water depth D. S is the hydraulic slope, estimated from DEM data (which reflects the water surface slope at the observation time). n is the Manning's coefficient (riverbed roughness). Following Chow (1959) and Engineering ToolBox (2004), we assume that it ranges from 0.03 to 0.06.

The rating curve is constructed in two steps. First, we use Eq. 3.1 to estimate the discharge corresponding to each water depth with regular intervals of one meter (e.g.,

0, 1, 2 m). After this step, we have at hand a number of data points, each containing a value of water depth and its corresponding discharge. Then, we fit the data points by a power curve. This translates into our rating curve. Note that when converting altimetry water level to discharge using the rating curve, we convert altimetry water level to water depth by deducting the river bed elevation (Fig. B.1b).

3.3.3 Sensitivity analysis and model calibration

Sensitivity analysis

We carry out a Global Sensitivity Analysis (Pianosi et al., 2016) to study the relationship between the performance of VIC-Res and the parameterization of the rating curve. We investigate a total of 10 model parameters, including 7 soil parameters of the rainfall-runoff module, 2 parameters of the routing module, and the Manning's coefficient appearing in the rating curve. We use Latin Hypercube Sampling to create 1000 samples in the 10-dimensional parameter space defined by the ranges given in Sects. 3.3.1 and 3.3.2. For each parameter sample, we run a simulation over the period 2009–2018 (after a warm-up period from 2005 to 2008), and reconstruct discharge data for the same period with the rating curve. We then compare reconstructed and simulated discharges through four performance metrics, which are described in the next subsection. Having built this input (parameters) and output (performance metrics) dataset, we analyse the co-dependence between the performance of VIC-Res and the Manning's coefficient. We also identify the parameter samples that map into the top 25 % values of each performance metric and analyze if, and how, such constraining on performances maps back into a constraining of the parameter values. The simulation experiment is run on an Intel (R) Xeon (R) W-2175 CPU 2.50 GHz with 128 GB RAM running Linux Ubuntu 18.04. The total running time is about 200 hours.

Performance metrics

The performance metrics are calculated by comparing the simulated (by VIC-Res) and remote-sensed discharge at the virtual station. Because the temporal resolution of remote-sensed discharge is defined by the revisit time of altimetry satellite (approximately 10 days for Jason2/3), we calculate the performance metrics using the data of all days in which altimetry water levels are available. Among the several metrics available in literature (Dawson, Abrahart, and See, 2010), we chose four metrics that explicitly capture different aspects of modelling accuracy. These are the Nash–Sutcliffe Efficiency (NSE), Transformed Root Mean Square Error (TRMSE), Mean Squared Derivative Error (MSDE), and Runoff Coefficient Error (ROCE). NSE and TRMSE assess the model performance on high and low flows, respectively, while MSDE accounts for the shape of the hydrograph timing errors, and noisy signals. Finally, ROCE assesses the overall water balance (Reed et al., 2013). The metrics are defined as follows:

$$NSE = 1 - \frac{\sum_{t=1}^{n} \left(Q_{Sim,t} - Q_{RS,t}\right)^2}{\sum_{t=1}^{n} \left(Q_{RS,t}^{t} - \overline{Q_{RS}}\right)^2}, \tag{3.2}$$

where n is the number of satellite altimetry water level observations, $Q_{Sim,t}$ and $Q_{RS,t}$ are the simulated and remote-sensed discharge at the virtual station (for the observation number t), and $\overline{Q_{RS}}$ is the mean of the remote-sensed discharge.

$$TRMSE = \sqrt{\frac{1}{n}\sum_{t=1}^{n}(z_{Sim,t} - z_{RS,t})^2}, \tag{3.3}$$

where $z_{sim,t}$ and $z_{RS,t}$ represent the value of the simulated and remote-sensed discharge at the virtual station (for the observation number t), both transformed by the expression $z = \frac{(1+Q)^{\lambda}-1}{\lambda}, (\lambda = 0.3)$. In other words, λ scales down the values of the discharge, thus emphasizing the errors on low flows.

$$MSDE = \frac{1}{n-1}\sum_{t=1}^{n}\left((Q_{RS,t} - Q_{RS,t-1}) - (Q_{Sim,t} - Q_{Sim,t-1})\right)^2, \tag{3.4}$$

$$ROCE = abs\left(\frac{\overline{Q_{Sim}}}{\overline{P}} - \frac{\overline{Q_{RS}}}{\overline{P}}\right), \tag{3.5}$$

where $\overline{Q_{Sim}}$ is the mean of the simulated discharge at the virtual station, and $\overline{P}$ is the mean annual rainfall.

Model calibration

As we shall see, the global sensitivity analysis helps us understand the relationship between the performance of VIC-Res and the parameterization of the rating curve. Moreover, by identifying the parameter samples that map into high values of the performance metrics (here the top 25 %), the analysis helps us narrow down the range of variability of (at least some of) the model parameters. However, one may still want to complete the model calibration by further seeking for the value of the VIC-Res parameters that optimize the performance metrics. To this purpose, we couple VIC-Res with ε-NSGA-II, a multi-objective evolutionary algorithm widely used for hydrological modelling applications (Reed et al., 2013; Dang, Chowdhury, and Galelli, 2020). Here, the decision variables are the 9 parameters of VIC-Res, while the objective function is a vector consisting of the 4 metrics described in Sect. 3.3.3. Similarly to the sensitivity analysis, all metrics are calculated via simulation over the period 2008–2018, with a spin-up period going from 2005 to 2008. The ε-NSGA-II is set up with ε = 0.001, an initial population size of 10, and a number of function evaluations equal to 100. All performance metrics are normalized between 0 and 1. The calibration exercise is carried out on 10 independent trials, with the best (Pareto-efficient) solutions selected across the 10 calibration exercises. The total run time is about 210 hours (using the same computational infrastructure adopted for the sensitivity analysis).

3.4 Results

Here, we move across 3 steps. First, we illustrate the results leading to the estimation of a discharge time series at the virtual station, including the identification of the river cross-section and rating curve (Sect. 3.4.1). Then, we use sensitivity analysis to

show that there exists a co-dependence between the Manning's coefficient and the performance of VIC-Res, and we propose an approach to overcome this potential issue (Sect. 3.4.2). We finally calibrate VIC-Res and validate its performance using observed discharge data at Chiang Sean (Sect. 3.4.3).

3.4.1 Estimation of the remote-sensed discharge at the virtual station

River cross-section

Fig. 3.5a shows the river cross-section at the virtual station, constructed through the use of multiple satellite data. Specifically, each dark blue bar represents a 30 m cell of the SRTM-DEM lying along the river cross-section. These bars are connected by a series of segments representing an estimate of the cross-section above the water surface at the observation time of the SRTM satellite. That specific water surface is depicted by the horizontal dark blue line at the elevation of 293 m. The light blue lines indicate the river widths derived from 19 Landsat-5 images and water levels obtained from Jason-2/3. Additional information about these images, water levels, and corresponding collection dates are reported in Table B.1. Finally, the dotted blue line represents the cross-section below the lowest observed water level. This line is created via extrapolation by 2 regression models (sixth-degree polynomial), which are fitted to the observations retrieved from DEM, Landsat-5, and Jason-2/3 (11 and 14 data points for the left and right banks, respectively).

Rating curve

With the river cross-section at hand, we estimate the rating curve at the virtual station using the Manning's equation (Eq. 3.1). Since the value of the Manning's coefficient n is unknown, the value of the estimated discharge Q depends not only on the water depth D but also on n, that is:

$$Q = \frac{0.161 D^{2.357}}{n} \tag{3.6}$$

In Fig. 3.5b, we plot the range of variability of the rating curve corresponding to values of n varying between 0.03 to 0.06 (Sect. 3.3.2). This range is represented by the light blue band. Note the large increase in river discharge estimates corresponding to a depth larger than 20 m. In this figure, we also report 3 rating curves corresponding to 3 specific values of n, namely minimum (dotted blue line), average (dark blue line), and maximum (dashed blue line).

Remote-sensed discharge

Using the rating curve and water depth (converted from Jason-2/3 altimetry water level data), we estimate 298 discharge data points at the virtual station during the period 2009–2018 (Fig. 3.5c). The light blue band represents the envelope of the variability of the discharge corresponding to values of n ranging between 0.03 and 0.06. The figure also depicts the discharge time series corresponding to the average value of the Manning's coefficient (n = 0.045), plus an additional time series obtained by scaling the observed discharge at Chiang Saen by a coefficient (equal to 1.17) representing the

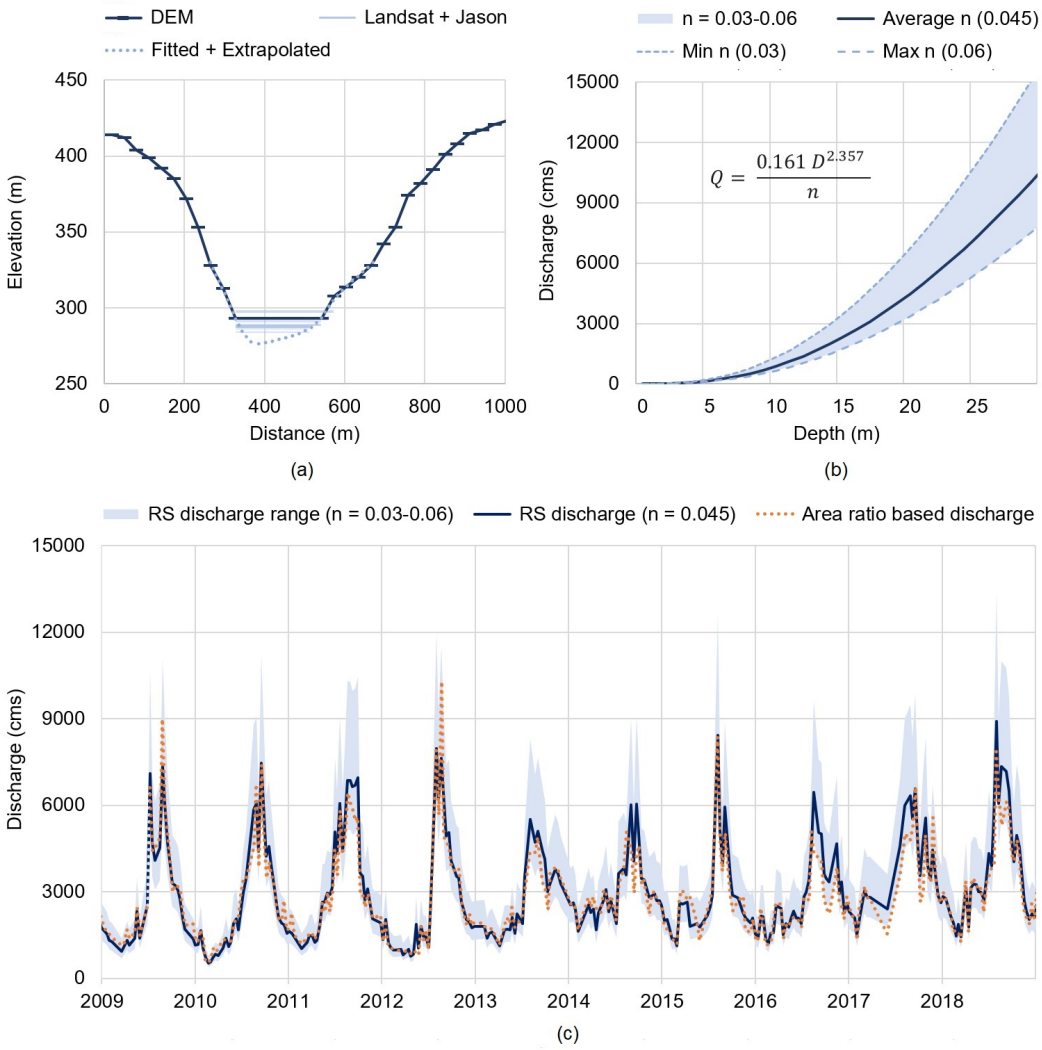

FIGURE 3.5: River cross-section at the virtual station constructed from multiple satellite data (a). The dark blue line is obtained from SRTM-DEM, while the light blue lines are retrieved by paring Landsat-derived river widths with Jason altimetry water levels. The dotted blue line is created by using two regression models, which are first fitted to the right and left banks and then extrapolated to the portion below the lowest observed water level. Range of variability of the rating curve (at the virtual station) for values of n ranging from 0.003 to 0.006 (light blue band) (b). In this plot, we also illustrate three rating curves corresponding to specific values of n: minimum (dotted blue line), average (dark blue line), and maximum (dashed blue line). Remote-sensed (RS) discharge at the virtual station (c). The light blue band represents the range of variability, with n varying from 0.03 to 0.06. The dark blue line is the estimated discharge with the average value of n (0.045). Note that this time series is relatively similar to the one obtained by scaling the discharge measured at Chiang Saen by the area ratio (equal to 1.17). That time series is depicted by the dotted orange line.

relative increase in drainage area between Chiang Saen and the virtual station (orange dotted line). A qualitative comparison of these estimated discharge values provides a few useful insights. First, there is large uncertainty in the discharge estimated during the summer monsoon season. This result is explained by the characteristics of the rating curve—the higher the value of D, the higher the uncertainty in Q (Fig. 3.5b). Second, there seems to be a reasonable agreement between the discharge time series corresponding to n = 0.045 and the one estimated from values observed at Chiang Sean. This implicitly validates the rating curve, further suggesting that the mean value of n might be a reasonable estimate. To further investigate this last point—and understand how the Manning's coefficient influences the performance of VIC-Res—we now move to the sensitivity analysis.

3.4.2 Sensitivity analysis

Co-dependence between VIC-Res performance and Manning's coefficient

The first fundamental step of our analysis is to understand whether co-estimating the Manning's coefficient and the parameters of the hydrological model (see Fig. 3.1) could bias the calibration process, ultimately limiting the reliability of VIC-Res. To answer this question, we leverage the results obtained by exploring via the simulation of 1000 different parameterizations of VIC-Res and Manning's equation.

In Fig. 3.6 (panels a, d, g, and j), we illustrate the relationship between the 4 metrics of performance calculated for VIC-Res (i.e., NSE, TRMSE, MSDE, and ROCE) and the value of the Manning's coefficient n. To aid the analysis, we highlight in darker color the parameterizations yielding the top 25 % performance (250 samples) with respect to each metric. For example, in Fig. 3.6a, the 250 samples with higher NSE are represented by the dark blue lines, while the 750 samples with lower NSE are represented by the light blue lines. The NSE threshold created by the top 25 % is equal to 0.48. Interestingly, when comparing these 4 panels, we see that the values of n corresponding to the best performance vary with the metric we consider. For example, the top 25 % performance in terms of NSE is given by values of n ranging between 0.03 and 0.054, while those giving the best performance for MSDE range between 0.037 and 0.06. This point is consolidated by panels b, e, h, and k, where we show the frequency distribution of n corresponding to the top 25 % performance for each metric. The minimum and maximum values we found for each distribution are [0.03, 0.054], [0.034, 0.06], [0.037, 0.06], and [0.033, 0.059] for NSE, TRMSE, MSDE, and ROCE, respectively. Note, also, how the median value of each distribution changes with the selected performance metric.

The explanation behind this result must be sought in the different aspects of modelling accuracy that are captured by the four metrics (see Sect. 3.3.3). Let's consider, for instance, NSE, a metric that emphasizes model performance on high flows: the parameterizations of VIC-Res achieving the top 25 % performance are those corresponding to smaller values of n, because those values translate (via the Manning's equation) into higher discharges. We observe, in other words, a co-dependence between the performance of VIC-Res and the Manning's coefficient: co-estimating the parameters of both models while focusing on NSE means calibrating the hydrological model on discharge data that are biased towards high flows (panel c). Similar conclusions can be drawn for TRMSE, MSDE, and ROCE. In this case, the values of n associated to the best TRMSE

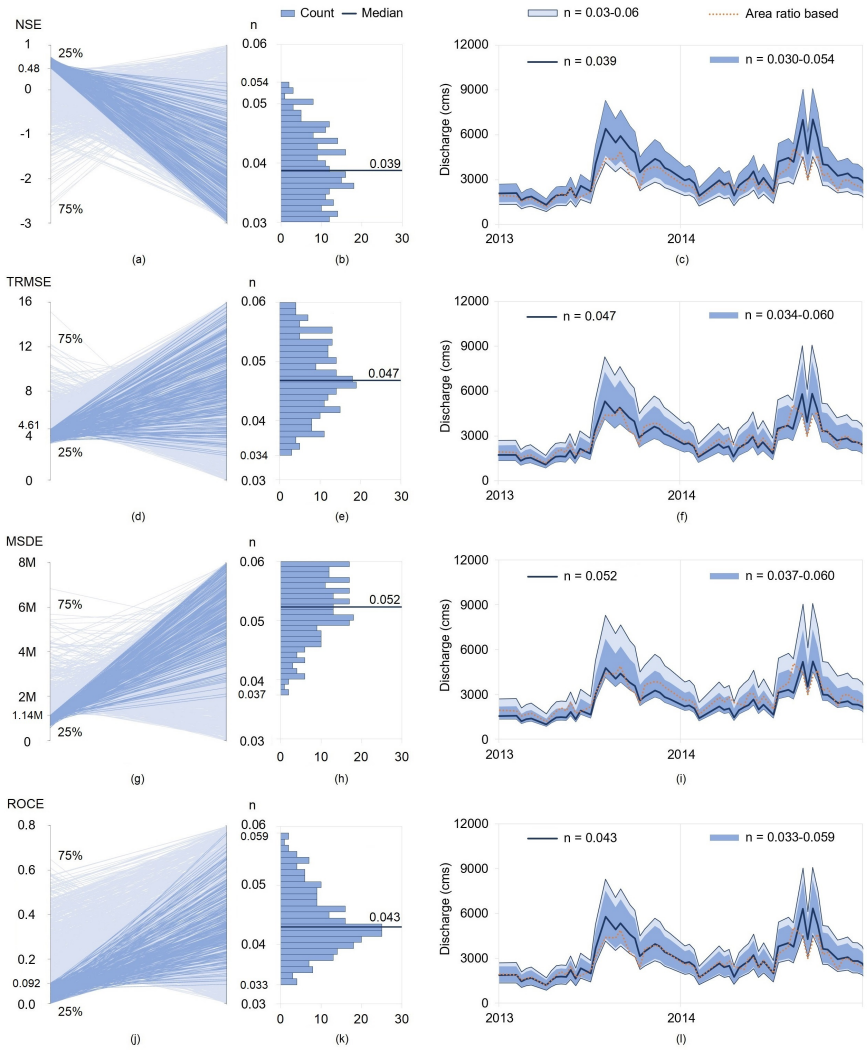

FIGURE 3.6: The first column contains 4 parallel-coordinate plots. In each plot, the left axis is a model performance metric (i.e., NSE, TRMSE, MSDE, and ROCE) while the right axis is the Manning's coefficient n. Each line corresponds to one of the 1000 parameterizations generated by Latin Hypercube sampling. The dark blue lines highlight the parameterizations yielding the top 25 % performance for each metric. The histograms in the second column illustrate the frequency distribution of n corresponding to these top 25 % parameterizations. The median is depicted by the dark blue line. In the last column, we report in light blue the range of variability of the discharge estimated with $n \in [0.03, 0.06]$ (this is the same range as in Fig. 3.5c), and in dark blue the range corresponding to the top 25 % performance for each metric. The black lines are the discharge corresponding to the 4 median values of n (see the second column) and the orange dotted line is the discharge estimated from observations at Chiang Saen via the area-ratio method. Note how the use of different performance metrics results in different ranges and different medians of the Manning's coefficient.

and MSDE performance shift upward, since both metrics emphasize model accuracy on lower flows (panels f and i). For ROCE, most values of n are concentrated around the median value of 0.043 (close to the mean of 0.45). This is because ROCE looks at the overall water balance, thereby requiring calibrating the hydrological models on discharge values that are more centered towards the bulk of the distribution (panel l).

Breaking the co-dependence

Having established that there can be a co-dependence between the performance of VIC-Res and the Manning's coefficient, we now turn our attention to a potential solution. Ideally, one would like to calibrate a hydrological model that performs well with respect to multiple performance metrics (Efstratiadis and Koutsoyiannis, 2010). Guided by this simple concept, we consider the parameterizations of VIC-Res and Manning's equation associated with the top 25 % performance with respect to all metrics (i.e., NSE, TRMSE, MSDE, and ROCE). This leaves us with 40 parameterizations, illustrated in Fig. 3.7. The first interesting point to note in the figure (right panel) is the empirical distribution of n. Focusing on satisfactory performance across multiple metrics means working with a narrow range of the Manning's coefficient concentrated around the median value of 0.046. As we shall see later, this means that the discharge values used to calibrate VIC-Res should not vary excessively, as we instead saw in Fig. 3.6.

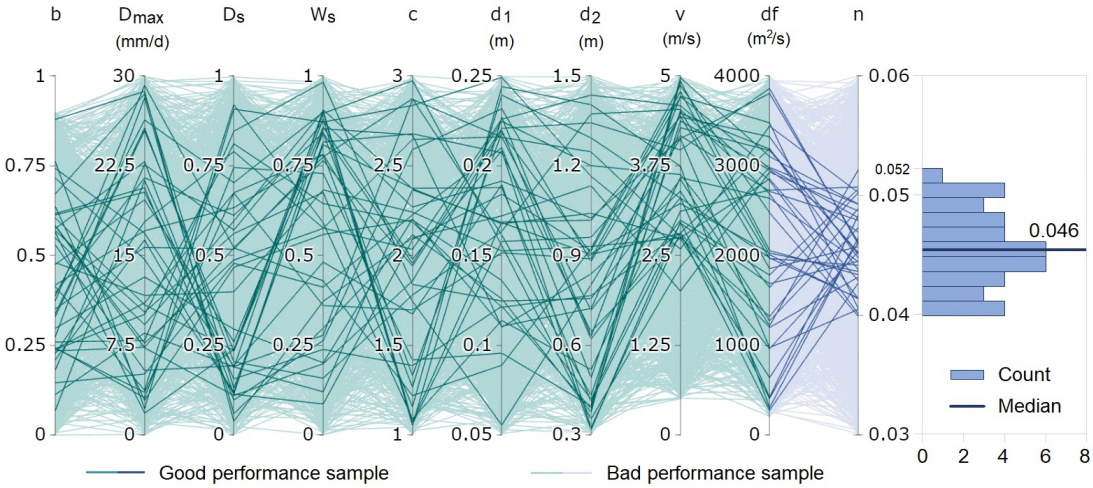

FIGURE 3.7: Parallel-coordinate plot illustrating the 1000 parameterizations explored in our sensitivity analysis. The first nine axes (green) represent the VIC-Res model parameters, while the last axis (blue) represents the Manning's coefficient n. Darker lines highlight the 40 parameterizations showing good performance on all metrics; these are identified by intersecting the four top 25 % parameterizations for each performance metric. The panel on the right illustrates the frequency distribution of n corresponding to the 40 selected parameterizations. The median of this distribution is 0.046.

The left panel of Fig. 3.7 illustrates the specific values of the parameterizations through a parallel-coordinate plot, in which each axis represents a parameter and each line is a

parameter sample. The 40 top-performing parameterizations are highlighted in bold, while the remaining 960 are depicted with a lighter color. Here, we notice that only the range of the flow velocity (v) can be narrowed down significantly (in addition to n, of course). Specifically, when considering only the 40 top-performing parameterizations, the range is reduced from $[0.5, 5]$ to $[2, 5]$. However, all the other parameters of VIC-Res cannot be constrained to narrower ranges—a common problem in macro-scale hydrological models, including VIC (Yeste et al., 2020). We will return to this issue in Sect. 3.5.

Narrowing the uncertainty in discharge data

How does the new parameterization of n impact the remote-sensed discharge data needed to calibrate the model? To answer this question, we focus on Fig. 3.8a, where we compare two envelops of variability, the one corresponding to $n \in [0.03, 0.06]$ (light blue envelope) and the one with $n \in [0.04, 0.052]$ (dark blue envelope). As expected, the range of remote-sensed discharge is narrowed down significantly, especially during the high flow periods. Another point that is worth noticing here is that the discharge time series corresponding to the median value of n (i.e., 0.046) is close to the time series estimated from the data available at Chiang Saen. This is a qualitative, yet informative, validation of the sensitivity analysis.

To complete the analysis, we finally compare the envelopes of variability produced by the Manning's equation and VIC-Res for the narrow range of n (panel b). The comparison shows encouraging results, since the range of simulated discharge (green envelope) is not too wide and it buffers around the remote-sensed one. Similar conclusions can be drawn when considering the monthly average simulated discharge (panel e). Looking at specific years, instead, we can note some inconsistencies between remote-sensed and simulated discharge, as shown in panels c and d. In one case (2014), the model seems to follow the river discharge fluctuations of the summer monsoon, while in the other case (2013), the simulated discharge after the flow peak (September–November) is ∼1.5 to 2.5 times higher than the remote-sensed (and area ratio based) discharge. We suspect the reason behind this is the uncertainty in the rainfall data that is typical of this region (Kabir, Pokhrel, and Felfelani, 2022).

3.4.3 Model calibration and validation performance

In our last step, we seek to reduce the uncertainty associated with the discharge simulated by VIC-Res presented in the previous section. To this purpose, we need to select a specific discharge time series with respect to which we can calibrate the model. Albeit arbitrary, a reasonable choice is the remote-sensed discharge corresponding to the median value of n, since (1) it does represent the envelope of variability produced by the Manning's equation and (2) it is rather close to the discharge at the virtual station estimated by scaling the discharge observed at Chiang Saen. Using this time series, we carry out a calibration task using the multi-objective evolutionary algorithm described in Sect. 3.3.3. From the 1100 solutions we obtained, we select the best-performing solutions by applying the same criteria used in the sensitivity analysis (i.e., top 25 % performance with respect to all 4 metrics). The envelope of variability of the simulated discharge corresponding to the twelve selected solutions is illustrated by the dark green

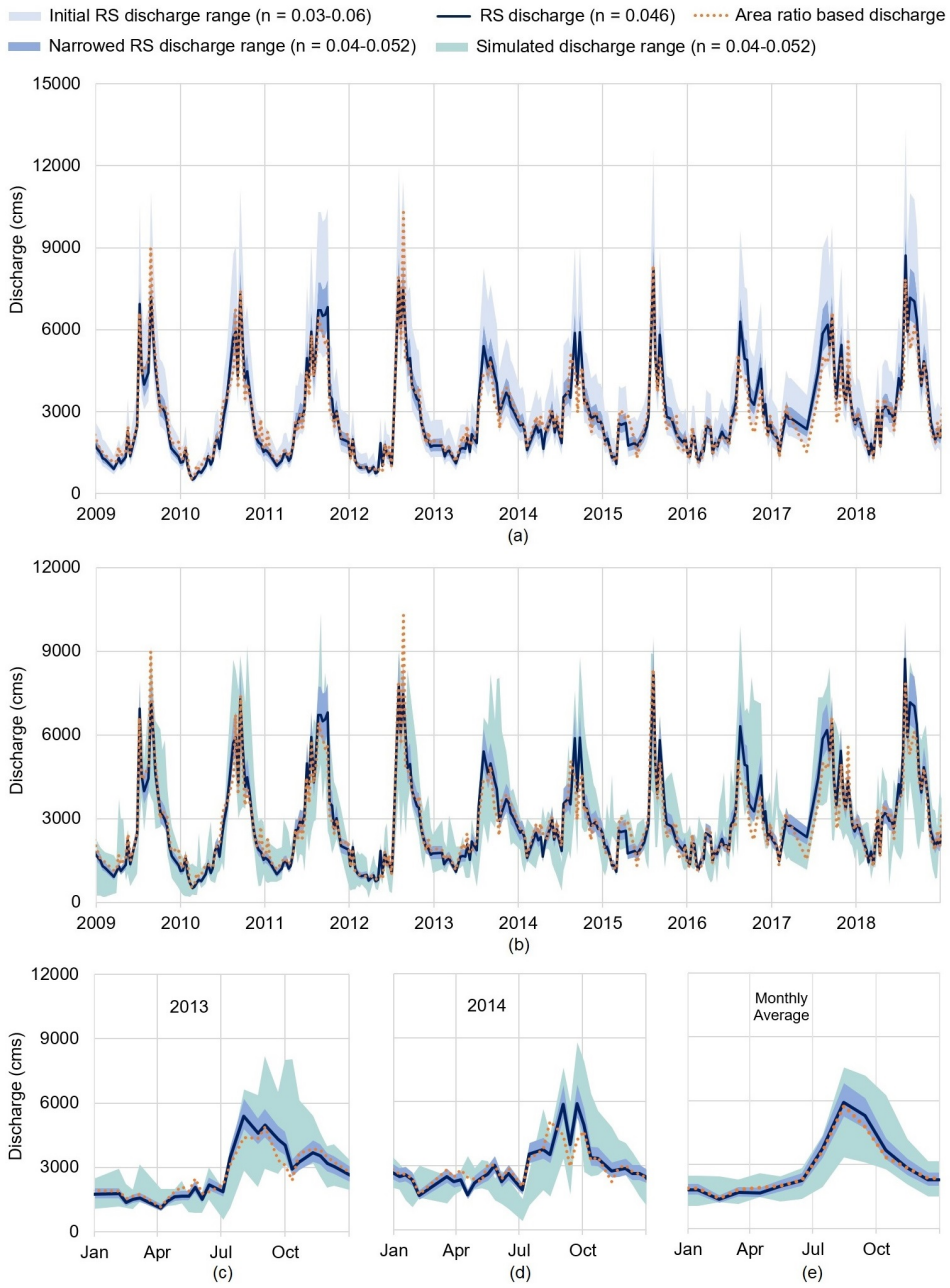

FIGURE 3.8: In panel a, we compare the range of variability of the remote-sensed (RS) discharge before and after sensitivity analysis. The two envelopes correspond to values of n belonging to $[0.03, 0.06]$ and $[0.04, 0.052]$. In the plot, we add the discharge values corresponding to the median value of n (0.046) and those estimated from the data at Chiang Saen (orange dotted line). In panel b, we compare the RS discharge against the discharge data simulated by VIC-Res. Both envelopes correspond to a value of $n \in [0.04, 0.052]$. In panels c, d, and e we focus on 2013, 2014, and average monthly discharge. The plots of other individual years are provided in Fig. B.2.

band in Fig. 3.9a, where it is contrasted against the envelope of variability generated by VIC-Res before this calibration step. As expected, the range of variability is narrowed significantly and is well in agreement with the remote-sensed discharge corresponding to a value of n of 0.046 (dark blue line) and the area ratio-based discharge (orange dotted line). The performance metrics of the twelve selected solutions—calculated by comparing simulated and remote-sensed discharge at the virtual station—are reasonable, with NSE, TRMSE, MSDE, and ROCE belonging to the ranges [0.686, 0.689], [3.337, 3.360], [890,904, 908,805], and [0.03, 0.04], respectively. The detailed performance of each solution is provided in Table B.2.

Finally, we report in Fig. 3.9b the performance of the model validation at Chiang Saen station. The variation range of the simulated discharge corresponding to the twelve selected solutions (dark green band) is much narrower than the one corresponding to the 40 solutions selected by the sensitivity analysis (light green band). The new envelope of variability is also well in agreement with the observed discharge at Chiang Saen station (orange dotted line). The performance metrics of the twelve selected solutions show only a small decay when compared against the one achieved at the virtual station—NSE, TRMSE, MSDE, and ROCE belong to the range [0.594, 0.616], [3.891, 3.935], [1,057,966, 1,071,282], and [0.169, 0.195] respectively. (The detailed performance of each solution is provided in Table B.3.) We note that similar results are achieved by selecting all 58 solutions belonging to the Pareto front, as shown in Fig. B.3, Tables B.4 and B.5. This is a remarkable result if we consider that no gauged discharge data were used to calibrate the model.

3.5 Discussion and Conclusions

Our study contributes an approach for calibrating macro-scale hydrological models in poorly gauged and heavily regulated basins. The approach uses satellite data to infer both the discharge data used for model calibration and the reservoir operations included in the hydrological model. Unlike previous studies, our approach uses Global Sensitivity Analysis to assess the biases that could be introduced when co-calibrating the hydrological model together with the rating curve used to reconstruct the discharge data. This fundamental step also helps us narrow down the uncertainty range for the parameterization of the rating curve in a more justified way. In turn, this step paves the way to a more reliable calibration of VIC-Res.

Looking at the specific results of the sensitivity analysis, there are two important points worth stressing here. First, we show that simultaneously estimating the parameters of the hydrological model and the Manning's coefficient (by optimizing a set of model performance metrics) may significantly bias the reconstruction of the discharge values. This implies that different combinations of performance metrics can result in different estimations of river discharge, thereby influencing the parameterization of the hydrological model. We saw, for example, that focusing on NSE erroneously biases the model towards high flows. In turn, this could bias the results of hydrological modelling applications, such as discharge forecasts or climate change impact assessments. Second, the sensitivity analysis specifically focused on the nine parameters of VIC-Res shows

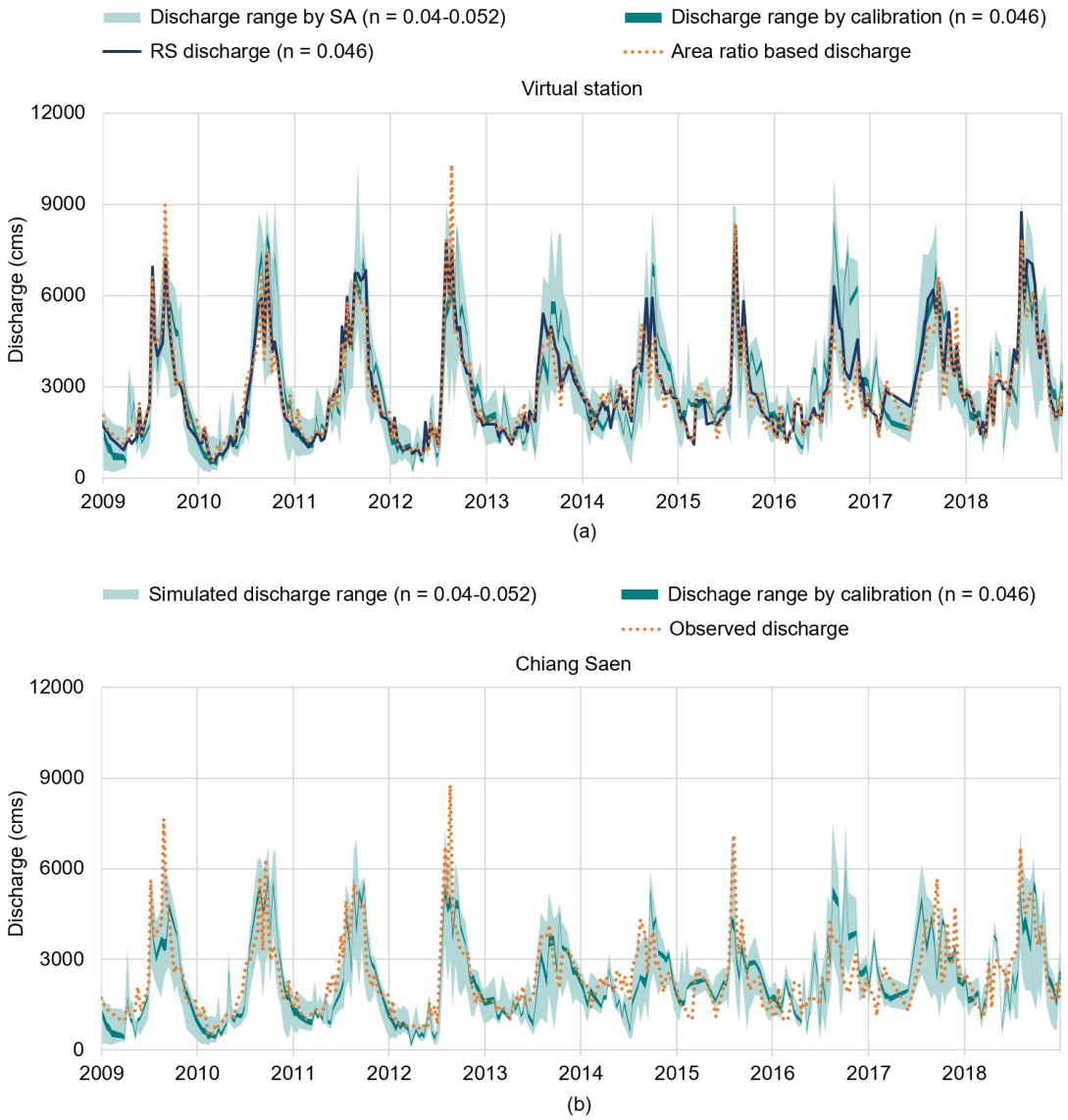

FIGURE 3.9: Performance of model calibration at the virtual station (a) and model validation at Chiang Saen station (b). The dark green band is the variation range of simulated discharge corresponding to the twelve selected solutions in calibration, while the light green band is the one corresponding to the 40 selected solutions from the sensitivity analysis. The dark blue line is the remote-sensed discharge at the virtual station with n = 0.046. In panel a, the dotted orange line is the discharge at the virtual station scaled from the observed discharge at Chiang Saen. In panel b, the line corresponds to the observed discharge at Chiang Saen.

the existence of equifinality, meaning that different parameterizations can yield similar performance in terms of NSE, TRMSE, MSDE, and ROCE. This equifinality issue is arguably explained by the fact that we are using only river discharge data to inform

the parameterization of both the rainfall-runoff and discharge routing modules. Previous research has systematically shown that a small number of parameters typically dominates the variability of a given model output (though which parameters that are dominant might vary with the chosen metric) (Wagener and Pianosi, 2019; Yeste et al., 2020). One may therefore expect that observations of other hydrological processes, such as evapotranspiration, could help reduce the uncertainty in the model parameters.

Our numerical framework seeks to reduce the pitfalls hidden in model calibration, but, like any other modelling study, is potentially affected by various uncertainties. First, because of the unavailability of gauged rainfall data, we use a gridded product—a common approach for macro-scale studies. Yet, gridded rainfall data inevitably carry uncertainties, especially in regions, like Southeast Asia, where the number of rainfall gauges is limited (Funk et al., 2015; Kabir, Pokhrel, and Felfelani, 2022). Another source of uncertainty is the estimation of the river discharge, which is here based on river cross-section, rating curve, and altimetry data. Our results show that the estimation is reliable, but one cannot deny that the spatial resolution of the DEM, the interpolation of the cross-section below the lowest water level, or the use of altrimetry do not contribute to modelling uncertainty. Still in this regard, we should also remind that approaches based on the relationship between discharge, water levels, and cross-sections work best on river stretches that are not affected by levees or other interventions. In this regard, a potential game changer is the Surface Water and Ocean Topography (SWOT) NASA satellite mission, recently launched in December 2022. SWOT will provide river width, water level, and water surface slope for major rivers with an average revisit time of 11 days for the next three years (JPL, n.d.). This means we will be able to leverage existing algorithms to estimate river discharge (Colin J. Gleason and Smith, 2014; M. Durand et al., 2016; Hagemann, C. J. Gleason, and M. T. Durand, 2017) and then inform the implementation of macro-scale hydrological model—an area certainly worth additional research. Yet, we should not forget that model calibration requires time series longer than three years. We could therefore envisage a future in which calibration exercises assimilate multiple discharge data inferred from multiple satellite data.

Looking forward, we should consider expanding frameworks like the one presented here to even more complex modelling environments. One often recurring in downstream applications is the presence of multiple human interventions, such as dams, irrigation withdrawals, and groundwater pumping. Understanding how data concerning the representation of all these processes influences model calibration remains an open question. A similar comment applies to the calibration of multi-basin and global models. Bringing all these elements together would be a major step towards a more reliable calibration of macro-scale hydrological models.

Chapter 4

Optimizing the filling strategy of cascade reservoir systems: A retrospective analysis of the Lancang dams

4.1 Introduction

The water impoundment and operations of large reservoirs often cause socioeconomic and environmental impacts, such as downstream flow alterations that affect ecosystem services and biodiversity (Winemiller et al., 2016). It is even more critical for the cascade reservoir systems located in large transboundary river basins, where riparian countries have different views on how the reservoirs should be filled and operated. In general, the upstream country (reservoir owner) usually tries to maximize the benefits of the reservoir (e.g., hydropower production), while the downstream countries would like to minimize the impacts on their habitat. For the reservoir filling period, ideally, the upstream country wants to apply a fast water impoundment to quickly generate hydropower. Conversely, the downstream countries may prefer a gradual filling strategy that causes minimal impacts (Zaniolo et al., 2021). This conflict presents a challenge in designing the reservoir filling strategy.

Over the past several decades, plenty of efforts have been focused on studying reservoir operating rule (Sale, Jr., and Herricks, 1982; M. S. Hossain and El-shafie, 2013; Galelli et al., 2022). Unfortunately, the reservoir filling stage has been receiving less attention than the operational stage in research activities (Y. Zhang, Erkyihum, and Block, 2016). There is indeed a limited number of studies on how reservoirs should be filled and the impacts of the filling strategy. In those studies, a limited number of alternative reservoir filling strategies were explored, and those strategies were created by using one of three methods. The first method is the modification of the historical filling strategy. For example, Zaniolo et al. (2021) classified the years in their study period into three classes (dry, normal, and wet), then use three variable scaling factors associated with the three classes to modify the historical filling strategy. The second method is based on the inflow to the reservoir. More specifically, a percentage of inflow to the reservoir (e.g., 10%, 20%) is assigned to each month or year during the filling period (Mulat and Moges, 2014; Madson and Shen, 2020). The last method does not require a historical filling strategy or information on inflow to the reservoir. It simply defines the filling duration (e.g., 3 years, 5 years) and the percentage of reservoir storage volume

that will be filled for each month or year in the filling duration (Y. Zhang, Erkyihum, and Block, 2016). A gap we can see here is that either the previous approaches rely on the historical filling strategy, which makes them not applicable to planned dams or they may miss out on potential alternative reservoir filling strategies because only a limited number of alternative filling strategies are created by simply defining a percentage of reservoir storage volume or inflow to the reservoir for each time step in the filling period.

In this work, we introduce a novel simulation-optimization approach for optimizing the filling strategy for reservoir systems. To create alternative reservoir filling strategies, we develop a new method (which does not depend on the historical filling strategy) by parameterizing the filling strategy. By changing the parameters in their feasible ranges with the support of an optimization algorithm, we can explore a large number of potential strategies. By applying our approach to the Lancang dam system, we then try to answer three questions: (1) What are the optimal filling strategies for the system? (2) How good/balanced is the historical filling strategy? (3) Are there more balanced filling strategies, and, if yes, how much upstream and downstream countries would have gained and lost if such strategies were used instead of the actual strategy?

4.2 Study area

4.2.1 The Lancang-Mekong River Basin

The Lancang-Mekong River Basin is the largest transboundary river in Southeast Asia, with a total drainage area of $\sim$ 795,000 km^2 (small box in the panel (a) of Figure 4.1). The river, which is $\sim$ 4,350 km long, originates from Tibetan Plateau in Southwest China and flows through Myanmar, Laos, Thailand, Cambodia, and Vietnam, where it drains into the Vietnam East Sea. Its upper portion—the Lancang—occupies almost half of the river length and around a quarter of the catchment area. The Lancang Basin is characterized by a complex topography, with high mountains and low valleys. Located in the monsoonal climate region, the basin receives a large amount of precipitation every year, 750 to 1025 mm across the basin. However, most of the precipitation (70-80%) arrives during the wet season (June to November) (Yun et al., 2020). The Lancang contributes about 80 km^3 of water, accounting for approximately 16 % of the average annual discharge of the entire Mekong (MRC, 2009).

4.2.2 The cascade dam system

The topographic and climatic characteristics of the Lancang Basin have turned it into a hotspot for hydropower development. Over the past three decades, eleven dams have been built and operated on the mainstream of the Lancang (WLE Mekong, n.d.). Figure 4.1a demonstrates the location of each dam in the cascade dam system, while Figure 4.1b shows the total storage volume and the commission time of each dam. The information is retrieved from Do et al. (2020). This cascade dam system has a total capacity of $\sim$ 42,000 MCM, which can control up to 55 % of the average downstream annual discharge, i.e., at Chiang Sean station in Northern Thailand (see the location in Figure 4.1a). Among these eleven dams, Xiaowan and Nouzhau are the two largest dams, which account for $\sim$ 85 % of the total storage of the system. Because of their size, they

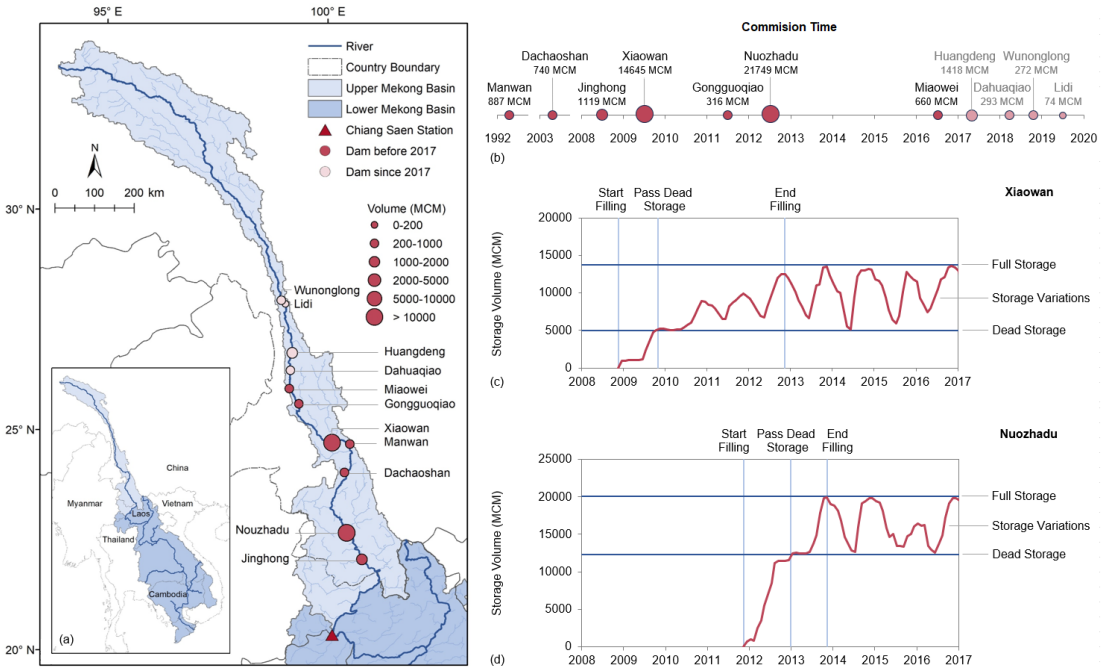

FIGURE 4.1: The Lancang River Basin—the upper portion of the Mekong River Basin (a), the total storage volume and commission time of the dams in the Lancang River (b), and the actual filling strategy of Xiaowan (c) and Nouzhadu (d) reservoirs inferred from satellite data (Chapter 2).

play the role of system 'drivers', gradually storing water until reaching their maximum operational level in the wet season and releasing water to the downstream reservoirs in the dry season to ensure that the other reservoirs can run at their normal operational level. Therefore, the other reservoirs have very limited storage variations (IRN, 2014).

4.2.3 Historical filling strategies

In panels (c) and (d) of Figure 4.1, we show the filling strategy of Xiaowan and Nuozhadu reservoirs inferred from satellite data (Chapter 2). As shown in the figure, Xiaowan was filled in four years, from December 2008 to November 2012, passing its dead storage after around one year of impoundment. Meanwhile, Nuozhadu was filled in only two years, from December 2011 to November 2013, also passing its dead storage after around one year of impoundment. Note that the filling strategies retrieved from satellite data are matching with the filling timeline mentioned in Hua, Ke, and Dai (2018) and Lv and Chi (2018) for Xiaowan and Nuozhadu, respectively. Other reservoirs have a relatively small storage capacity compared to Xiaowan and Nuozhadu, varying from 74 MCM (Lidi) to 1418 MCM (Huangdeng); so they were filled in just a few months (see Figure C.1).

By focusing on the filling strategies of Xiaowan and Nuozhadu, we choose our study period to go from 2008 to 2016. This period allows us to test the filling strategies with a duration of maximum five years for each reservoir (see the explanation in Section 4.3.2).

The reason for such a constraint in our study period is that the other reservoirs are relatively small compared to Xiaowan and Nuozhadu; so, the storage variations of the entire system before and after their filling period seem to be stationary. If we include the stationary stages, when calculating the average annual indicators for assessing the impacts of the filling strategies (see Section 4.3.3), we will hardly see the differences of the indicators with different filling strategies. For the other reservoirs in the system, we use their actual filling strategy and operations inferred from satellite data (Chapter 2).

4.3 Methodology

In this work, we develop a simulation-optimization approach, which includes a hydrological model—VIC-Res—and a multi-objective evolutionary algorithm—ϵ-NSGA-II (Figure 4.2). VIC-Res model, described in Section 4.3.1, simulates the water level of reservoirs, release from reservoirs, and downstream discharge (at Chiang Saen). We simulate these processes using alternative reservoir filling strategies, and each of the strategies is determined by a set of parameters—referred to as filling strategy parameters here-after (see Section 4.3.2). VIC-Res output is used to calculate three objective functions (see Section 4.3.3), which ϵ-NSGA-II uses to evaluate and adjust the filling strategy parameters. This process (the blue loop in Figure 4.2) is repeated a predefined number of times (see Section 4.3.3), and the optimal solutions are identified from all explored solutions. To calculate the average monthly deviation of the downstream flow from its natural flow (MD), we also use the natural downstream discharge (at Chiang Saen). We estimate this data by running VIC-Res with the no-dam scenario (i.e., the reservoir operation module in VIC-Res is switched off). We also run VIC-Res with the actual reservoir filling strategy obtained from satellite data (the output of Chapter 2) and calculate the corresponding objective functions (the pink arrows in Figure 4.2). Finally, we evaluate the performance of the actual reservoir filling strategy (also referred to as the baseline) by comparing it with the performance of the optimal solutions.

4.3.1 Hydrological Model

In this study, we use a large-scale semi-distributed hydrological model—VIC-Res (Dang, Chowdhury, and Galelli, 2020; Dang, Vu, et al., 2020), a novel variant of VIC (Liang et al., 2014). VIC-Res includes 2 modules, namely rainfall-runoff and routing. The first module calculates the base-flow and runoff for each pixel in the model domain from various inputs, including precipitation, temperature, wind speed, land cover, albedo, and Leaf Area Index. The second module routes the base-flow and runoff, calculated previously, throughout the river network using the method presented in Lohmann, Nolte-Holube, and Raschke (1996) and Lohmann, Raschke, et al. (1998). In the routing module of VIC-Res, an explicit representation of reservoir operations is integrated. The option of using pre-determined time-series of reservoir storage volume allows us to capture the effect of reservoirs not only in operational period but filling period also. The model calculates the reservoir release from the input of storage volume, simulated inflow to reservoir and evaporation by using the mass balance method. Our VIC-Res model in the Lancang River Basin was calibrated previously in Dang, Chowdhury, and Galelli (2020), and its reliability was improved by another calibration exercise (for 7 soil parameters and 2 routing parameters) with an additional source of stream flow data—archived from satellite observations (see more details in Chapter 3). Input data for

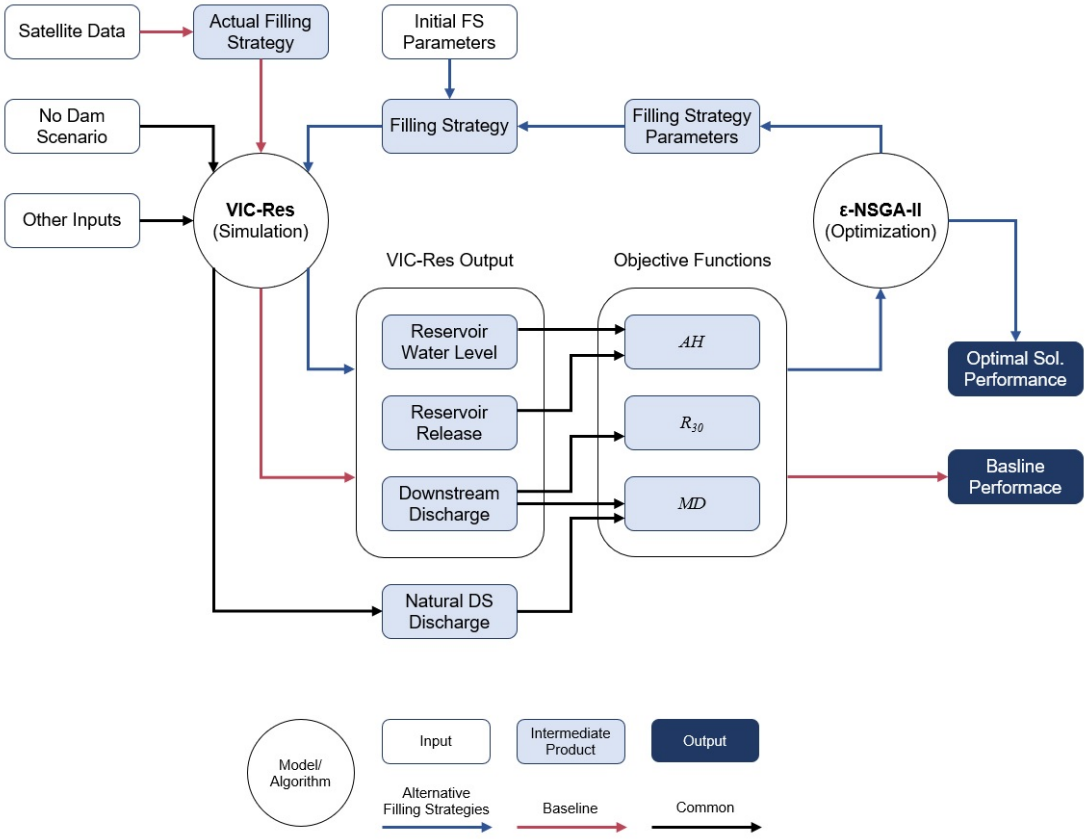

FIGURE 4.2: Flowchart illustrating the adopted simulation-optimization approach, which includes a hydrological model (VIC-Res) and a multi-objective evolutionary algorithm (ϵ-NSGA-II). VIC-Res model simulates the water level of reservoirs, release from reservoirs, and downstream discharge using alternative reservoir filling strategies. Each of the filling strategies is determined by a set of filling strategy (FS) parameters. The VIC-Res output is used to calculate three objective functions, which ϵ-NSGA-II uses to evaluate and adjust the filling strategy parameters. This process (the blue loop) is repeated a predefined number of times, and the optimal solutions are identified from all explored solutions. The natural downstream (DS) discharge, used for calculating the average monthly deviation of the downstream flow from its natural flow (MD), is simulated by the VIC-Res model with the no-dam scenario. The performance of the actual reservoir filling strategy (inferred from satellite data) is obtained following the pink arrows, then evaluated by comparing it with the performance of the optimal solutions.

VIC-Res including climate forcing data, land use and cover, albedo, Leaf Area Index, and flow direction can be found in Section 3.3.1.

4.3.2 Alternative reservoir filling strategies

Notations and assumptions

To model our reservoir filling strategies, we use the following notations:

T_F - Filling duration or time to reach full storage of reservoir (unit: year);
S_D - Dead storage volume of reservoir (unit: MCM), S_D = 5096 and 12500 MCM for Xiaowan and Nuozhadu respectively;
S_F - Full storage volume of reservoir (unit: MCM), S_F = 13725 and 20077 MCM for Xiaowan and and Nuozhadu respectively;
S_{Wt} - Storage voulume of reservoir at the end of the wet season (November) of year t (unit: MCM), $t = 1, 2, ..., T_F$;
S_{Dt} - Storage volume of reservoir at the end of dry season (May) of year t (unit: MCM), $t = 1, 2, ..., T_F$.

To make our reservoir filling strategies practical and also to avoid a high computational cost (due to introducing too many parameters and calculation cases), the following assumptions are made:

(1) The starting time of the filling strategies in our experiment follows the actual starting time, i.e., December 2008 and December 2011 for Xiaowan and Nuozadu, respectively. We do not move the starting time forward because the construction of reservoirs may not be completed yet. We do not move the starting time backward neither, since it delays the commission time of reservoirs. Besides, our filling strategies finish at the end of wet seasons (November), also based on the actual operations of Xiaowan and Nuozadu. These reservoirs store water in the wet seasons until November (reaching the peak values of storage volume in November) and release water thereafter. Therefore, the filling duration T_F is an integer number, e.g., 3 years or 4 years, with each year starting from December (of the previous year) to November (of that year).

(2) The impoundment of each reservoir can be completed in one wet season (June to November). This is possible because the total inflow to each reservoir in a wet season is larger than the total storage volume of that reservoir. Particularly, The total inflow to Xiaowan in the wet season of each year (from 2009 to 2013) varies from 23500 to 28800 MCM (note that the inflow is simulated by VIC-Res and there was no reservoir in the upstream of Xiaowan in this period). Meanwhile, the total inflow to Nuozhadu in the wet season of each year (from 2012 to 2016) varies from 24900 to 37200 MCM (with the actual operation of Xiaowan in the upstream of Nuozhadu) and from 22600 to 33700 MCM (if Xiaowan is fully operated). However, to avoid designing aggressive filling strategies, we set the minimum filling duration of each reservoir at 2 years. On the other hand, the maximum filling duration of each reservoir is 5 years, which is longer than the actual filling duration of Xiaowan and Nuozhadu. The selection of 5 years (till 2013 and 2016 for Xiaowan and Nuozhadu, respectively) is also suitable with the fact that from the end of 2016, at least one new dam in the Lancang River is filled. Therefore, $T_F = 2, 3, 4, 5$.

(3) The storage volume of reservoirs at the end of the first month (December 2008 and December 2011 for Xiaowan and Nuozadu respectively), S_{W0}, is set to 1000 MCM,

which is approximately the actual values.

(4) To ensure progress of the reservoir filling, the storage volume at the end of wet season of each year in filling period should be higher than the one of the previous year, $S_{Wt} \geq S_{W(t-1)}$.

(5) Before passing dead storage, during the dry seasons, reservoirs either store more water or keep the same storage volume. This means that the storage volume at the end of the dry season of each year is higher than or equal to the one at the end of the previous wet season, i.e., $S_{Dt} \geq S_{W(t-1)}$.

(6) After passing dead storage, there is no storing of water in dry seasons. In most cases, storage volume is kept the same in dry seasons until the end of filling period. However, Xiaowan, in fact, released water in dry seasons to quickly produce hydropower. Therefore, the storage volume at the end of dry season of each year is less than or equal to the one at the end of the previous wet season, i.e., $S_{Dt} \leq S_{W(t-1)}$.

(7) After the filling period (reaching the full storage), the reservoir storage volume follows the actual variations estimated from satellite data.

(8) The impoundment of each month in a dry/wet season follows a distribution based on the average monthly inflow to reservoir simulated by VIC-Res within the study period. Note that there is no difference in the inflow to Xiaowan under different scenarios because there is no reservoir upstream, and no significant difference in the inflow to Nuozhadu under different scenarios because, in 2012-2013, Xiaowan (in the upstream of Nuozhadu) almost reached its stationary storage variation with all scenarios.

Standard reservoir filling strategies

To produce the alternative reservoir filling strategies, we first construct our standard reservoir filling strategies, which are modified later to create other alternative reservoir filling strategies. As illustrated in Figure 4.3a, our standard reservoir filling strategies are created simply by distributing an equal portion of the total reservoir storage volume (= S_F/T_F) to the impoundment of each year in the filling period. For example, in the case of 4-year filling period ($T_F = 4$), the reservoir is filled 25% of its total volume in each year. The storage volume at the end of each year (wet season) are S_{W1} = 25% S_F, S_{W2} = 50% S_F, S_{W3} = 75% S_F, and S_{W4} = 100% S_F. In the standard reservoir filling strategies, the impoundment is carried out in the wet seasons only, and storage volume is kept the same throughout the dry seasons (S_{Dt} = $S_{W(t-1)}$). After the filling period (T_F), S_{Dt} and S_{Wt} follow the actual storage variations—baseline—inferred from satellite data.

Variants of the standard reservoir filling strategies

We create the variants of the standard reservoir filling strategies by changing the values of S_{Dt} and S_{Wt} within their ranges. Specifically, the storage volume at the end of wet seasons, S_{Wt}, varies from $S_{Wt(standard)} - 1/2 \cdot S_F/T_F$ to $S_{Wt(standard)} + 1/2 \cdot S_F/T_F$ (see Assumption 4). Before passing the dead storage, the storage volume at the end of

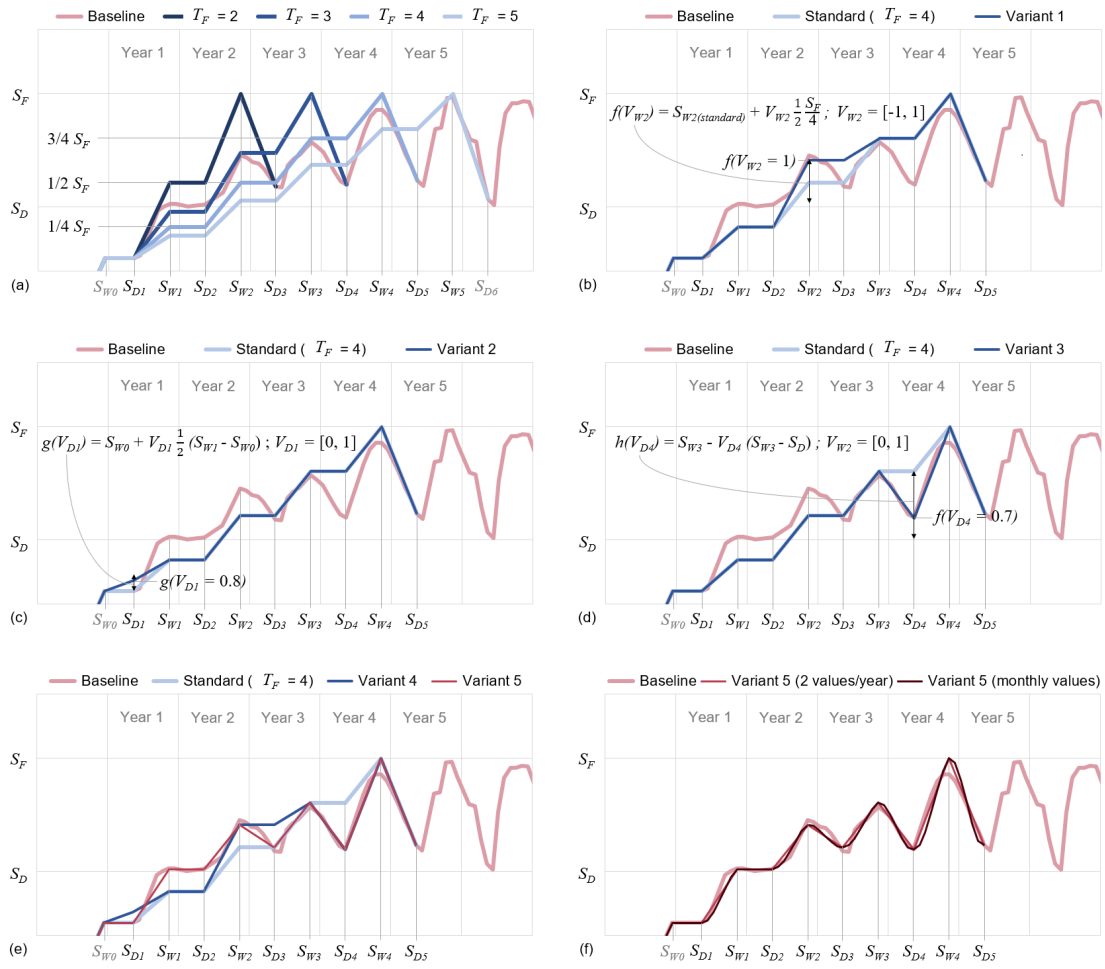

FIGURE 4.3: Reservoir filling strategy parameterization. Standard reservoir filling strategies with filling duration, T_F = 2, 3, 4, 5 years (a). Examples of creating variants of the standard reservoir filling strategy (T_F = 4) by modifying S_{Wt}—a function of parameter V_{Wt} (b), and S_{Dt}—a function of parameter V_{Dt} with two cases, before (c) and after (d) passing dead storage. Panel (e) shows 2 alternative reservoir filling strategies with Variant 5 as a reconstruction of the baseline. Panel (f) shows Variant 5 in two formats, 2 values/year and monthly values. The monthly time-series is created using the monthly impoundment distributions.

dry seasons, S_{Dt}, varies from $S_{W(t-1)}$ to $S_{W(t-1)} + 1/2(S_{Wt} - S_{W(t-1)})$ (Assumption 5); and after passing dead storage, S_{Dt} varies from S_D to $S_{W(t-1)}$ (Assumption 6). To have different variations of S_{Dt} and S_{Wt}, we introduce the following parameters:

V_{Wt} - Parameter of the storage volume at the end of wet season of year t (unitless), $V_{Wt} \in [-1, 1]$, $t = 1, 2, 3, 4, 5$;
V_{Dt} - Parameter of the storage volume at the end of dry season of year t (unitless), $V_{Dt} \in [0, 1]$, $t = 1, 2, 3, 4, 5$.

Then, the storage volume at the end of wet seasons, S_{Wt}, is identified using Equation

4.1. Meanwhile, the storage volume at the end of the dry seasons, S_{Wt}, is identified using Equation 4.2 (before passing dead storage) and Equation 4.3 (after passing dead storage). For example, illustrated in Figure 4.3b, S_{W2} in the case of 4-year filling period varies from $S_{W2(standard)} - 1/2 \cdot S_F/4$ (when $V_{W2} = -1$) to $S_{W2(standard)} + 1/2 \cdot S_F/4$ (when $V_{W2} = 1$). We create a variant by choosing $V_{W2} = 1$ while keeping other S_{Wt} and S_{Dt} the same ($V_{Wt} = 0, t \neq 2$ and $V_{Dt} = 0$). In Figure 4.3c, we show the variation range of S_{D0} (before passing dead storage), which is from S_{W0} (when $V_{D1} = 0$) to $S_{W0} + 1/2(S_{W1} - S_{W0})$ (when $V_{D1} = 1$). We create a variant by choosing $V_{D1} = 0.8$ while keeping other S_{Wt} and S_{Dt} the same ($V_{Wt} = 0$ and $V_{Dt} = 0, t \neq 1$). In Figure 4.3d, we show the variation range of S_{D4} (after passing dead storage), which is from S_D (when $V_{D4} = 1$) to S_{W3} (when $V_{D4} = 0$). We create a variant by choosing $V_{D4} = 0.7$ while keeping other S_{Wt} and S_{Dt} the same ($V_{Wt} = 0$ and $V_{Dt} = 0, t \neq 4$).

$$f(V_{Wt}) = t\frac{S_F}{T_F} + V_{Wt}\frac{1}{2}\frac{S_F}{T_F} \tag{4.1}$$

$$g(V_{Dt}) = S_{W(t-1)} + V_{Dt}\frac{1}{2}(S_{Wt} - S_{W(t-1)}) \tag{4.2}$$

$$h(V_{Dt}) = S_{W(t-1)} - V_{Dt}(S_{W(t-1)} - S_D) \tag{4.3}$$

In Figure 4.3e, we show 2 examples of alternative reservoir filling strategies, which are modified from a standard reservoir filling strategy ($T_F = 4$). Variant 5 is an example that is similar to the baseline of Xiaowan. In other words, our reservoir filling strategy parameterization is able to reconstruct the actual filling strategies. Finally, in Figure 4.3f, we show the Variant 5 with 2 formats, 2 values/year and monthly values. The second one is created by using the monthly impoundment distributions mentioned in Assumption 8. We interpolate the monthly time-series data to a daily time-series data, that we use as the input of the reservoir operation module in VIC-Res.

4.3.3 Optimizing reservoir filling strategy

Decision variables

The decision variables in our optimization exercises are V_{Wt} and V_{Dt} (see Section 4.3.2), which determine our alternative filling strategies. Since we are testing our approach on 2 reservoirs (Xiaowan and Nuozhadu), and the maximum filling duration is 5 years, the total number of decision variables is 20.

Objective functions

The objective functions are selected to capture the effects of the filling strategies of the Lancang reservoirs system. Our objective functions, adapted from Galelli et al. (2022), include benefits for upstream, represented by an indicator of hydropower production (AH), and impacts downstream represented by two indicators of downstream flow modification by the dam system (R_{30} and MD). The three objective functions are defined below:

(1) AH - Average annual hydropower production of the dam system (unit: TWh/year), which is to be maximized.

$$AH = \frac{1}{Y}\sum_{y=0}^{Y}\sum_{d=1}^{D_y}\sum_{n=1}^{N} P_{ydn} \tag{4.4}$$

where P_{ydn} is the hydropower production of dam number n, on day d, year y. N is the number of dams in the system. D_y is the number of days in year y, and Y is the number of years considered in this study (i.e., 8 years, from 2009 to 2016).

(2) R_{30} - Average annual ratio between 30-day maximum and 30-day minimum flows to downstream—calculated with discharge at Chiang Saen station—(unitless), which is to be maximized.

$$R_{30} = \frac{1}{Y}\sum_{y=0}^{Y}\frac{Q_y^{30,max}}{Q_y^{30,min}} \tag{4.5}$$

where $Q_y^{30,max}$ and $Q_y^{30,min}$ are the 30-day maximum and minimum flows at Chiang Saen station of year y. R_{30} is an indicator that reflects the shape of the hydrograph. A high value of R_{30} means that annual stream flow has a strong seasonal hydrological regime. R_{30} of the natural stream flow at Chiang Sean (simulated by VIC-Res under the no-dam scenario) is approximately 11.758. The Lancang dams tend to decrease R_{30} at Chiang Saen since they decrease flood season flow and increase dry season flow.

(3) MD - Average monthly deviation of the flow to downstream from its natural flow—calculated with discharge at Chiang Saen station—(unitless), which is to be minimized.

$$MD = \frac{1}{M}\sum_{m=1}^{M}\frac{|Q_m^{sim} - Q_m^{nat}|}{Q_m^{nat}} \tag{4.6}$$

where Q_m^{sim} is the discharge of month m at Chiang Saen station simulated by VIC-Res with reservoir filling strategies, while Q_m^{nat} is the natural discharge of month m at Chiang Saen station simulated by the VIC-Res model with its reservoir operation module switched off (no-dam scenario). M is the number of months considered in this study (i.e., 96 months, from January 2009 to December 2016). The reason for maximizing R_{30} and minimizing MD is to decrease the alteration level of the downstream flow regime, which drives key ecosystem services and and biodiversity.

Experimental setup

For our optimization exercise, we employ a multi-objective evolutionary algorithm—ε-NSGA-II. We set the initial population size equal to 20, the number of function evaluations equal to 500, and ε equal to 0.001. We normalize all performance metrics between 0 and 1. The optimization exercise is carried out independently for different cases of T_F. There are a total of 16 cases (4 T_F values of Xiaowan x 4 T_F values of Nuozhadu). The best (Pareto-efficient) solutions are selected across the 16 optimization exercises. The experiment is run on an Intel (R) Xeon (R) W-2175 CPU 2.50 GHz with 128 GB RAM running Linux Ubuntu 18.04 with a total running time of about 84 hours.

4.4 Results

4.4.1 Trade-offs between objective functions

After running our experiment, we receive a total of 280 members in the Pareto front (non-dominated solutions). To visualize the trade-offs between objective functions, we produce the scatter plots (Figure 4.4). Overall, the plots confirm the trade-offs between the benefits and impacts created by filling in the reservoirs. In particular, in panel (a), we can easily notice a strong correlation between the average annual hydropower production (AH, to be maximized) and the average monthly deviation of the downstream flow (i.e., at Chiang Saen) from the natural flow (MD, to be minimized): the more hydropower is produced during the filling period, the more the downstream flow is altered, and vice versa. Panel (b) shows a relatively strong correlation between the average annual hydropower production and the average annual ratio between the 30-day maximum and 30-day minimum flows at Chiang Saen (R_{30}, to be maximized). At the same level of MD, the higher AH is, the lower R_{30} is. On the other hand, in panel (c), we hardly see a correlation between the two objective functions which capture the impacts of reservoirs on the downstream flow (R_{30} and MD). Finally, in panel (d), we provide a 3D scatter plot using all three objective functions. The 3D visualization agrees with the insight found in panels (a), (b), and (c).

Interestingly, the actual filling strategy of Xiaowan and Nuozhadu (also referred to as the baseline, represented by pink color in Figure 4.4) is not dominated by the Pareto members. Yet, we note that our filling strategy parameterization is not able to create the exact same strategy as the baseline. It is because we create the monthly time series from the storage values at the end of wet and dry seasons using our monthly impoundment distribution (see Section 4.3.2), meanwhile the baselines did not follow that distribution. Furthermore, compared to the values of the objective functions of the Pareto members, the baseline has a high value of AH, a low value of R_{30}, and a high value of MD. This means that the actual filling strategy of Xiaowan and Nuozhadu was applied to prioritize hydropower production. We provide more insights into this aspect in the next section.

4.4.2 Evaluation of the filling strategies

In this subsection, we compare the values of each objective function (AH, R_{30}, and MD in panels (a), (b), and (c) of Figure 4.5 respectively) corresponding to each Pareto solution groups (light blue), all solutions (dark blue), and the baseline (pink). The Pareto solutions are grouped by the filling durations (T_F) of the two reservoirs, and the number of solutions in each group is shown in Figure 4.5 (in the parentheses under group name). For example, Group X4-N2 includes 25 solutions, which are a 4-year filling strategy for Xiaowan and a 2-year filling strategy for Nuozhadu.

The first three groups (X2-N2, X2-N3, and X3-N2) are the most 'aggressive' groups regarding the time to fill, with at least one reservoir filled in 2 years and at most one reservoir filled in three years. These groups have high AH values, but low R_{30} values and high MD values. These groups are favorable for the upstream country (China). Also considered favorable for upstream, Group X4-N2 has high AH values and high MD values, however, its R_{30} values vary in a higher and broader range. By extending

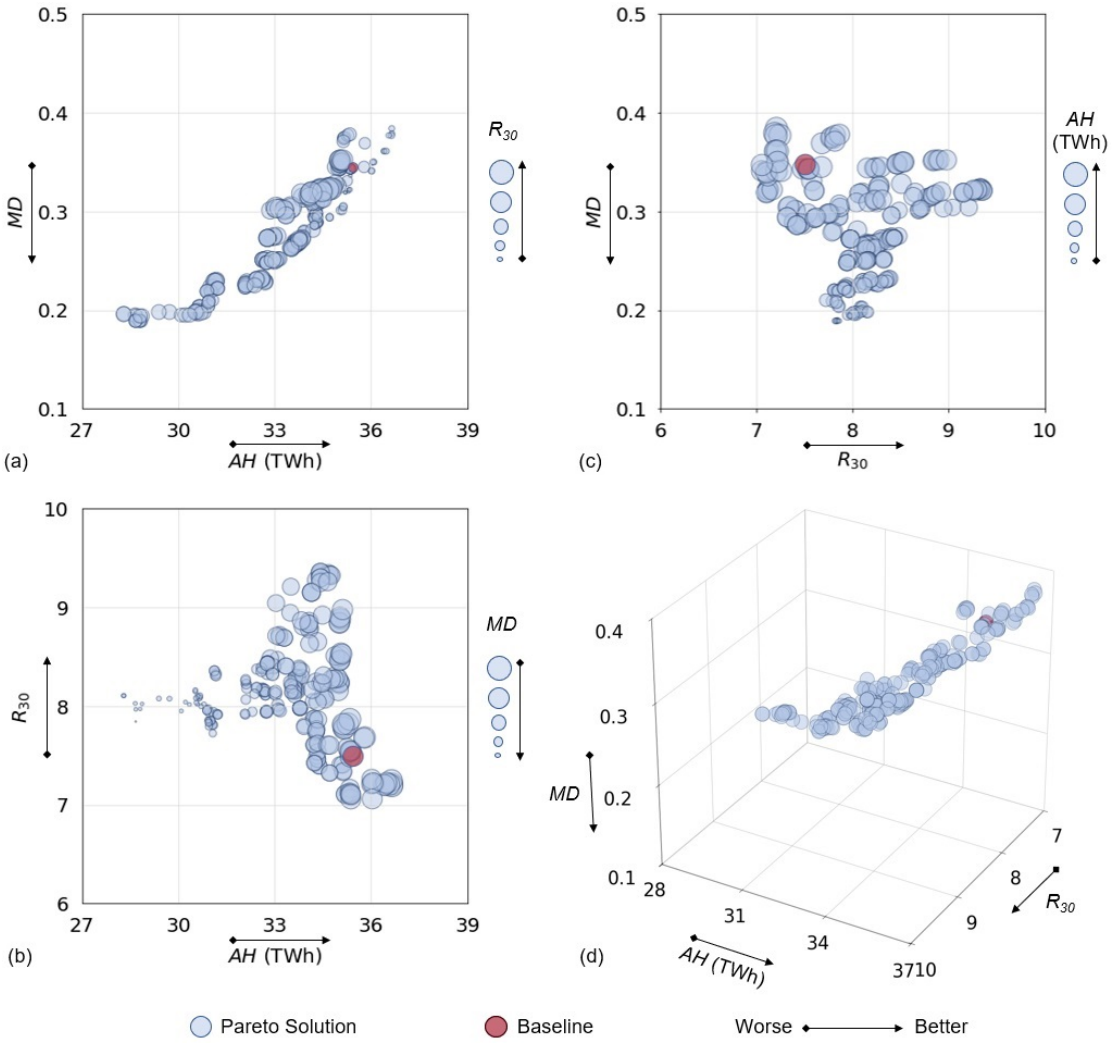

FIGURE 4.4: Pareto front and the correlations between the objective functions. Panel (a) reveals a strong correlation between the average annual hydropower production (AH, to be maximized) and the average monthly deviation of the downstream flow (i.e., at Chiang Saen) from its natural flow (MD, to be minimized). Panel (b) shows a relatively strong correlation between AH and the average annual ratio between the 30-day maximum and 30-day minimum flows at Chiang Saen (R_{30}, to be maximized). In panel (c), the correlation between R_{30} and MD is hardly seen. Panel (d) is a 3D scatter plot using all three objective functions. The actual filling strategy of Xiaowan and Nuozhadu (the baseline, represented by pink color) behaves like a Pareto member, which was applied to prioritize hydropower production.

one more year in the filling duration of either Nuozhadu (X4-N3) or Xiaowan (X5-N2), we can lower down MD values and increase R_{30} values (some strategies in Group X5-N2 even have the highest values of R_{30}), which are more favorable for downstream. Nevertheless, by doing so, we also decrease AH (although some strategies in Group

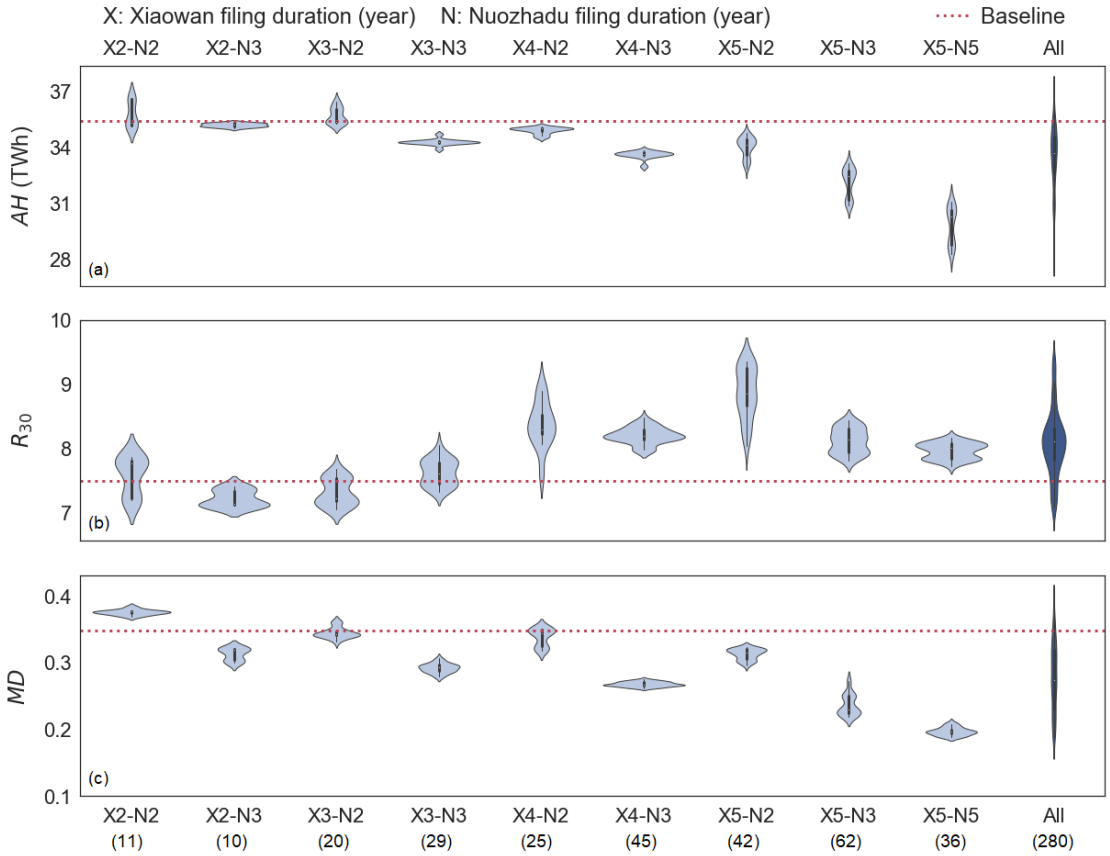

FIGURE 4.5: Comparison of the values of each objective function (AH, R_{30}, and MD in panels (a), (b), and (c) respectively) corresponding each Pareto solution groups (light blue), all solutions (dark blue), and the baseline (pink).

X5-N2 still can maintain high values of AH). Group X3-N3 has a quite similar performance to Group X4-N3, but relatively lower R_{30} values. Lastly, the two last groups (N5-X3 and N5-X4) have low MD values, but also low AH values. R_{30} values of these groups are higher than the ones of the most 'aggressive' groups, but not the highest. These groups are considered favorable for the downstream.

Recall that the baseline follows the durations of Group X4-N2: Represented by the pink dotted lines in Figure 4.5, the performance of the baseline shows that the actual filling strategy of Xiaowan and Nouzhadu is favorable for upstream with a high value of AH (35.430 TWh/year), a low value of R_{30} (7.501), and a high value of MD (0.348).

4.4.3 Pros and cons of more balanced strategies

Based on our analysis in the previous section, we select two groups of more balanced strategies (X4-N3 and X5-N2) for a more detailed analysis to see how much we would have gained and lost if we used such strategies instead of the actual strategy. First, a simple calculation using Equation 4.7 reveals that when changing from the baseline to the filling strategies in Groups X4-N3 and X5-N2, we receive slightly less hydropower,

AH decreases by 4% - 7% and 2% - 7% for X4-N3 and X5-N2, respectively. However, the two remaining indicators are improved significantly, which is beneficial for downstream. To specify, R_{30} increases by 6% - 13% and 7% - 25% for X4-N3 and X5-N2, respectively. Meanwhile, MD reduces 21% - 25% and 7% - 15% for X4-N3 and X5-N2, respectively.

$$FD = \frac{F_{alt} - F_{bl}}{F_{bl}} \cdot 100\% \tag{4.7}$$

where FD is the difference between the objective function values when changing from the baseline to an alternative filling strategy. FD is calculated for each objective function (AH, R_{30}, and MD). F_{alt} and F_{bl} are the objective function values corresponding to the filling strategy and the baseline.

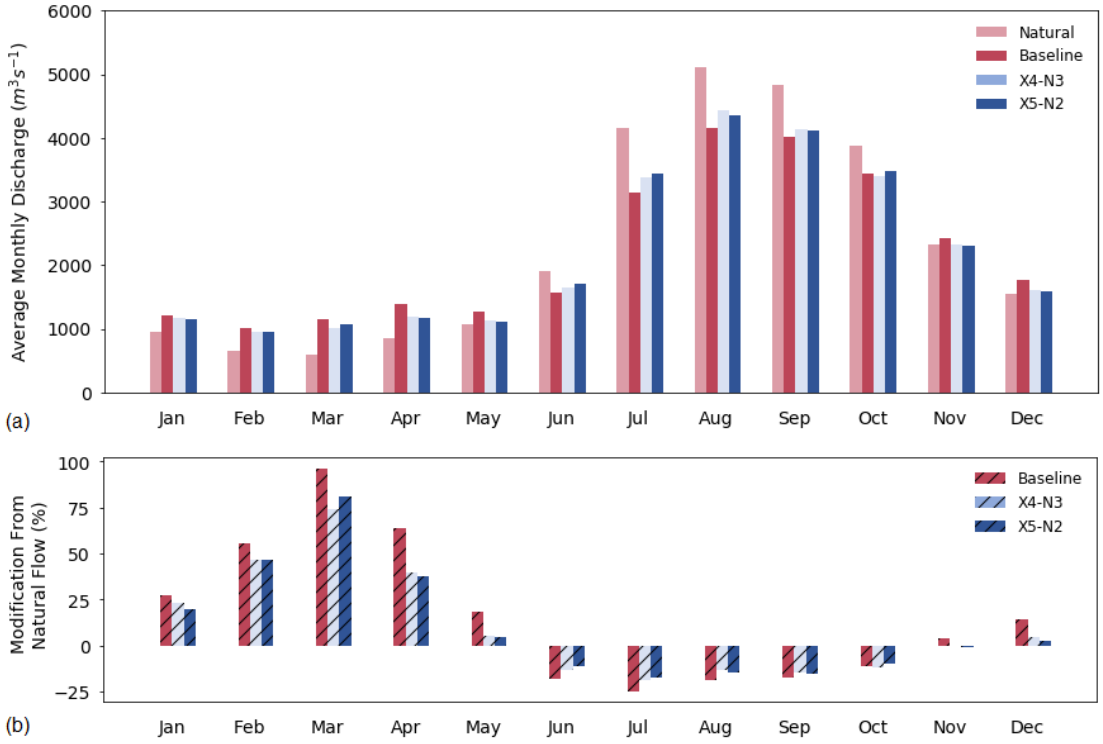

FIGURE 4.6: Average monthly discharge at Chiang Saen (a) and the percentage of modification from the natural flow created by the actual and alternative filling strategies (b). The alternative filling strategies include the non-dominated solutions in Group X4-N3 (light blue) and Group X5-N2 (dark blue) compared against the baseline (dark pink) and the no-dam scenario—natural flow condition (light pink).

In Figure 4.6, we provide a detailed look at downstream flow (i.e., at Chiang Sean station). Particularly, in Panel (a), we compare the average monthly discharge at Chiang Saen with different filling strategies for the dam system. Those strategies include the ones in Group X4-N3 (light blue) and Group X5-N2 (dark blue) compared against the baseline (dark pink) and the no-dam scenario—natural flow condition (light pink). Note that for the two groups of strategies, we use an average value representing all

strategies for each month. The overall point that can be noticed from the figure is that the discharge at Chiang Sean is modified in the same way (increasing the dry season flow and decreasing the wet season flow) but at different levels under the impacts of the different strategies. To see clearly the difference in the levels of flow modification, we calculate and show, in Panel (b), the percentage of flow modification from the natural flow. From the plot, we can see that the strategies of the two selected groups can help to reduce the level of flow modification created by the baseline, especially for the months in the dry season (December to May). For example, in April, the modification levels created by the selected filling strategies is only around half of the one created by the actual strategy.

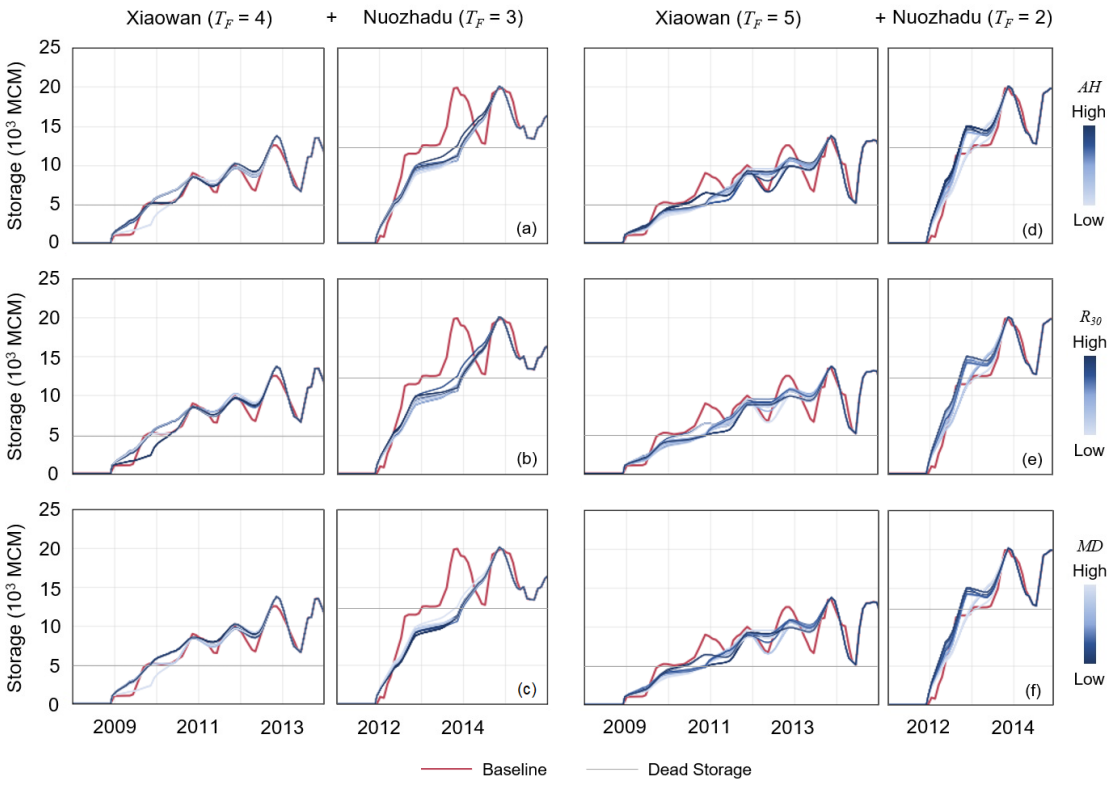

FIGURE 4.7: More balanced strategies—non-dominated solutions in Groups X4-N3 (the left two columns) and X5-N2 (the right two columns). Dark blue lines are the strategies with high AH values (top panels), high R_{30} (middle panels), and low MD (bottom panels). All strategies are compared against the baseline (pink color).

Finally, In Figure 4.7, we plot the filling strategies of two groups (X4-N3 in the left two columns and X5-N2 in the right two columns). For each group, we highlight in dark blue color the strategies with high AH values (top panels), high R_{30} (middle panels), and low MD (bottom panels). All strategies are compared against the baseline (pink color). We notice the time to pass the dead storage of the reservoirs—another aspect that can be used to evaluate the reservoir filling strategies. This factor affects the time when the dams can start generating hydropower. In particular, some strategies in Group (X4-N3) can ensure the time to pass the dead storage of Xiaowan to be the

same as the baseline; yet, the other strategies in this group delay the time to pass dead storage by around 6 months (when trying to prioritize R_30, panel (b)). For Nuozhadu, the time to pass the dead storage is delayed by 10 - 12 months. On the other hand, the X5-N2 strategies delay the time to pass the dead storage of Xiaowan by 5 - 14 months. Interestingly, by extending the filling duration of Xiaowan, we can reduce the water impoundment of Xiaowan in 2012, followed by an increase in the inflow to Nuozhadu downstream. Consequently, the water impoundment of Nuozhadu this year could be increased; and the time to pass the dead storage could be pushed forward by 3 - 4 months. Nevertheless, we are not able to do further analysis on the effects of shifting the time to pass the dead storage because we do not have at hand the official information on the commission time of the dams.

4.5 Discussion and Conclusions

Our study contributes an approach to optimize the filling strategy for cascade reservoir systems. By parameterizing the filling strategy, and changing the parameters in their feasible ranges with the support of an optimization algorithm (ε-NSGA-II), we can explore a large number of alternative filling strategies. Applying our approach to the Lancang dam system, we provided the optimal filling strategies for the system, evaluated the historical filling strategy by comparing it against the optimal solutions, and showed how much upstream and downstream countries would have gained, and lost, if more balanced strategies were used instead of the actual strategy. Our experiment results in 280 optimal filling strategies corresponding to 280 non-dominated solutions on the Pareto front. Interestingly, the actual filling strategy is not dominated by the optimal strategies. Our analysis shows that the actual filling strategy is favorable for upstream with a high value of average annual hydropower production and a high level of downstream flow alteration (i.e., a low value of average annual 30-day maximum and minimum flows ratio and a high value of average monthly flow deviation from natural flow). Lastly, by changing the actual filling strategy to the more balanced filling strategies (which extent the actual filling duration of either Xiaowan or Nuozhadu by one year), the upstream country may expect a slight decrease in hydropower production, however, there are significant improvements in downstream flow alteration.

It is worth noting that there are still a few limitations in our study. First, the outcome of the study is potentially affected by the uncertainties of the hydrological model, which we use to simulate the filling process, inflow, and release of the reservoirs as well as the downstream flow. The uncertainties could come from the rainfall input data or/and model calibration. Second, we use only two parameters for each year in the filling period (at the end of the dry and wet seasons) and convert the half-yearly time series to the monthly time series of storage volume. Doing this way, we may miss out on potential solutions.

Finally, our approach can be applied to other reservoir systems. When applying to the other systems, we may consider other objective functions which work well for the distinctive features of those systems (e.g., the drop in water level of a downstream lake (Zaniolo et al., 2021)). Since our method for creating alternative filling strategies is free from using the historical filling strategy, our approach also can be used for dams under

construction and planned dams. In fact, more dams are currently being constructed and planned to be built in the large transboundary river basins. In the Lancang basin, Tuoba dam, which has a capacity of 1039 Mm^3, is currently under construction. Additionally, ten new dams with a total storage capacity of about 64 950 Mm^3 are planned to join the hydropower fleet of the Lancang (Schmitt et al., 2019). Moving to the downstream, 9 large-scale dams (capacity from $\sim$ 1000 to more than 4000 Mm^3) are slated for the mainstream of the Lower Mekong (Do et al., 2020). Therefore, having tools that can help design more sustainable filling strategies is very important.

Chapter 5

Conclusions

5.1 Summary

In this thesis, we developed a suite of three approaches to address three problems originating from asymmetries in transboundary river basins. The problems include (1) the lack of information on how reservoirs are operated, which causes controversies among riparian countries, (2) the lack of streamflow data for calibrating macro-scale hydrological models in poorly gauged and heavily regulated basins, which characterizes the transboundary river basins, and (3) the need for optimal reservoir filling strategies that can balance the upstream benefits and downstream impacts. Our approaches leverage remote-sensed data, process-based hydrological models, and use of systems analysis (i.e., machine learning, sensitivity analysis, and multi-objective optimization). Besides the methodological contributions, this thesis also contributes to the knowledge of the study site—the Lancang-Mekong River Basin—which well exemplifies the typical issues of transboundary river basins.

In the first problem (Chapter 2), we use a 3-step approach to overcome the challenge of the lack of information on the reservoir operations of the Lancang dam system. First, we estimate the relationship between reservoir water surface area and storage volume (also called the area-storage curve) from the SRTM digital elevation model. Then, we calculate the reservoir water surface area from Landsat satellite images by using our novel water surface area estimation algorithm, which helps remove the effects of clouds, no-data pixels, and other disturbances. Lastly, we infer the time series of reservoir storage volume from the time series of water surface area via the area-storage curve. We leverage satellite altimetry water level data (i.e., Jason and Sentinel-3) to validate our results derived from Landsat images for a couple of reservoirs for which altimetry water level data are available. Our results describe the evolution of the Lancang dam system. We provide the 13-year storage volume time series data of the ten selected reservoirs and highlight the key role of Xiaowan and Nuozhadu reservoirs, which account for approximately 85 % of the total storage of the entire system. Carrying out an additional analysis of the discharge downstream, we show that the Lancang dam system can retain up to $\sim$ 50 % of the natural flow during the wet season and control up to $\sim$ 89 % of the dry-season flow at Chiang Sean station, located nearby the outlet of the Lancang Basin.

In the second problem (Chapter 3), we leverage satellite data to solve the problem of the lack of data for calibrating macro-scale hydrological models in poorly gauged and heavily regulated basins. Those data include reservoir operations, which, if omitted,

can affect model parameterization, and observed river discharge data, which the simulated discharge is compared against to adjust the tuning parameters of the model. For the lack of data on reservoir operations, we make use of the result of the first problem. For the lack of river discharge data, we use a new approach. Specifically, we first couple our hydrological VIC-Res model with a hydraulic model, which converts satellite altimetry water level data to river discharge for model calibration. Using Global Sensitivity Analysis, we find a strong co-dependence between the parameterization of the Manning coefficient—the parameter in the hydraulic model—and the performance metrics that we use to evaluate the accuracy of VIC-Res. The results provided by sensitivity analysis help us to constrain the parameter of the hydraulic model. Finally, we carry out a calibration exercise for the hydrological model with the aid of ε-NSGA-II (a multi-objective optimization algorithm). We apply our approach to the same study site in the first problem—the Lancang River Basin. The performances of model calibration with remote-sensed discharge data and validation with observed discharge data at Chiang Saen show a remarkable result if we consider that no gauged data were used.

In the last problem (Chapter 4), we use a simulation-optimization approach, which includes a hydrological model—VIC-Res—and a multi-objective evolutionary algorithm—ε-NSGA-II to optimize the filling strategy for the Lancang dam system. By parameterizing the filling strategy, and changing the parameters in their feasible ranges with the aid of ε-NSGA-II, we explore a large number of alternative filling strategies. VIC-Res model simulates the filling process based on the input of the filling strategy and calculates reservoir release and downstream discharge. Those outputs are used to calculate the objective functions, which ε-NSGA-II uses to evaluate and adjust the filling strategy parameters. Our experiment results in 280 non-dominated solutions equivalent to 280 optimal filling strategies. Interestingly, the actual filling strategy behaves like a non-dominated solution. Our analysis shows that the actual filling strategy is favorable for upstream with a high value of average annual hydropower production and a high level of downstream flow alteration. Lastly, we show that if one of the more balanced filling strategies was applied instead of the actual strategy, the upstream country would have received slightly less hydropower, however, there would have been a significant decrease in the level of downstream flow alteration.

5.2 Future Works

From the limitations discussed in each chapter, we notice that there are several areas for further improvement. First, the data on reservoir operations that we produced have a monthly temporal solution. However, research on hydrology and water management often requires a better temporal solution (e.g., weekly and daily). In this regard, we think about synthesizing data from multiple satellite missions. Specifically, we would like to use a data fusion approach using other satellite images (e.g., MODIS, Sentinel) to create Landsat-like data (Wu et al., 2016; Salehi et al., 2021). Second, the approach that we use to construct the river cross-section only works well for a few locations (i.e., where the topography is in natural condition). It means the satellite data collected at many locations are not exploited. In this regard, we can develop a new approach for constructing river cross-sections, which is applicable to any or most of the locations along the river network. By doing that, we can exploit better the source of satellite data.

One of the ideas that we have in mind is a knowledge transfer model (Y. Liu et al., 2010), which is trained with a large number of surveyed river cross-sections and used to construct river cross-sections in unsurveyed areas based on the available remote-sensed data around the location of river cross-sections.

In regard to applications, a potentially impactful work is to build supporting tools or databases for riparian countries in managing transboundary water. First, based on the approach in Chapter 2, a tool for (near) real-time reservoir operation monitoring can be developed. This tool is absolutely helpful in the case that the upstream counties do not share the data. Besides, when the upstream countries agree to be part of basin water agreements/treaties, this tool will be an unbiased monitoring tool to make sure that the agreements/treaties (e.g., commitment to maintaining a certain amount of release from reservoirs to downstream) are implemented efficiently. It is also worth noting that there are existing reservoir operation monitoring tools (e.g., Mekong Dam Monitor (Eyler, Basist, et al., 2020) and RAT (Biswas, F. Hossain, Bonnema, Lee, et al., 2021)). However, as discussed in 1.2 and 2.1, all satellite data have their own limitations, which affect the usability of the tool using those data. The algorithm in our approach for removing the effect of cloud cover in Landsat images can increase the usability of the tool. Second, with the reliability of hydrological models in heavily regulated and poorly gauged river basins improved, we can build a database of river discharge. This database is absolutely helpful for downstream countries in transboundary river basins because knowing how much water and when they can receive water from upstream is necessary for preparing their water management and adaptation plans.

Lastly, the approach to optimize the reservoir filling strategy (Chapter 4) is helpful, especially in the context when there are more and more dams being constructed and planned to be built in the transboundary river basins (WLE Mekong, 2016; Schmitt et al., 2019; Wang et al., 2022). Although the filling strategy is decided by the upper countries (the dam owners), the assessment of the planned filling strategies could be a strong supporting point for the downstream countries in their negotiation with the upper countries for a more 'friendly' filling strategy. However, it is also worth noting that negotiations among riparian countries over the filling strategy of new dams are also affected by other factors such as the relationship among riparian countries, the potential of economy or military of riparian countries. Another research avenue that can be developed from Chapter 4 is to design the filling strategy for planned reservoirs with meteorology and stream flow forecast under the impacts of climate change. Under the impacts of climate change, there will be more extreme weather events. In addition, the impacts of climate change on the transboundary river basins—which are often large and may spread across different climate regions—are different throughout the basin (Hansford, Plink-Björklund, and Jones, 2020). Such research could be interesting and beneficial for all riparian countries.

Appendix A

Supplement of Chapter 2

TEXT A.1: Commonalities and differences between our study and the Mekong Dam Monitor

Both our study and the Mekong Dam Monitor (MDM) are based on the idea of extracting the water extent of the reservoirs from satellite images and then converting it into water level and storage by using the information from a Digital Elevation Model (DEM). However, there are a few key differences. First, we use an image improvement algorithm, which is important and necessary because it enables us to extract the information on reservoir storage from Landsat images for a long period (2008–2020). Meanwhile, to avoid the cloud contamination in satellite images, MDM looks to other remote sensing products, such as the Sentinel-SAR (Synthetic Aperture Radar), which can "pierce" through clouds. However, Sentinels were launched recently (in April 2014), so the information before that time (including the construction and filling periods of five reservoirs on the mainstream of the Lancang) cannot be revealed. Second, with the water extent estimation provided by our algorithm, we directly infer water level and storage through the elevation-area-storage curves estimated from the DEM. Meanwhile, MDM calculates the average elevation at the reservoir shoreline, and then converts it into storage. This way may not work well for all water surface images. Finally, to strengthen our results, we make use of water level from Altimetry data (where available) to validate the results obtained by processing the Landsat images.

TABLE A.1: Design specifications of the hydropower dams on the mainstream of the Lancang River. Retrieved from Do et al. (2020).

Name	COM	Dam height (m)	Max WL (m a.s.l.)	Dead WL (m a.s.l.)	Max WSA (km²)	Dead storage (MCM)	Full storage (MCM)	Installed capacity (MW)
Jinghong	2009	108	602	595	510	810	1119	1750
Nuozhadu	2014	262	812	756	320	10414	21749	5850
Dachaoshan	2003	115	899	887	826	465	740	1350
Manwan	1992	132	994	982	415	630	887	1670
Xiaowan	2010	292	1236	1162	194	4750	14645	4200
Gongguoqiao	2012	105	1319	1311	343	196	316	900
Miaowei	2016	140	1408	1373	171	359	660	1400
Dahuaqiao	2018	106	1477	1466	148	252	293	920
Huangdeng	2017	203	1619	1604	199	1031	1418	1900
Tuoba	2023	158	1735	1725	177	735	1039	1400
Lidi	2019	74	1818	1813	4	57	71	420
Wunonglong	2018	138	1906	1894	163	236	272	990

COM Commission year
WL Water level
WSA Water surface area

FIGURE A.1: Comparison between Landsat-derived water level (green line), Jason altimetry water level (blue dots), and Sentinel-1-derived water level (orange dashed line) archived from Mekong Dam Monitor platform for Nuozhadu (left) and Xiaowan (right) reservoirs. Note that Jason has a 10-day temporal resolution and Sentinel-1 have a frequency of up to 6 days (Sentinel-1A and B have a frequency of 12 days and interleave to each other). The comparison shows that the use of a monthly resolution yields the same trajectories of a weekly one.

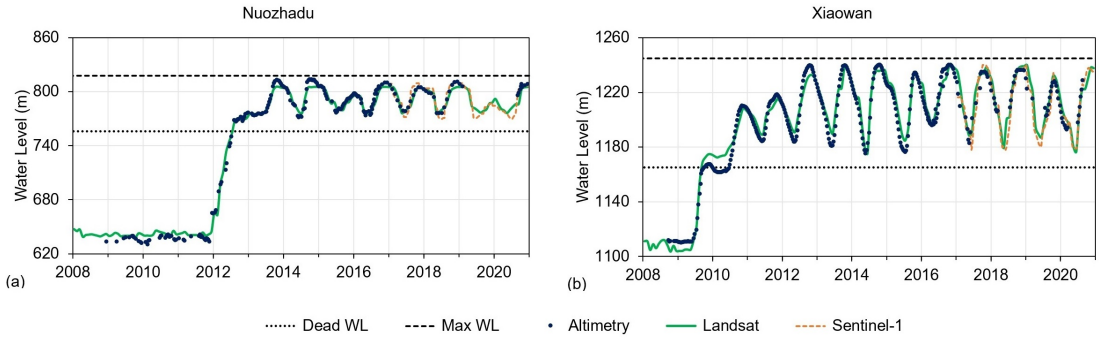

FIGURE A.2: E-A, A-S, and E-S curves of Bhumibol reservoir (top) and Ubol Ratana reservoir (bottom). The curves are represented by light blue lines, which are fitted to the data points (blue circles) derived from the DEM data. Note that the curves intersect the points identified by maximum water level, maximum water surface area, and full storage volume (dashed lines) as well as those identified by dead water level and dead storage volume (dotted lines). The green lines reported in panels (c) and (f) correspond to the observations by Electricity Generating Authority of Thailand (EGAT).

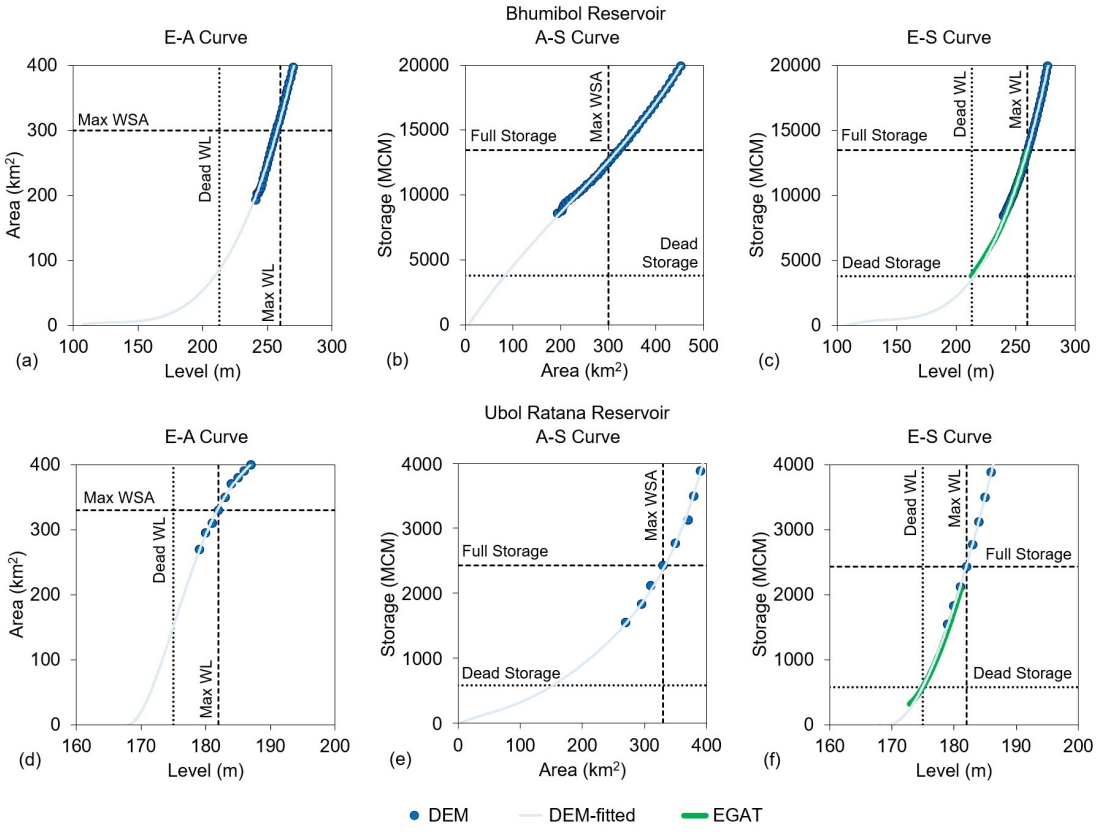

TABLE A.2: The differences in storage corresponding to each water level in the variation range of Xiaowan and Nuozhadu reservoirs obtained by using the trapezoidal approximation [1] and direct calculation from the DEM [2].

Xiaowan				Nuozhadu			
Water level (m)	Storage [1] (MCM)	Storage [2] (MCM)	Difference (%)	Water level (m)	Storage [1] (MCM)	Storage [2] (MCM)	Difference (%)
1162	4077	4149	1.74	766	10501	10678	1.67
1164	4223	4298	1.74	768	10859	11042	1.65
1166	4375	4452	1.73	770	11227	11414	1.64
1168	4531	4611	1.74	772	11605	11797	1.63
1170	4693	4776	1.74	774	11992	12189	1.62
1172	4862	4948	1.74	776	12390	12592	1.61
1174	5036	5126	1.74	778	12798	13005	1.59
1176	5217	5309	1.74	780	13216	13428	1.58
1178	5403	5498	1.73	782	13645	13862	1.57
1180	5595	5692	1.71	784	14084	14307	1.56
1182	5792	5892	1.70	786	14534	14763	1.55
1184	5994	6096	1.68	788	14995	15230	1.54
1186	6201	6306	1.67	790	15468	15709	1.53
1188	6413	6520	1.65	792	15953	16199	1.52
1190	6630	6741	1.64	794	16450	16702	1.51
1192	6853	6966	1.62	796	16958	17217	1.50
1194	7081	7197	1.61	798	17479	17743	1.49
1196	7316	7434	1.60	800	18012	18283	1.48
1198	7555	7677	1.59	802	18557	18834	1.47
1200	7801	7925	1.57	804	19115	19399	1.46
1202	8052	8179	1.56	806	19686	19975	1.45
1204	8308	8438	1.54	808	20269	20565	1.44
1206	8570	8703	1.53	810	20865	21167	1.43
1208	8838	8974	1.51	812	21473	21781	1.42
1210	9112	9251	1.50				
1212	9392	9534	1.49				
1214	9678	9823	1.47				
1216	9970	10118	1.46				
1218	10268	10419	1.45				
1220	10572	10726	1.44				
1222	10882	11039	1.42				
1224	11198	11358	1.41				
1226	11521	11684	1.40				
1228	11849	12015	1.38				
1230	12184	12353	1.37				
1232	12525	12697	1.36				
1234	12872	13047	1.35				
1236	13225	13404	1.33				
1238	13584	13766	1.32				
1240	13950	14134	1.30				
1242	14321	14508	1.29				

TABLE A.3: Spectral indices for water surface extraction.

Index	Formula	Recommended threshold values
NDVI	(Red - Green)/(Red + Green)	0 (Zhai et al., 2015) and 0.1 (Huilin Gao, C. Birkett, and Lettenmaier, 2012)
NDWI	(Green - NIR)/(Green + NIR)	0 (Zhai et al., 2015; Bonnema and F. Hossain, 2017)
MNDWI	(Green - MIR)/(Green + MIR)	0 and 0.1 Duan and Bastiaanssen, 2013

NDVI	Normalized Difference Vegetation Index
NDWI	Normalized Difference Water Index
MNDWI	Modified Normalized Difference Water Index
NIR	Near Infrared
MIR	Middle Infrared

TABLE A.4: Performance of the water surface area estimation algorithm for the reservoirs on the Lancang River.

Reservoir	Number of available images	Percentage of usable images	
		Before improvement	After improvement
	Dry season (Dec-May)		
Jinghong	175	24 %	89 %
Nuozhadu	187	27 %	89 %
Dachaoshan	187	26 %	89 %
Manwan	187	25 %	85 %
Xiaowan	187	27 %	88 %
Gongguoqiao	173	34 %	75 %
Miaowei	173	36 %	84 %
Dahuaqiao	173	36 %	82 %
Huangdeng	164	34 %	85 %
Wunonglong	164	34 %	73 %
Total	1770	30 %	84 %
	Wet season (Jun-Nov)		
Jinghong	122	20 %	80 %
Nuozhadu	127	13 %	69 %
Dachaoshan	130	16 %	76 %
Manwan	131	18 %	77 %
Xiaowan	130	16 %	88 %
Gongguoqiao	118	23 %	69 %
Miaowei	118	27 %	90 %
Dahuaqiao	118	28 %	81 %
Huangdeng	120	27 %	78 %
Wunonglong	120	20 %	81 %
Total	1234	21 %	79 %
	Total		
Jinghong	297	22 %	85 %
Nuozhadu	314	21 %	81 %
Dachaoshan	317	22 %	84 %
Manwan	318	22 %	82 %
Xiaowan	317	23 %	88 %
Gongguoqiao	291	29 %	72 %
Miaowei	291	32 %	87 %
Dahuaqiao	291	33 %	81 %
Huangdeng	284	31 %	82 %
Wunonglong	284	28 %	76 %
Total	3004	26 %	82 %

TABLE A.5: Quantitative comparison of Landsat-derived and altimetry-converted water surface area.

Reservoir	R (CC)	RMSE (km²)	NRMSE
Nuozhadu	0.994	13.941	0.049
Xiaowan	0.977	9.901	0.062
Huangdeng	0.977	1.884	0.077
Jinghong	0.558	0.428	0.020

TABLE A.6: The statistical indices of the annual peak and lowest discharge at Chiang Saen station for two periods: before and after the two biggest dams (Nuozhadu and Xiaowan) began operations.

	Peak Discharge (cms)				Lowest Discharge (cms)			
	Mean	Q1	Median	Q3	Mean	Q1	Median	Q3
1990 - 2008	11157	9235	10700	12350	638	551	599	759
2013 - 2020	6476	5213	6834	7866	966	844	975	1077
Change	-45 %	-45 %	-43 %	-42 %	57 %	69 %	65 %	42 %

FIGURE A.3: Water surface area (a,b) and storage variations (c,d) of Bhumibol reservoir (left) and Ubol Ratana reservoir (right). In panels (a,b), note the drastic difference in WSA values before (light blue points) and after (cyan points) the classification improvement. The corrected values of WSA are well in agreement with those converted from observed water level (EGAT) through E-A curves (blue dashed lines). In panels (c,d), note the similarity in the storage volume derived from Landsat images (cyan dotted lines) and observed data from EGAT (blue lines).

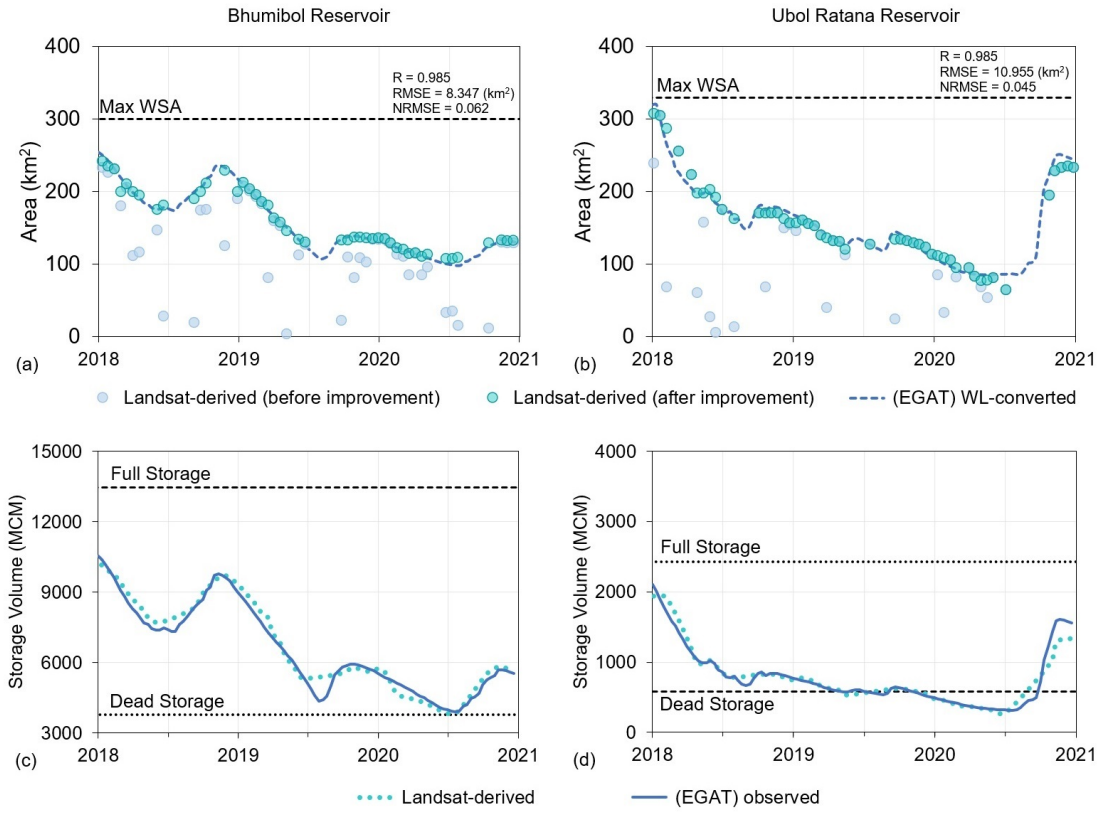

FIGURE A.4: E-S curve of Nouzhadu (left) and Xiaowan (right) reservoirs obtained by using the trapezoidal approximation and direct calculation from the DEM.

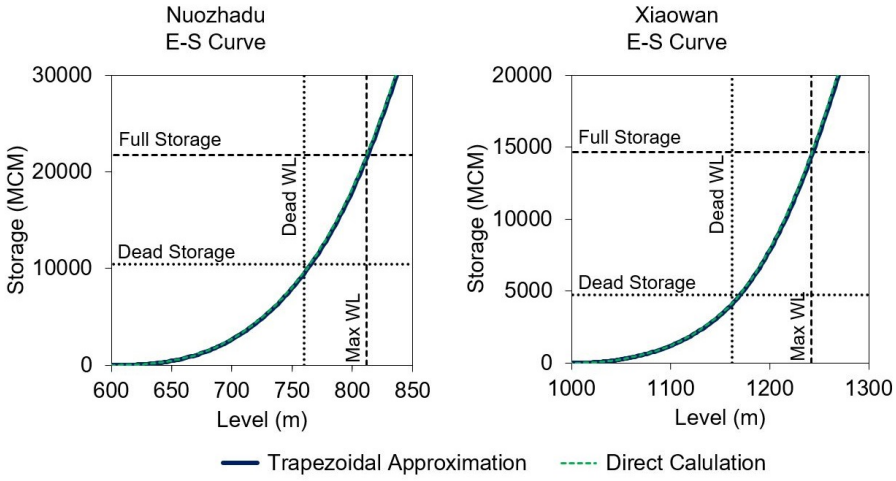

FIGURE A.5: Performance of three spectral indices (NDVI, NDWI, and MNDWI) in extracting the water surface area of Xiaowan reservoir. Results are reported for three threshold values, 0, 0.05, and 0.1, and compared to the Maximum Water Extent dataset, developed by the European Commission's Joint Research Centre (Pekel et al., 2016). The meaning of the three indices is explained in Table A.3.

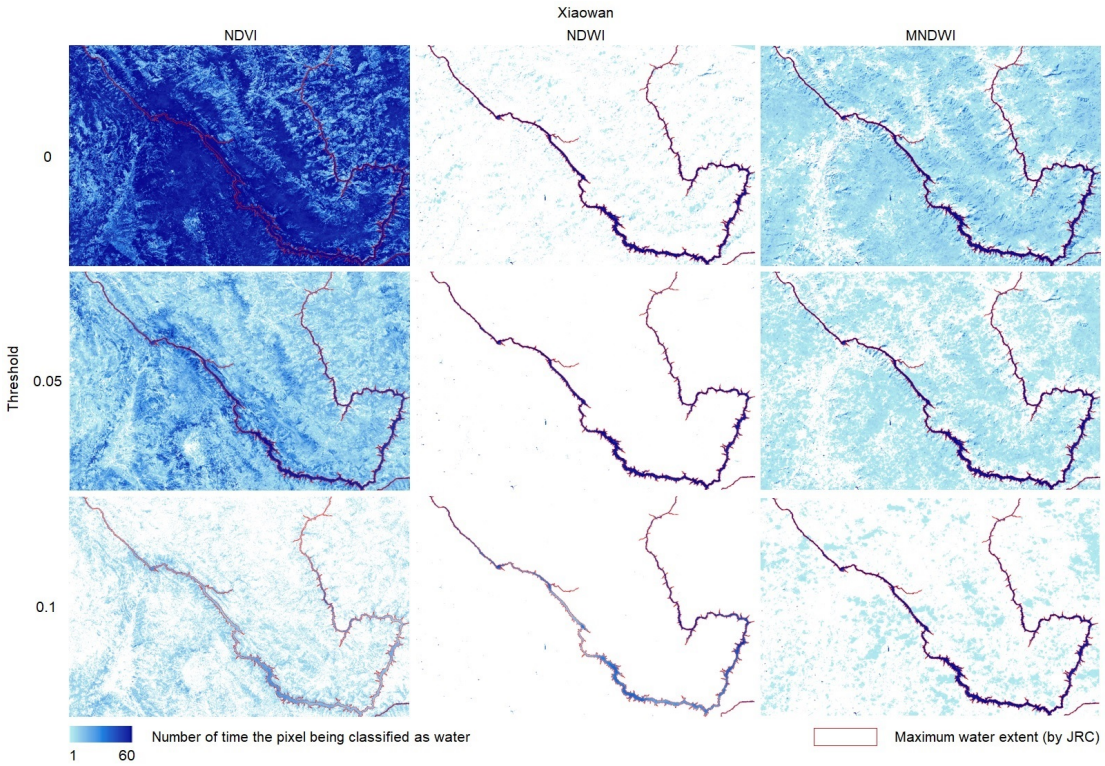

FIGURE A.6: Performance of three spectral indices (NDVI, NDWI, and MNDWI) in extracting the water surface area of Nuozhadu reservoir. Results are reported for three threshold values, 0, 0.05, and 0.1, and compared to the Maximum Water Extent dataset, developed by the European Commission's Joint Research Centre (Pekel et al., 2016). The meaning of the three indices is explained in Table A.3.

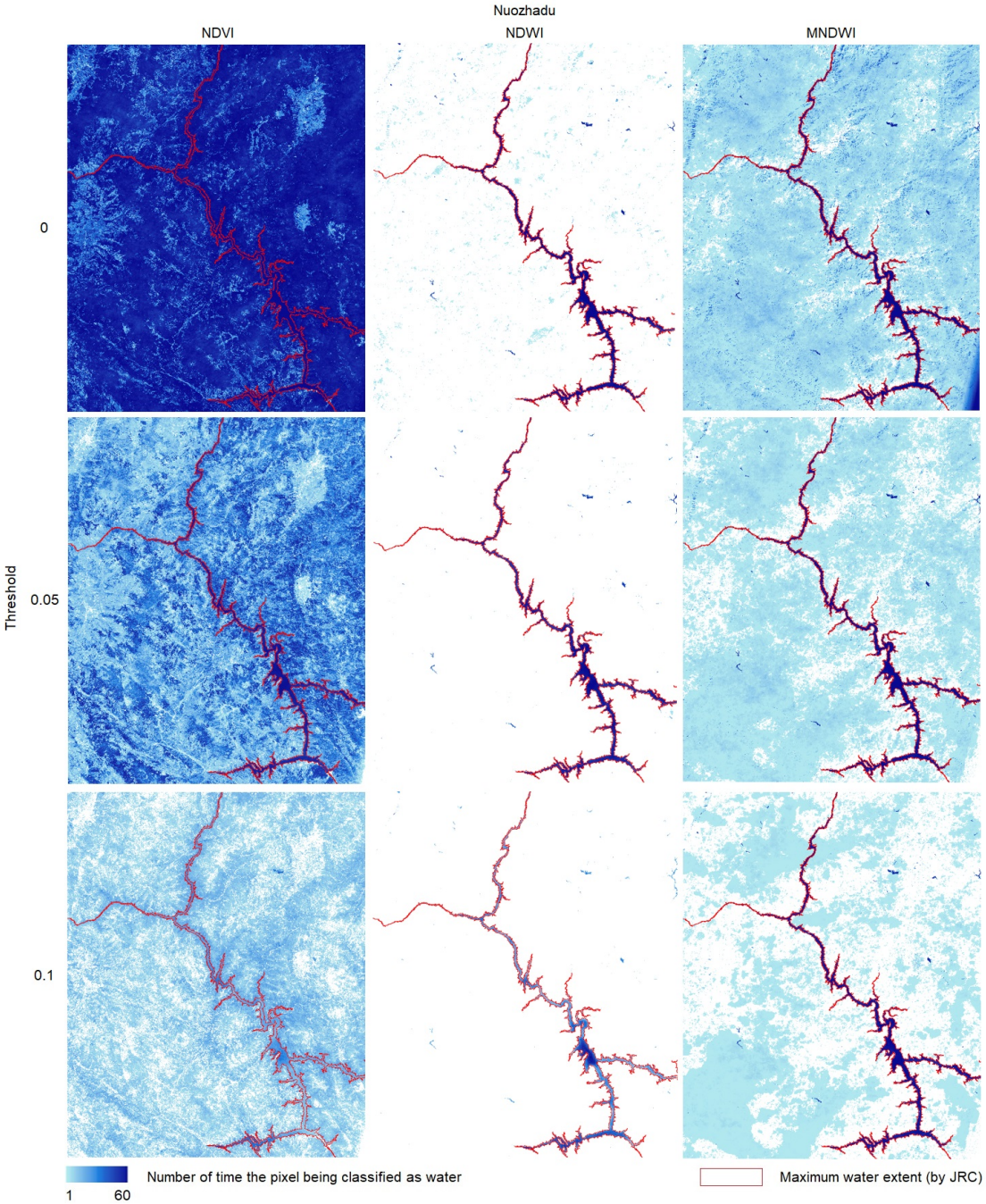

FIGURE A.7: Comparison of the simulated discharge by VIC-Res (blue dots) and observed discharge (grey line) at Chiang Sean for the period 2009-2019 (filling period of Xiaowan and Nuozhadu reservoirs). Observed data are archived from Mekong River Commission (MRC).

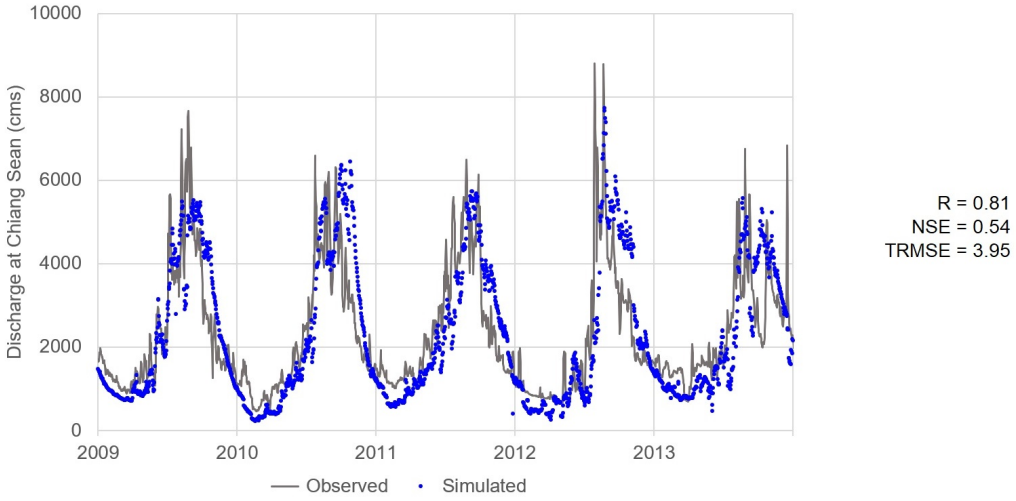

FIGURE A.8: Comparison of storage derived from Landsat images and VIC-Res model for Nuozhadu (left) and Xiaowan (right) reservoirs.

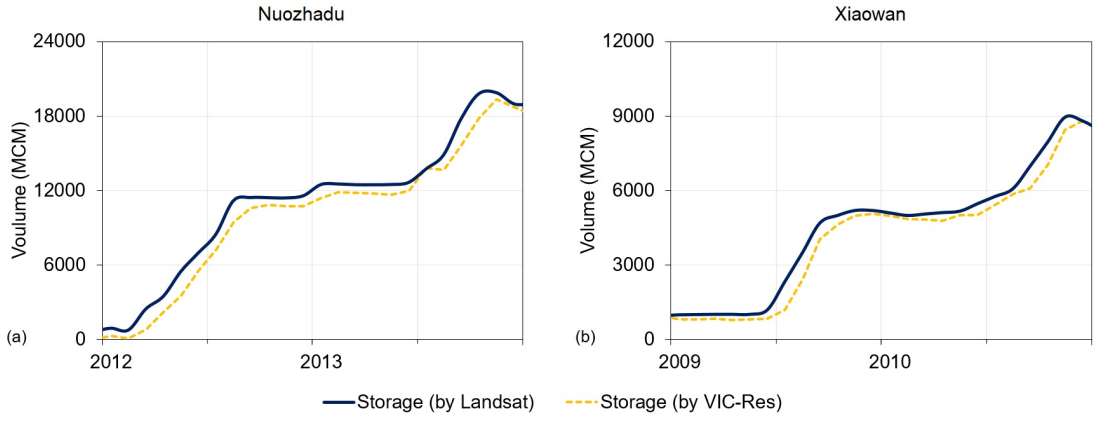

FIGURE A.9: E-A, A-S and E-S curves of Jinghong, Dachaoshan, Manwan and Gongguoqiao reservoirs.

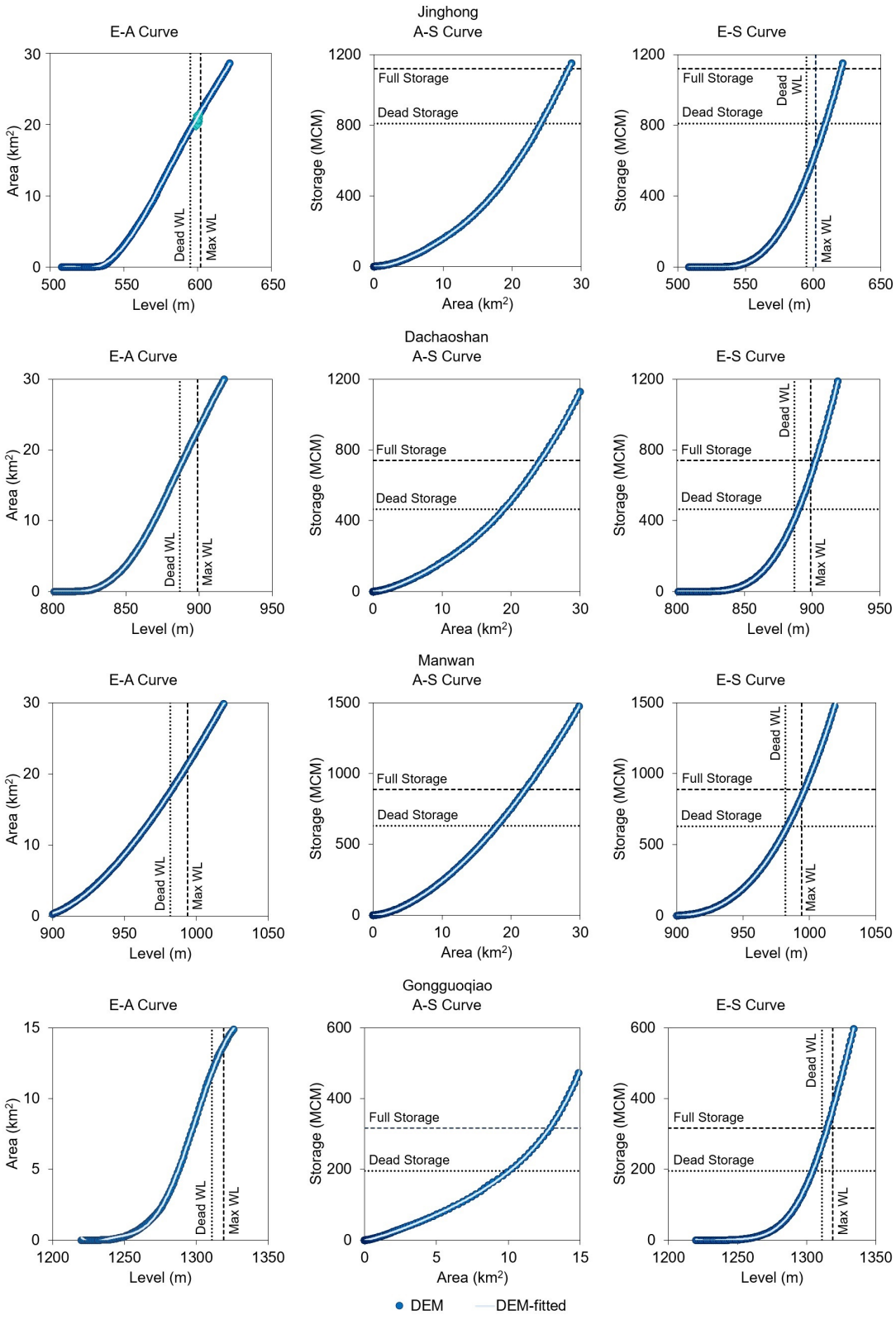

FIGURE A.10: E-A, A-S and E-S curves of Miaowei, Dahuaqiao, Huangdeng and Wunonglong reservoirs.

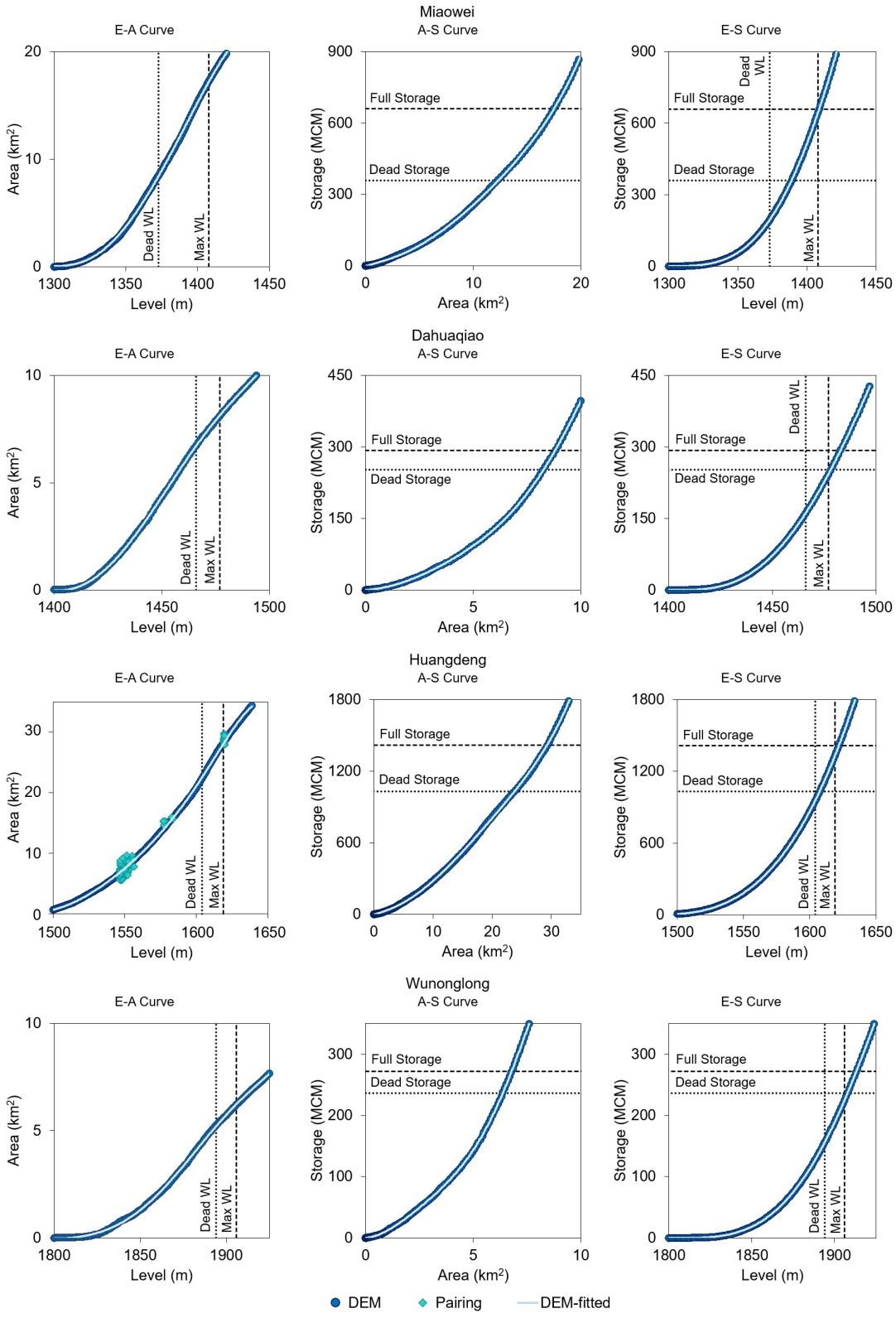

FIGURE A.11: Water surface area of Huangdeng (top) and Jinghong (bottom) reservoirs. Note the drastic difference in WSA values before (lightblue points) and after (cyan points) the classification improvement. The corrected values of WSA are well in agreement with those obtained through altimetry water level data and E-A curves (dark blue points)

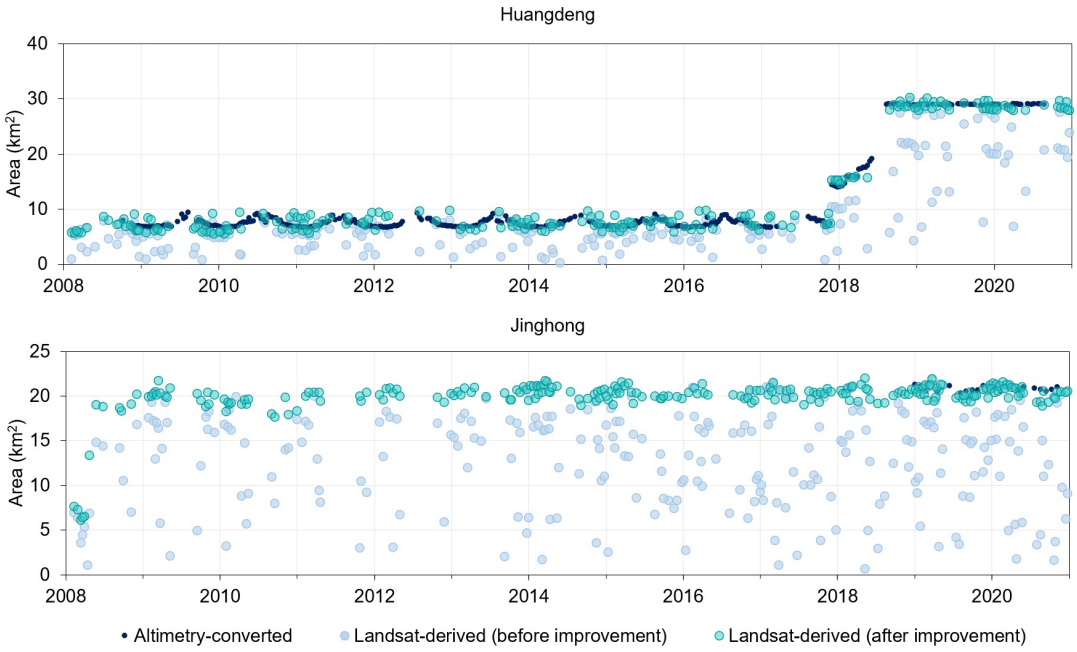

FIGURE A.12: Storage variation of reservoirs on the Lancang River.

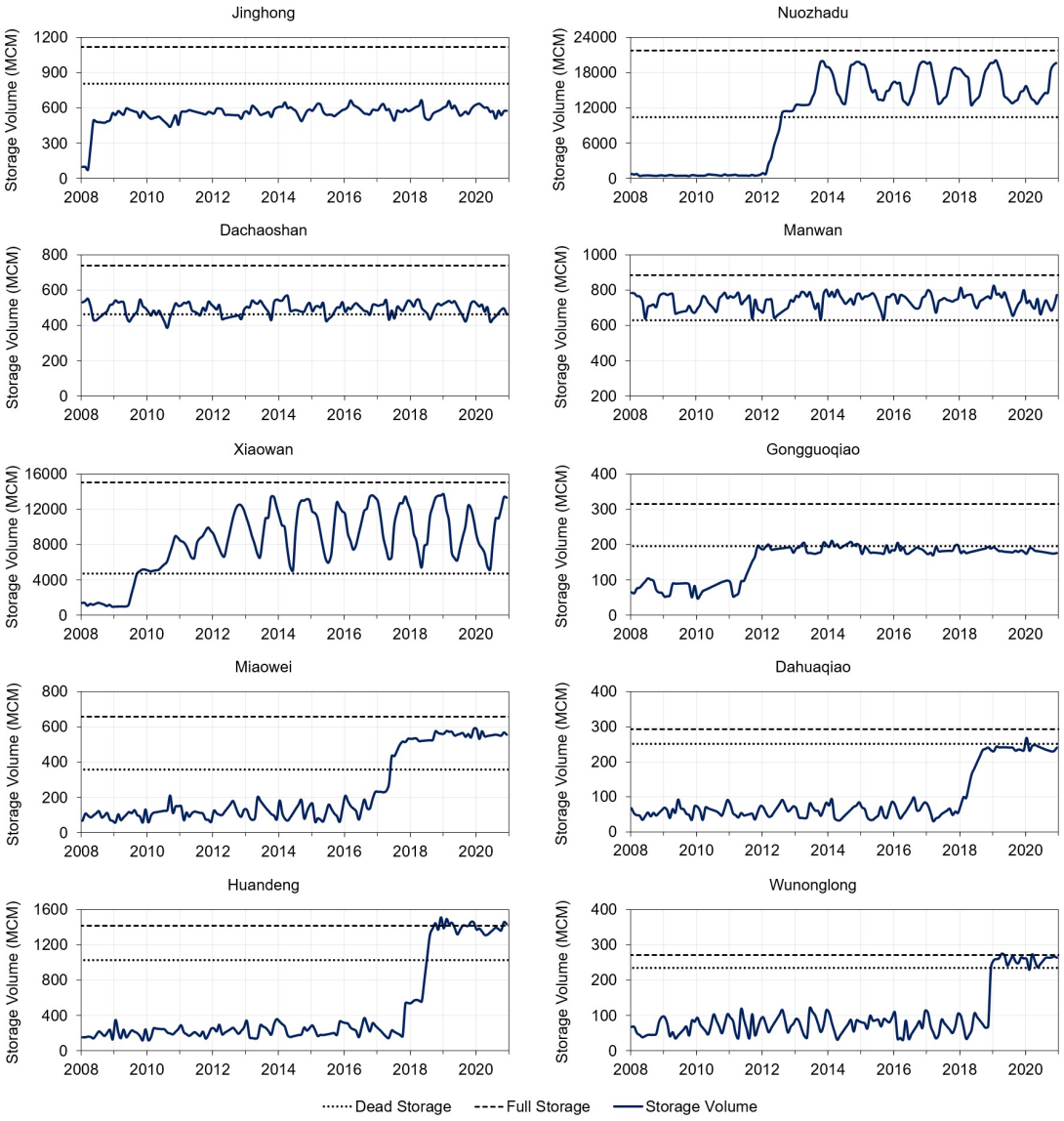

FIGURE A.13: Operation curves of 8 reservoirs (Jinghong, Dachaoshan, Manwan, Gongguoqiao, Miaowei, Dahuaqiao, Huangdeng and Wunonglong).

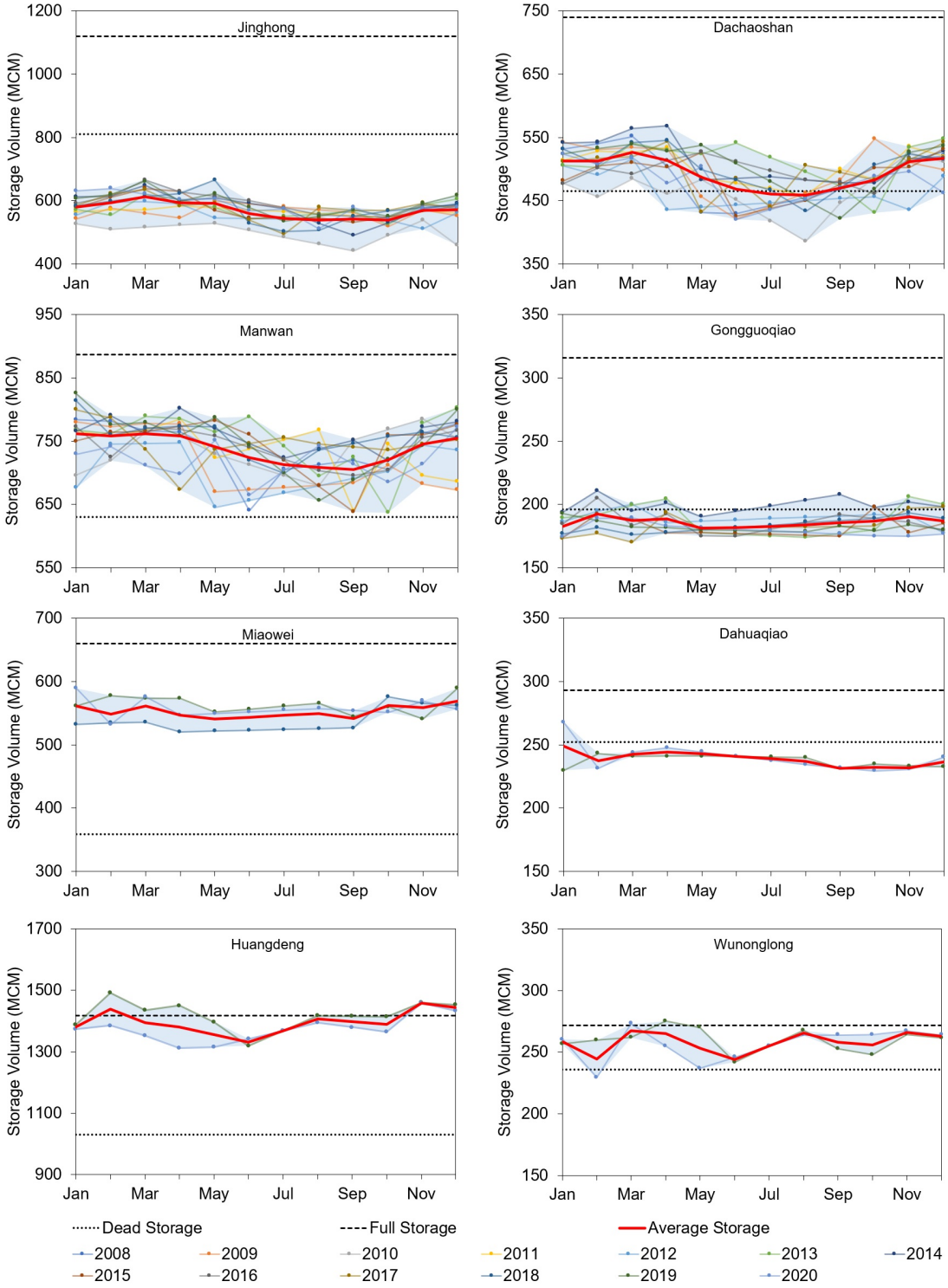

FIGURE A.14: Upper panel: graphical illustration of total storage and discharge at Chiang Saen station. Middle panel: wavelet analysis of the discharge. Colors represent wavelet power, while confidence level contours identify statistically significant power. The flow regime changed in 2014, when Nuozhadu reservoir started its normal operations. Bottom panel: wavelet coherency and phase between discharge and reservoir storage. Contours identify statistically significant coherencies. The vectors indicate the phase difference between discharge and storage.

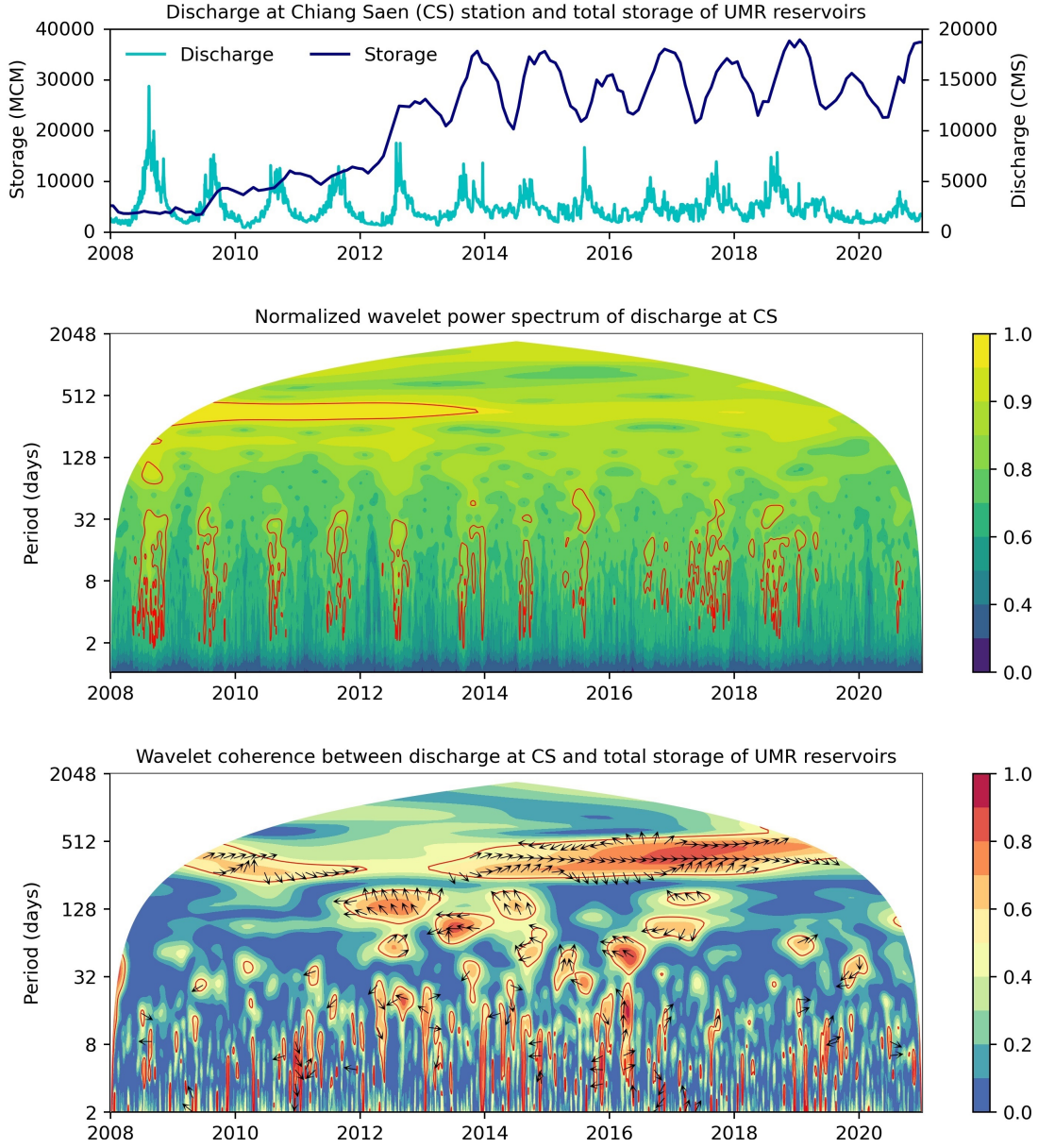

Appendix B

Supplement of Chapter 3

TABLE B.1: List of Landsat 5 images used to identify the river cross-section at the virtual station.

ID	Collection date (dd/mm/yyyy)	River width (m)	Water level* (m)
LT05_L1TP_129046_20080929_20161029_01_T1	29/09/2008	240	298.36
LT05_L1TP_129046_20081015_20161029_01_T1	15/10/2008	240	297.47
LT05_L1TP_129046_20081202_20170111_01_T1	02/12/2008	210	291.89
LT05_L1TP_129046_20081218_20170111_01_T1	18/12/20008	210	290.75
LT05_L1TP_129046_20090119_20161028_01_T1	19/01/2009	210	288.80
LT05_L1TP_129046_20090220_20161027_01_T1	20/02/2009	180	287.39
LT05_L1TP_129046_20090308_20161029_01_T1	08/03/2009	180	286.77
LT05_L1TP_129046_20091018_20161019_01_T1	18/10/2009	210	293.50
LT05_L1TP_129046_20091103_20161023_01_T1	03/11/2009	210	292.51
LT05_L1TP_129046_20091205_20161017_01_T1	05/12/2009	210	288.93
LT05_L1TP_129046_20100207_20161017_01_T1	07/02/2010	180	285.88
LT05_L1TP_129046_20100223_20161016_01_T1	23/02/2010	180	284.06
LT05_L1TP_129046_20100428_20161015_01_T1	28/04/2010	180	287.85
LT05_L1TP_129046_20100514_20161015_01_T1	14/05/2010	180	287.22
LT05_L1TP_129046_20100903_20161014_01_T1	03/09/2010	240	297.37
LT05_L1TP_129046_20101106_20161012_01_T1	06/11/2010	210	293.59
LT05_L1TP_129046_20110125_20161010_01_T1	25/01/2011	210	288.38
LT05_L1TP_129046_20110210_20161010_01_T1	10/02/2011	180	287.45
LT05_L1TP_129046_20110415_20161209_01_T1	15/04/2011	180	287.74

* obtained by Jason-2/3 on the corresponding day

TABLE B.2: Model calibration performance calculated for 12 selected solutions, i.e., those yielding the top 25 % performance in terms of NSE, TRMSE, MSDE, and ROCE. The performance metrics are calculated by comparing simulated and remote-sensed discharge at the virtual station.

No.	NSE	TRMSE	MSDE	ROCE
1	0.689	3.353	891526	0.035
2	0.689	3.353	891388	0.035
3	0.689	3.354	890904	0.035
4	0.688	3.360	897298	0.040
5	0.687	3.356	891553	0.030
6	0.687	3.345	908805	0.033
7	0.687	3.345	908805	0.033
8	0.686	3.343	891400	0.036
9	0.686	3.343	891400	0.036
10	0.686	3.343	890948	0.036
11	0.686	3.343	891457	0.036
12	0.686	3.337	891369	0.039

TABLE B.3: Model validation performance calculated for the 12 selected solutions, i.e., those yielding the top 25 % performance in terms of NSE, TRMSE, MSDE, and ROCE. The performance metrics are calculated by comparing simulated and observed discharge at Chiang Saen station.

No.	NSE	TRMSE	MSDE	ROCE
1	0.616	3.908	1062099	0.169
2	0.608	3.919	1058180	0.183
3	0.608	3.919	1058419	0.183
4	0.608	3.920	1057966	0.183
5	0.599	3.891	1058223	0.170
6	0.598	3.904	1058282	0.177
7	0.598	3.904	1058282	0.177
8	0.598	3.906	1058083	0.178
9	0.598	3.905	1058305	0.178
10	0.596	3.935	1058645	0.195
11	0.594	3.911	1071282	0.187
12	0.594	3.911	1071282	0.187

TABLE B.4: Model calibration performance calculated for the 58 selected solutions (the Pareto front) from model calibration. The performance metrics are calculated between simulated and remote-sensed discharge at the virtual station.

No.	NSE	TRMSE	MSDE	ROCE	No.	NSE	TRMSE	MSDE	ROCE
1	0.698	3.375	1065802	0.041	30	0.688	3.330	1119978	0.027
2	0.697	3.363	1064265	0.046	31	0.688	3.372	883766	0.038
3	0.696	3.420	1104404	0.013	32	0.687	3.265	1240258	0.057
4	0.696	3.333	1296485	0.022	33	0.687	3.356	891553	0.030
5	0.696	3.374	1061290	0.042	34	0.687	3.336	897516	0.047
6	0.695	3.377	1060950	0.041	35	0.687	3.410	884122	0.035
7	0.695	3.379	1039961	0.040	36	0.687	3.407	885826	0.036
8	0.695	3.301	1298463	0.032	37	0.687	3.345	908805	0.033
9	0.694	3.366	1172060	0.028	38	0.687	3.398	883010	0.037
10	0.694	3.300	1296746	0.032	39	0.686	3.432	854452	0.038
11	0.694	3.301	1297546	0.032	40	0.686	3.343	891400	0.036
12	0.693	3.329	973419	0.041	41	0.686	3.343	890948	0.036
13	0.693	3.324	963126	0.041	42	0.686	3.420	883425	0.037
14	0.693	3.311	1300094	0.024	43	0.686	3.337	891369	0.039
15	0.692	3.310	1298422	0.024	44	0.685	3.271	1238422	0.059
16	0.692	3.303	1121617	0.032	45	0.685	3.447	864589	0.037
17	0.692	3.305	1118386	0.031	46	0.685	3.465	858494	0.037
18	0.692	3.286	1237423	0.039	47	0.681	3.422	880224	0.045
19	0.691	3.307	977172	0.043	48	0.680	3.348	1286568	0.024
20	0.691	3.387	1170933	0.018	49	0.679	3.363	1269557	0.018
21	0.691	3.308	1230897	0.025	50	0.679	3.379	1254975	0.014
22	0.690	3.386	1174178	0.019	51	0.673	3.452	793084	0.037
23	0.690	3.387	1174042	0.019	52	0.672	3.425	792973	0.028
24	0.690	3.295	1244238	0.038	53	0.670	3.428	793443	0.026
25	0.690	3.324	962490	0.049	54	0.670	3.428	793443	0.026
26	0.689	3.299	1244769	0.037	55	0.670	3.428	793443	0.026
27	0.689	3.353	891526	0.035	56	0.670	3.428	793443	0.026
28	0.689	3.353	891388	0.035	57	0.656	3.545	1285269	0.007
29	0.689	3.354	890904	0.035	58	0.646	3.588	892415	0.001

TABLE B.5: Model validation performance calculated for the 58 selected solutions (the Pareto front) from model calibration. The performance metrics are calculated between simulated and observed discharge at Chiang Saen station.

No.	NSE	TRMSE	MSDE	ROCE	No.	NSE	TRMSE	MSDE	ROCE
1	0.637	3.928	989984	0.174	30	0.594	3.911	1071282	0.187
2	0.635	3.897	988499	0.170	31	0.592	3.871	1211314	0.223
3	0.634	3.924	1002652	0.173	32	0.592	3.872	1211245	0.223
4	0.632	3.716	1093794	0.139	33	0.591	3.846	1335416	0.117
5	0.631	3.745	1093664	0.157	34	0.588	4.032	993374	0.201
6	0.625	3.944	1047262	0.158	35	0.586	3.845	1336296	0.123
7	0.624	3.731	1094157	0.152	36	0.581	4.041	994241	0.206
8	0.623	3.733	1094213	0.154	37	0.581	4.041	994241	0.206
9	0.622	3.737	1081727	0.156	38	0.581	4.041	994241	0.206
10	0.621	3.967	1050516	0.180	39	0.581	4.041	994241	0.206
11	0.620	3.851	1108955	0.143	40	0.574	3.923	1334334	0.174
12	0.619	3.957	1052596	0.180	41	0.570	3.950	1376977	0.192
13	0.619	3.948	1050599	0.177	42	0.569	3.928	1337789	0.177
14	0.619	3.963	1051327	0.183	43	0.568	3.960	949657	0.292
15	0.618	3.861	1059505	0.148	44	0.567	3.932	1337865	0.179
16	0.616	3.927	1051718	0.176	45	0.567	3.947	1248912	0.193
17	0.614	3.885	1119650	0.166	46	0.567	3.942	1386466	0.187
18	0.613	3.880	1112699	0.165	47	0.566	3.944	1386968	0.187
19	0.610	3.842	1207660	0.197	48	0.566	3.953	1246566	0.196
20	0.609	4.022	990455	0.180	49	0.566	3.942	1388012	0.188
21	0.608	3.919	1058180	0.183	50	0.564	4.001	1389071	0.218
22	0.608	3.919	1058419	0.183	51	0.561	3.970	1327052	0.214
23	0.605	3.883	1088908	0.171	52	0.557	3.977	1246317	0.205
24	0.602	3.847	1119397	0.159	53	0.553	3.981	1318489	0.243
25	0.599	3.891	1058223	0.170	54	0.552	3.975	1388532	0.211
26	0.598	3.904	1058282	0.177	55	0.551	3.973	1389883	0.210
27	0.598	3.841	1133345	0.236	56	0.545	3.992	1368735	0.216
28	0.598	3.906	1058083	0.178	57	0.539	4.015	1353742	0.232
29	0.596	3.935	1058645	0.195	58	0.512	4.190	1053505	0.276

FIGURE B.1: Approach for constructing the river cross-section at the virtual station (a) and elements of the river cross-section used to construct the rating curve (b). Note that the approach builds on multiple satellite data, namely DEM, altimetry, and river width (derived from Landsat images).

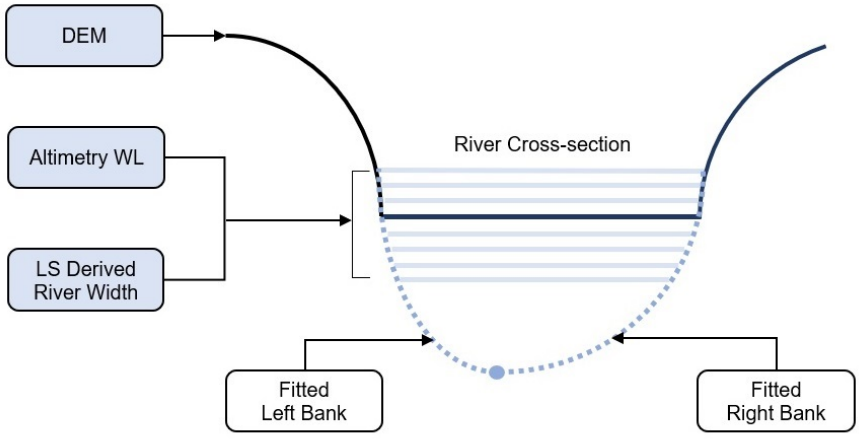

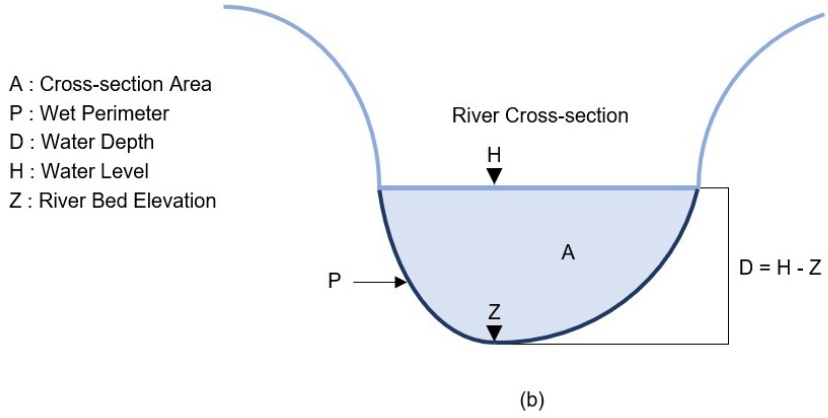

FIGURE B.2: Comparison between remote-sensed (RS) and simulated discharge at the virtual station. The range of variability of the RS discharge is represented by the medium blue band, while the range of simulated discharge (corresponding to new range of Manning's coefficient $n \in [0.04\text{-}0.052]$) is represented by the light green band. The RS discharge estimated with $n = 0.046$ is illustrated by the dark blue line. Finally, the dotted orange line illustrates the discharge estimated by scaling the discharge observed at Chiang Saen by the area ratio.

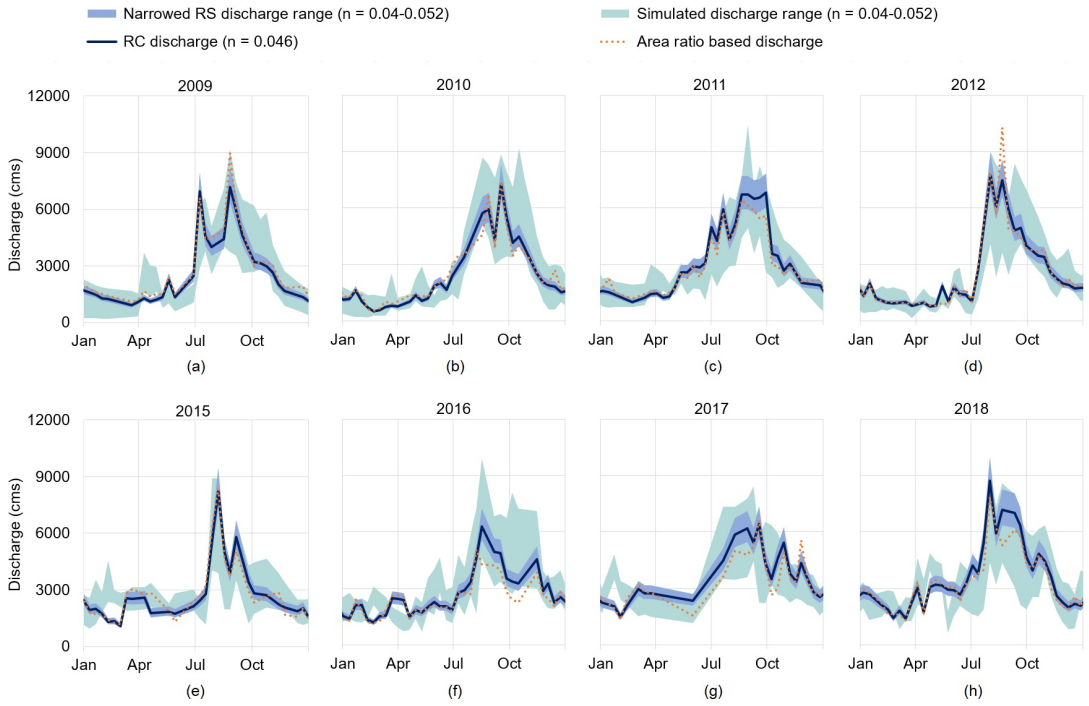

FIGURE B.3: Comparison of discharge time series obtained during calibration at the virtual station (a) and validation at Chiang Saen station (b). The dark green band depicts the range of variability of 58 selected solutions (corresponding to the Pareto front), while the light green band corresponds to the range of variability of 40 solutions selected in the sensitivity analysis. In panel (a), the dark blue line represents the remote-sensed discharge at the virtual station (with n = 0.046), while the dotted orange line corresponds to the discharge estimated by scaling the discharge observed at Chiang Saen by the area ratio. In panel (b), the dotted orange line illustrates the observed discharge at Chiang Saen.

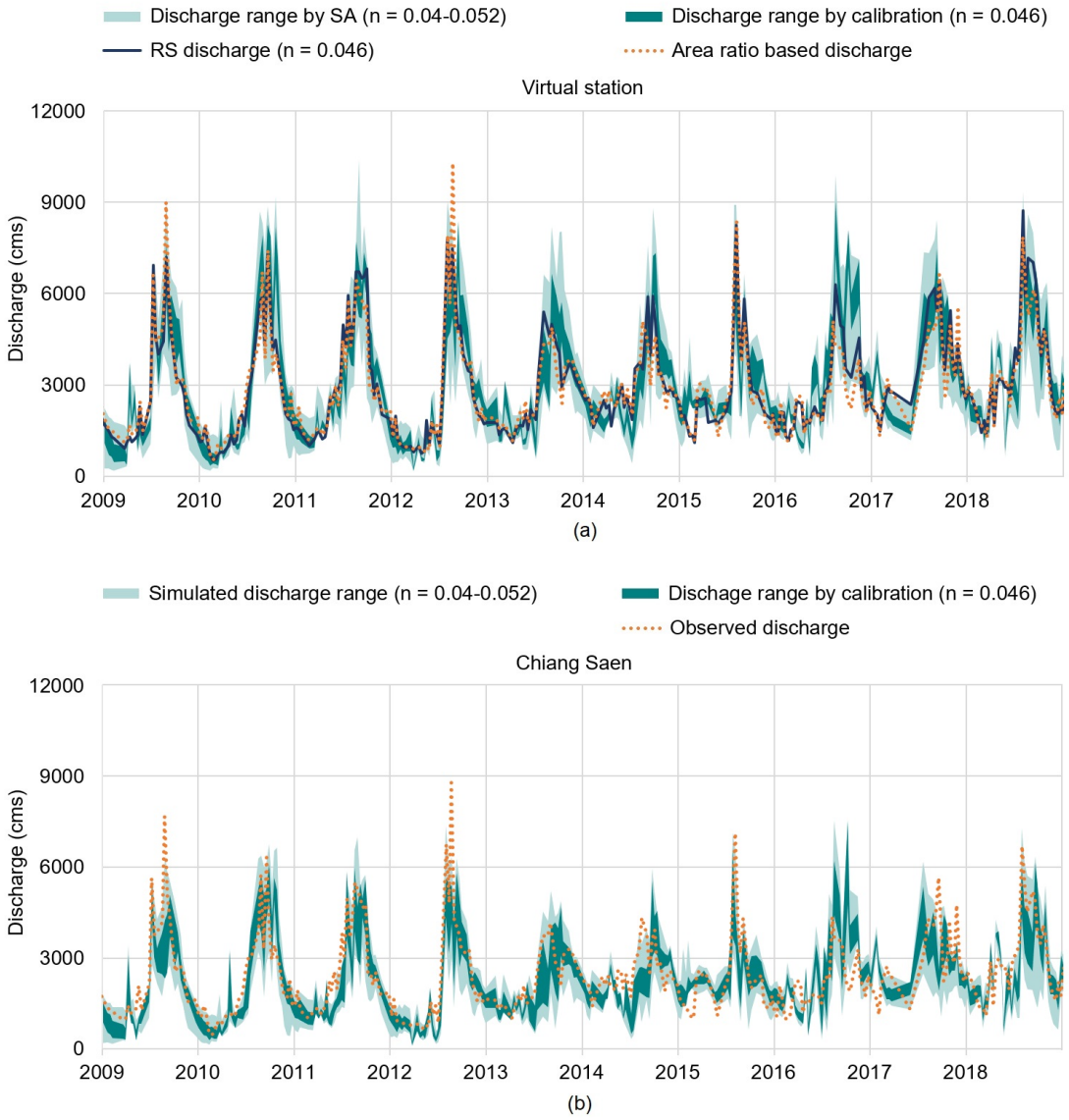

Appendix C

Supplement of Chapter 4

FIGURE C.1: Filling strategy of Jinghong, Manwan, Dachaoshan, Gonguoqiao, Miaowei, Dahuaqiao, Huangdeng, and Wunonglong reservoirs.

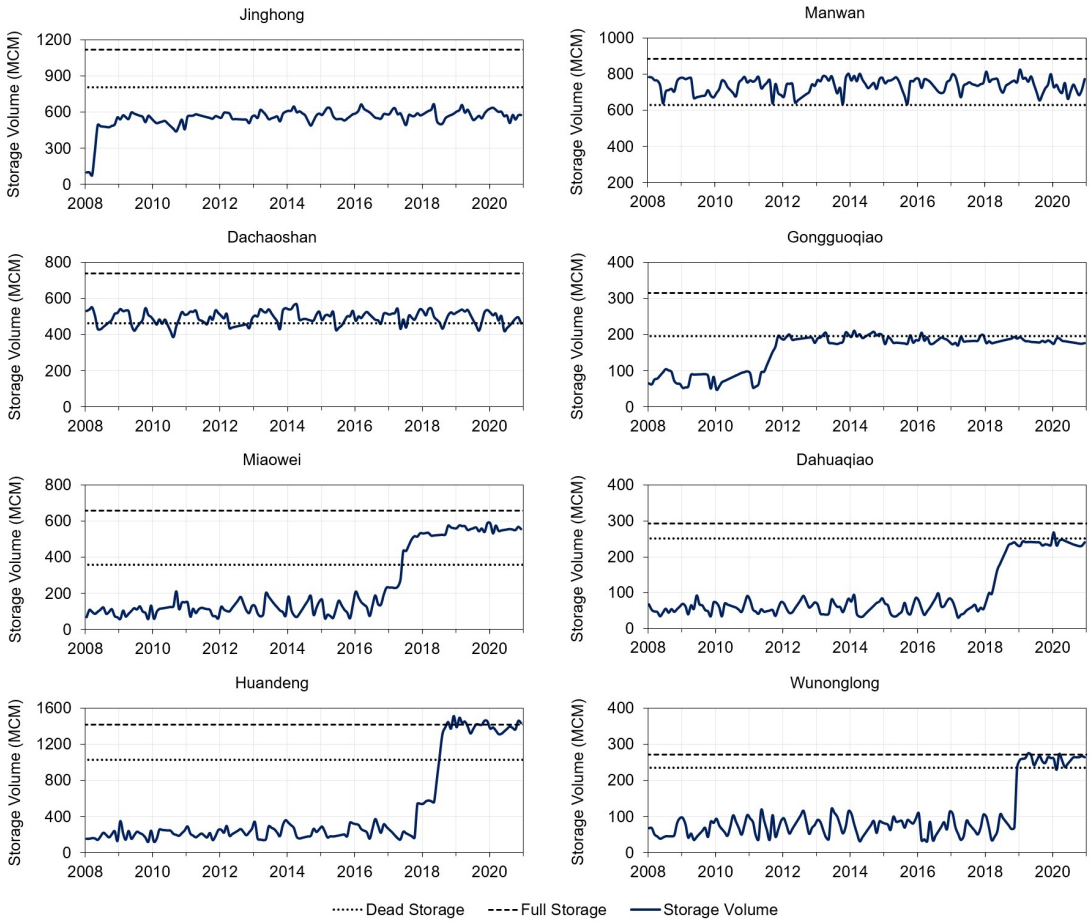

Bibliography

Abtew, SWossenu and Assefa M. Melesse (2014). "Transboundary rivers and the Nile". In: *Nile River Basin: Ecohydrological challenges, climate change and hydropolitics*. Ed. by Assefa M. Melesse, Wossenu Abtew, and Shimelis G. Setegn. Cham: Springer International Publishing, pp. 65–579. DOI: 10.1007/978-3-319-02720-3_28.

Ahmad, Shahryar K. et al. (2021). "Predicting the likely thermal impact of current and future dams around the world". In: *Earth's Future* 9.10, e2020EF001916. DOI: 10.1029/2020ef001916.

Ambec, Stefan, Ariel Dinar, and Daene McKinney (2013). "Water sharing agreements sustainable to reduced flows". In: *Journal of Environmental Economics and Management* 66.3, pp. 639–655. DOI: 10.1016/j.jeem.2013.06.003.

Amini, Abdulsalam et al. (2021). "Transboundary water resources conflict analysis using graph model for conflict resolution: A case study—Harirud River". In: *Discrete Dynamics in Nature and Society* 2021, p. 1720517. DOI: 10.1155/2021/1720517.

Arias, Mauricio E. et al. (2014). "Impacts of hydropower and climate change on drivers of ecological productivity of Southeast Asia's most important wetland". In: *Ecological Modelling* 272, pp. 252–263. DOI: 10.1016/j.ecolmodel.2013.10.015.

Avisse, Nicolas et al. (2017). "Monitoring small reservoirs' storage with satellite remote sensing in inaccessible areas". In: *Hydrology and Earth System Sciences* 21.12, pp. 6445–6459. DOI: 10.5194/hess-21-6445-2017.

Basheer, Mohammed et al. (2020). "Filling Africa's largest hydropower dam should consider engineering realities". In: *One Earth* 3.3, pp. 277–281. DOI: 10.1016/j.oneear.2020.08.015.

Beveridge, Claire, Faisal Hossain, and Matthew Bonnema (2020). "Estimating impacts of dam development and landscape changes on suspended sediment concentrations in the Mekong River Basin's 3S tributaries". In: *Journal of Hydrologic Engineering* 25.7, p. 05020014. DOI: 10.1061/(asce)he.1943-5584.0001949.

Bevington, Alexandre et al. (2018). "A review of free optical satellite imagery for watershed-scale landscape analysis". In: *Journal of Watershed Science and Management* 2.2. DOI: 10.22230/jwsm.2018v2n2a18.

Biancamaria, Sylvain, Dennis P. Lettenmaier, and Tamlin M. Pavelsky (2016). "The SWOT mission and its capabilities for land hydrology". In: *Remote Sensing and Water Resources*. Ed. by A. Cazenave et al. Cham: Springer International Publishing, pp. 117–147. DOI: 10.1007/978-3-319-32449-4_6.

Bierkens, Marc F. P. (2015). "Global hydrology 2015: State, trends, and directions". In: *Water Resources Research* 51.7, pp. 4923–4947. DOI: 10.1002/2015wr017173.

Binh, Doan Van, Sameh Kantoush, and Tetsuya Sumi (2020). "Changes to long-term discharge and sediment loads in the Vietnamese Mekong Delta caused by upstream dams". In: *Geomorphology* 353, p. 107011. DOI: 10.1016/j.geomorph.2019.107011.

Birkett, C. M. et al. (2011). "From Research to Operations: The USDA Global Reservoir and Lake Monitor". In: *Coastal altimetry*. Ed. by S. Vignudelli et al. Berlin: Springer, pp. 19–50. DOI: 10.1007/978-3-642-12796-0_2.

Birkinshaw, S. J. et al. (2010). "Using satellite altimetry data to augment flow estimation techniques on the Mekong River". In: *Hydrological Processes* 24.26, pp. 3811–3825. DOI: 10.1002/hyp.7811.

Biswas, Nishan Kumar, Faisal Hossain, Matthew Bonnema, Hyongki Lee, et al. (2021). "Towards a global Reservoir Assessment Tool for predicting hydrologic impacts and operating patterns of existing and planned reservoirs". In: *Environmental Modelling and Software* 140, p. 105043. DOI: 10.1016/j.envsoft.2021.105043.

Biswas, Nishan Kumar, Faisal Hossain, Matthew Bonnema, Modurodoluwa Adeyinka Okeowo, et al. (2019). "An altimeter height extraction technique for dynamically changing rivers of South and South-East Asia". In: *Remote Sensing of Environment* 221, pp. 24–37. DOI: 10.1016/j.rse.2018.10.033.

Bonnema, Matthew and Faisal Hossain (2017). "Inferring reservoir operating patterns across the Mekong Basin using only space observations". In: *Water Resources Research* 53.5, pp. 3791–3810. DOI: 10.1002/2016wr019978.

— (2019). "Assessing the potential of the Surface Water and Ocean Topography mission for reservoir monitoring in the Mekong River Basin". In: *Water Resources Research* 55.1, pp. 444–461. DOI: 10.1029/2018wr023743.

Bonnema, Matthew, Faisal Hossain, et al. (2020). "Hydropower's hidden transformation of rivers in the Mekong". In: *Environmental Research Letters* 15.4, p. 044017. DOI: 10.1088/1748-9326/ab763d.

Bonnema, Matthew, Safat Sikder, et al. (2016). "Understanding satellite-based monthly-to-seasonal reservoir outflow estimation as a function of hydrologic controls". In: *Water Resources Research* 52.5, pp. 4095–4115. DOI: 10.1002/2015wr017830.

Bose, Indira et al. (2021). "Developing a baseline characterization of river bathymetry and time-Varying height for Chindwin River in Myanmar using SRTM and Landsat data". In: *Journal of Hydrologic Engineering* 26.11, p. 05021030. DOI: 10.1061/(asce)he.1943-5584.0002126.

Busker, Tim et al. (2019). "A global lake and reservoir volume analysis using a surface water dataset and satellite altimetry". In: *Hydrology and Earth System Sciences* 23.2, pp. 669–690. DOI: 10.5194/hess-23-669-2019.

Chow, Ven Te (1959). *Open-channel Hydraulic*. New York: McGraw-Hill Book Company.

Chowdhury, AFM Kamal, Thanh Duc Dang, Arijit Bagchi, et al. (2020). "Expected benefits of Laos' hydropower development curbed by hydro-climatic variability and limited transmission capacity: opportunities to reform". In: *Journal of Water Resources Planning and Management* 146.10, p. 05020019. DOI: 10.1061/(asce)wr.1943-5452.0001279.

Chowdhury, AFM Kamal, Thanh Duc Dang, Hung T. T. Nguyen, et al. (2021). "The Greater Mekong's climate-water-energy nexus: How ENSO-triggered regional droughts affect power supply and CO_2 emissions". In: *Earth's Future* 9.3, e2020ef001814. DOI: 10.1029/2020ef001814.

Chuphal, Dipesh Singh and Vimal Mishra (2023). "Increased hydropower but with an elevated risk of reservoir operations in India under the warming climate". In: *iScience* 2589-0042, p. 105986. DOI: 10.1016/j.isci.2023.105986.

Dan, Li et al. (2012). "Hydrological projections of climate change scenarios over the 3H region of China: A VIC model assessment". In: *Journal of Geography Research* 117, p. D11102. DOI: 10.1029/2011jd017131.

Dang, Thanh Duc, AFM Kamal Chowdhury, and Stefano Galelli (2020). "On the representation of water reservoir storage and operations in large-scale hydrological models: Implications on model parameterization and climate change impact assessments". In: *Hydrology and Earth System Sciences* 24.1, pp. 397–416. DOI: 10.5194/hess-24-397-2020.

Dang, Thanh Duc, Thomas A. Cochrane, et al. (2016). "Hydrological alterations from water infrastructure development in the Mekong floodplains". In: *Hydrological Processes* 30.21, pp. 3824–3838. DOI: 10.1002/hyp.10894.

Dang, Thanh Duc, Dung Trung Vu, et al. (2020). "A software package for the representation and optimization of water reservoir operations in the VIC hydrologic model". In: *Environmental Modelling & Software* 126, p. 104673. DOI: 10.1016/j.envsoft.2020.104673.

Dawson, C. W., R. J. Abrahart, and L. M. See (2010). "HydroTest: Further development of a web resource for the standardised assessment of hydrological models". In: *Environmental Modelling & Software* 25.11, pp. 1481–1482. DOI: doi.org/10.1016/j.envsoft.2009.01.001.

Didan, Kamel and Armando Barreto Munoz (2019). *MODIS vegetation index user's guide (MOD13 Series)*. Vegetation Index and Phenology Lab, The University of Arizona. last access: 20 May 2021. URL: https://vip.arizona.edu/documents/MODIS/MODIS_VI_UsersGuide_09_18_2019_C61.pdf.

Ding, Ting and Hui Gao (2020). "The record-breaking extreme drought in Yunnan Province, Southwest China during spring-early summer of 2019 and possible causes". In: *Journal of Meteorological Research* 34, pp. 997–1012. DOI: 10.1007/s13351-020-0032-8.

Do, Pierre et al. (2020). "Exploring synergies in the water-food-energy nexus by using an integrated hydro-economic optimization model for the Lancang-Mekong River Basin". In: *Science of The Total Environment* 728, p. 137996. DOI: 10.1016/j.scitotenv.2020.137996.

Döll, P. et al. (2008). "Advances and visions in large-scale hydrological modelling: findings from the 11th Workshop on large-scale hydrological modelling". In: *Advances in Geosciences* 18, pp. 51–56. DOI: 10.5194/adgeo-18-51-2008.

Duan, Zheng and W. G. M. Bastiaanssen (2013). "Estimating water volume variations in lakes and reservoirs from four operational satellite altimetry databases and satellite imagery data". In: *Remote Sensing of Environment* 134, pp. 403–416. DOI: 10.1016/j.rse.2013.03.010.

Durand, M. et al. (2016). "An intercomparison of remote sensing river discharge estimation algorithms from measurements of river height, width, and slope". In: *Water Resources Research* 52.6, pp. 4527–4549. DOI: 10.1002/2015wr018434.

Efstratiadis, Andreas and Demetris Koutsoyiannis (2010). "One decade of multi-objective calibration approaches in hydrological modelling: A review". In: *Hydrological Sciences Journal* 55.1, pp. 58–78. DOI: 10.1080/02626660903526292.

Engineering ToolBox (2004). *Manning's Roughness Coefficients*. last access 22 December 2022. URL: https://www.engineeringtoolbox.com/mannings-roughness-d_799.html.

Eyler, Brian, Alan Basist, et al. (2020). *Mekong dam Monitor: Methods and Processes*. The Stimson Center. last access: 20 May 2021. URL: https://www.stimson.org/2020/mekong-dam-monitor-methods-and-processes/.

Eyler, Brian and Courtney Weatherby (2020). *New evidence: How China turned off the tap on the Mekong River*. The Stimson Center. last access: 20 May 2021. URL: https://www.stimson.org/2020/new-evidence-how-china-turned-off-the-mekong-tap/.

Flores-Anderson, Africa Ixmuca et al. (2019). *The SAR handbook: Comprehensive methodologies for forest monitoring and biomass estimation*. Huntsville, AL, USA: National Space Science and Technology Center. DOI: 10.25966/nr2c-s697.

Franchini, Marco and Michele Pacciani (1991). "Comparative analysis of several conceptual rainfall-runoff models". In: *Journal of Hydrology* 122.1-4, pp. 161–219. DOI: 10.1016/0022-1694(91)90178-k.

Funk, Chris et al. (2015). "The climate hazards infrared precipitation with stations—a new environmental record for monitoring extremes". In: *Scientific Data* 2.150066. DOI: 10.1038/sdata.2015.66.

Galelli, Stefano et al. (2022). "Opportunities to curb hydrological alterations via dam re-operation in the Mekong". In: *Nature Sustainability* 5, pp. 1058–1069. DOI: 10.1038/s41893-022-00971-z.

Gao, Huilin (2015). "Satellite remote sensing of large lakes and reservoirs: From elevation and area to storage". In: *Wiley Interdisciplinary Reviews: Water* 2.2, pp. 145–157. DOI: 10.1002/wat2.1065.

Gao, Huilin, Charon Birkett, and Dennis P. Lettenmaier (2012). "Global monitoring of large reservoir storage from satellite remote sensing". In: *Water Resources Research* 48.9, w09504. DOI: 10.1029/2012wr012063.

Gleason, Colin J. and Laurence C. Smith (2014). "Toward global mapping of river discharge using satellite images and at-many-stations hydraulic geometry". In: *The Proceedings of the National Academy of Sciences* 111.13, pp. 4788–4791. DOI: 10.1073/pnas.1317606111.

Grill, G. et al. (2019). "Mapping the world's free-flowing rivers". In: *Nature* 59, pp. 215–221. DOI: 10.1038/s41586-019-1111-9.

Grill, Günther, Camille Ouellet Dallaire, et al. (2014). "Development of new indicators to evaluate river fragmentation and flow regulation at large scales: A case study for the Mekong River Basin". In: *Ecological Indicators* 45, pp. 148–159. DOI: 10.1016/j.ecolind.2014.03.026.

Grill, Günther, Bernhard Lehner, et al. (2015). "An index-based framework for assessing patterns and trends in river fragmentation and flow regulation by global dams at multiple scales". In: *Environmental Research Letter* 10.1, pp. 145–157. DOI: 10.1088/1748-9326/10/1/015001.

Haddeland, I. et al. (2014). "Global water resources affected by human interventions and climate change". In: *Proceedings of the National Academy of Sciences of the United States of America* 111.9, pp. 3251–3256. DOI: 10.1073/pnas.1222475110.

Haddeland, Ingjerd, Thomas Skaugen, and Dennis P. Lettenmaier (2006). "Anthropogenic impacts on continental surface water fluxes". In: *Geophysical Research Letters* 33.8, p. l08406. DOI: 10.1029/2006gl026047.

Hagemann, M. W., C. J. Gleason, and M. T. Durand (2017). "BAM: Bayesian AMHG-Manning inference of discharge using remotely sensed stream width, slope, and height". In: *Water Resources Research* 53.11, pp. 9692–9707. DOI: 10.1002/2017wr021626.

Hanasaki, Naota, Shinjiro Kanae, and Taikan Oki (2006). "A reservoir operation scheme for global river routing models". In: *Journal of Hydrology* 327.1-2, pp. 22–41. DOI: 10.1016/j.jhydrol.2005.11.011.

Hansford, Mark R., Piret Plink-Björklund, and Evan R. Jones (2020). "Global quantitative analyses of river discharge variability and hydrograph shape with respect to climate types". In: *Earth-Science Reviews* 200, p. 102977. DOI: 10.1016/j.earscirev.2019.1029771.

Hecht, Jory S. et al. (2019). "Hydropower dams of the Mekong River Basin: A review of their hydrological impacts". In: *Journal of Hydrology* 568, pp. 285–300. DOI: 10.1016/j.jhydrol.2018.10.045.

Hipel, Keith W., D. Marc Kilgour, and Rami A. Kinsara (2019). "Strategic investigations of water conflicts in the Middle East". In: *Group Decision and Negotiation* 23, pp. 355–376. DOI: 10.1007/s10726-012-9325-3.

Hoang, Long P. et al. (2019). "The Mekong's future flows under multiple drivers: How climate change, hydropower developments and irrigation expansions drive hydrological changes". In: *Science of the Total Environment* 649, pp. 601–609. DOI: 10.1016/j.scitotenv.2018.08.160.

Hossain, Md. Shabbir and A. El-shafie (2013). "Intelligent systems in optimizing reservoir operation policy: A review". In: *Water Resources Management* 27.9, pp. 3387–3407. DOI: 10.1007/s11269-013-0353-9.

Hrachowitz, M. et al. (2013). "A decade of Predictions in Ungauged Basins (PUB) — a review". In: *Hydrological Sciences Journal* 58.6, pp. 1198–1255. DOI: 10.1080/02626667.2013.803183.

Hua, Wei, Naichen Ke, and Yaqiong Dai (2018). *Comprehensive Study on Reservoir-induced Seismicity in the Xiaowan Reservoir, Yunnan Province, China*. 2018 Southern California Earthquake Center Annual Meeting. URL: https://www.scec.org/publication/8277.

Huang, Qi et al. (2020). "Daily continuous river discharge estimation for ungauged basins using a hydrologic model calibrated by satellite altimetry: Implications for the SWOT mission". In: *Water Resources Research* 56.7, e2020wr027309. DOI: 10.1029/2020wr027309.

IRN (2002). *China's Upper Mekong dams endanger millions downstream*. International Rivers Network. last access: 20 May 2021. URL: https://www.irn.org/files/pdf/mekong/MekongFactSheet2002.pdf.

— (2014). *The environmental and social impacts of Lancang dams*. International Rivers Network. last access: 20 May 2023. URL: https://archive.internationalrivers.org/sites/default/files/attached-files/ir_lancang_dams_researchbrief_final.pdf.

Johnson, Kay (2020). *China commits to share year-round water data with Mekong River Commission*. Reuters. last access 22 December 2022. URL: https://www.reuters.com/article/us-mekong-river/china-commits-to-share-year-round-water-data-with-mekong-river-commission-idINKBN277135.

JPL (n.d.). *SWOT: Surface Water and Ocean Topography*. last access 22 December 2022. URL: https://swot.jpl.nasa.gov/.

Kabir, Tamanna, Yadu Pokhrel, and Farshid Felfelani (2022). "On the precipitation-induced uncertainties in process-based hydrological modeling in the Mekong River Basin". In: *Water Resources Research* 58.2, e2021wr030828. DOI: 10.1029/2021wr030828.

Kallio, Marko and Amy Fallon (2020). *Critical Nature: Are China's dams on the Mekong causing downstream drought? The importance of scientific debate*. The Center for Social Development Studies. last access: 20 May 2021. URL: https://www.csds-chula.org/publications/2020/4/28/critical-nature-are-chinas-dams-on-the-mekong-causing-downstream-drought-the-importance-of-scientific-debate.

Kattelus, Mirja et al. (2015). "China's southbound transboundary river basins: A case of asymmetry". In: *Water International* 40.1, pp. 113–138. DOI: 10.1080/02508060.2014.980029.

Keovilignavong, Oulavanh, Tuong Huy Nguyen, and Philip Hirsch (2021). "Reviewing the causes of Mekong drought before and during 2019–20". In: *International Journal of Water Resources Development* 0.0, pp. 1–21. DOI: 10.1080/07900627.2021.1967112.

Khan, Sadiq I. et al. (2012). "Microwave satellite data for hydrologic modeling in ungauged basins". In: *IEEE Geoscience and Remote Sensing Letters* 9.44, pp. 663–667. DOI: 10.1109/lgrs.2011.2177807.

Kondolf, G. Mathias et al. (2018). "Changing sediment budget of the Mekong: Cumulative threats and management strategies for a large river basin". In: *Science of The Total Environment* 625, pp. 114–134. DOI: 10.1016/j.scitotenv.2017.11.361.

Lettenmaier, Dennis P. et al. (2015). "Inroads of remote sensing into hydrologic science during the WRR era". In: *Water Resources Research* 51.9, pp. 7309–7342. DOI: 10.1002/2015WR017616.

Li, Yao et al. (2019). "Deriving high-resolution reservoir bathymetry from ICESat-2 prototype photon-counting lidar and Landsat imagery". In: *IEEE Transactions on Geoscience and Remote Sensing* 57.10, pp. 7883–7893. DOI: 10.1109/tgrs.2019.2917012.

Liang, Xu et al. (2014). "A simple hydrologically based model of land surface water and energy fluxes for general circulation models". In: *Journal of Geophysical Research: Atmospheres* 99.D7, pp. 14415–14428. DOI: 10.1029/94jd00483.

Liu, Benxi et al. (2018). "Hydropower curtailment in Yunnan Province, southwestern China: Constraint analysis and suggestions". In: *Renewable Energy* 121, pp. 700–711. DOI: 10.1016/j.renene.2018.01.090.

Liu, Ganming et al. (2015). "Discharge and water-depth estimates for ungauged rivers: Combining hydrologic, hydraulic, and inverse modeling with stage and water-area measurements from satellites". In: *Water Resources Research* 51.8, pp. 6017–6035. DOI: 10.1002/2015wr016971.

Liu, Kuan-Ting et al. (2016). "Assessment of the impact of reservoirs in the Upper Mekong River using satellite radar altimetry and remote sensing imageries". In: *Remote Sensing* 8.5, p. 367. DOI: 10.3390/rs8050367.

Liu, Yang et al. (2010). "Building topographic subspace model with transfer learning for sparse representation". In: *Neurocomputing* 73.10, pp. 1662–1668. DOI: 10.1016/j.neucom.2009.11.041.

Llamosas, Cecilia and Benjamin K. Sovacool (2021). "The future of hydropower? A systematic review of the drivers, benefits and governance dynamics of transboundary dams". In: *Renewable and Sustainable Energy Reviews* 137.1364-0321, p. 110495. DOI: 10.1016/j.rser.2020.110495.

Lohmann, Dag, Ralph Nolte-Holube, and Ehrhard Raschke (1996). "A large-scale horizontal routing model to be coupled to land surface parametrization schemes". In:

Tellus A: Dynamic Meteorology and Oceanography 48.5, pp. 708–721. DOI: 10.3402/tellusa.v48i5.12200.

Lohmann, Dag, Ehrhard Raschke, et al. (1998). "Regional scale hydrology: I. Formulation of the VIC-2L model coupled to a routing model". In: *Hydrological Sciences Journal* 43.1, pp. 131–141. DOI: 10.1080/02626669809492107.

Lv, Xiaolong and Shichun Chi (2018). "Strain analysis of the Nuozhadu high rockfill dam during Initial impoundment". In: *Mathematical Problems in Engineering* 2018.7291473. DOI: 10.1155/2018/7291473.

Ly, Kongmeng, Graciela Metternicht, and Lucy Marshall (2022). "Transboundary river basins: Scenarios of hydropower development and operation under extreme climate conditions". In: *Science of The Total Environment* 803.0048-9697, p. 149828. DOI: 10.1016/j.scitotenv.2021.149828.

Madson, Austin and Yongwei Shen (2020). "Reservoir induced deformation analysis for several filling and operational scenarios at the Grand Ethiopian Renaissance dam impoundment". In: *Remote Sensing* 12.11, p. 1886. DOI: doi.org/10.3390/rs12111886.

Mager, Ute (2015). *International water law: Global developments and regional examples*. Heidelberg, Germany: Jedermann-Verlag GmbH.

Markert, Kel N. et al. (2019). "AltEx: An open source web application and toolkit for accessing and exploring altimetry datasets". In: *nvironmental Modelling & Software* 117, pp. 164–175. DOI: 10.1016/j.envsoft.2019.03.021.

McCabe, Matthew F. et al. (2017). "The future of Earth observation in hydrology". In: *Hydrology and Earth System Sciences* 21.7, pp. 3879–3914. DOI: 10.5194/hess-21-3879-2017.

McCracken, Melissa and Aaron T. Wolf (2019). "Updating the register of international river basins of the world". In: *International Journal of Water Resources Development* 35.5, pp. 732–821. DOI: 10.1080/07900627.2019.1572497.

MRC (2009). *The flow of the Mekong*. Vientiane, Lao PDR: Mekong River Commission Secretariat.

— (2020a). *Sub-basins, major rivers and evaluation of the UMB in China*. Mekong River Commission. last access: 20 May 2021. URL: https://www.mrcmekong.org/our-work/topics/hydropower/.

— (2020b). *Understanding the Mekong River's hydrological conditions: A brief commentary note on the "Monitoring the quantity of water flowing through the Upper Mekong Basin under natural (unimpeded) conditions" study by Alan Basist and Claude Williams (2020)*. Vientiane, Lao PDR: Mekong River Commission Secretariat.

Mulat, Asegdew and Semu Moges (2014). "Filling option assessments for proposed reservoirs in Abbay (Upper Blue Nile) River Basin to minimize impacts on energy generation of downstream reservoirs". In: *Open Journal of Renewable Energy and Sustainable Development* 2014, pp. 22–35. DOI: 10.15764/resd.2014.01003.

Nazemi, A. and H. S. Wheater (2015a). "On inclusion of water resource management in Earth system models - Part 1: Problem definition and representation of water demand". In: *Hydrology and Earth System Sciences* 19.1, pp. 33–61. DOI: 10.5194/hess-19-33-2015.

— (2015b). "On inclusion of water resource management in Earth system models - Part 2: Representation of water supply and allocation and opportunities for improved modeling". In: *Hydrology and Earth System Sciences* 19.1, pp. 63–90. DOI: 10.5194/hess-19-63-2015.

Nguyen, Hung T T et al. (2020). "Coherent streamflow variability in Monsoon Asia over the past eight centuries—links to oceanic drivers". In: *Water Resources Research* 56.12, e2020wr027883. DOI: 10.1029/2020wr027883.

Papa, Fabrice et al. (2012). "Ganga-Brahmaputra river discharge from Jason-2 radar altimetry: An update to the long-term satellite-derived estimates of continental freshwater forcing flux into the Bay of Bengal". In: *Journal of Geophysical Research* 117.c11, p. c11021. DOI: 10.1029/2012jc008158.

Park, Daeryong and Momcilo Markus (2014). "Analysis of a changing hydrologic flood regime using the Variable Infiltration Capacity model". In: *Journal of Hydrology* 515, pp. 627–280. DOI: 10.1016/j.jhydrol.2014.05.004.

Pearse-Smith, Scott W. D. (2014). "'Water war' in the Mekong Basin?" In: *Asia Pacific Viewpoint* 53.2, pp. 6147–162. DOI: 10.1111/j.1467-8373.2012.01484.x.

Pekel, Jean-Francois et al. (2016). "High-resolution mapping of global surface water and its long-term changes". In: *Nature* 540, pp. 418–422. DOI: 10.1038/nature20584.

Petersen-Perlman, Jacob D., Jennifer C. Veilleux, and Aaron T. Wolf (2017). "International water conflict and cooperation: Challenges and opportunities". In: *42* 2, pp. 105–120. DOI: 10.1080/02508060.2017.1276041.

Pianosi, Francesca et al. (2016). "Sensitivity analysis of environmental models: A systematic review with practical workflow". In: *Environmental Modelling & Software* 79, pp. 214–232. DOI: 10.1016/j.envsoft.2016.02.008.

Pickens, Amy H. et al. (2020). "Mapping and sampling to characterize global inland water dynamics from 1999 to 2018 with full Landsat time-series". In: *Remote Sensing of Environment* 243, p. 111792. DOI: 10.1016/j.rse.2020.111792.

Piman, T. et al. (2013). "Assessment of flow changes from hydropower development and operations in Sekong, Sesan, and Srepok Rivers of the Mekong Basin". In: *ournal of Water Resources Planning and Management* 139.6, pp. 723–732. DOI: 10.1061/(asce)wr.1943-5452.0000286.

Räsänen, Timo A. et al. (2017). "Observed river discharge changes due to hydropower operations in the Upper Mekong Basin". In: *Journal of Hydrology* 545, pp. 28–41. DOI: 10.1016/j.jhydrol.2016.12.023.

Reed, P. M. et al. (2013). "Evolutionary multiobjective optimization in water resources: The past, present, and future". In: *Advances in Water Resources* 51, pp. 438–456. DOI: doi.org/10.1016/j.advwatres.2012.01.005.

Ren-Jun, Zhao (1992). "The Xinanjiang model applied in China". In: *Journal of Hydrology* 135.1-4, pp. 371–381. DOI: 10.1016/0022-1694(92)90096-e.

Ryan, Jonathan C. et al. (2020). "Global characterization of inland water reservoirs using ICESat-2 altimetry and climate reanalysis". In: *Geophysical Research Letters* 47.17, e2020gl088543. DOI: 10.1029/2020gl088543.

Sabo, J. L. et al. (2017). "Designing river flows to improve food security futures in the Lower Mekong Basin". In: *Science* 358.6368, eaao1053. DOI: 10.1126/science.aao1053.

Sale, Michael J., E. Downey Brill Jr., and Edwin E. Herricks (1982). "An approach to optimizing reservoir operation for downstream aquatic resources". In: *Water Resources Research* 18.4, pp. 705–712. DOI: doi.org/10.1029/wr018i004p00705.

Salehi, Hamid et al. (2021). "Spatial and temporal resolution improvement of actual evapotranspiration maps using Landsat and MODIS data fusion". In: *Frontiers in Environmental Science* 9, pp. 2296–665X. DOI: 10.3389/fenvs.2021.795287.

Salomonson, Vincent V., William Barnes, and Edward J. Masuoka (2006). "Introduction to MODIS and an overview of associated activities". In: *Earth science satellite remote sensing: Vol. 1: Science and instruments*. Ed. by John J. Qu et al. Heidelberg, Berlin: Springer, pp. 12–32. DOI: 10.1007/978-3-540-37293-6_2.

Schmitt, Rafael J. P. et al. (2019). "Planning dam portfolios for low sediment trapping shows limits for sustainable hydropower in the Mekong". In: *Science Advances* 5.10, eaaw2175. DOI: 10.1126/sciadv.aaw2175.

Schwatke, C. et al. (2015). "DAHITI – an innovative approach for estimating water level time series over inland waters using multi-mission satellite altimetry". In: *Hydrology and Earth System Sciences* 19.10, pp. 4345–4364. DOI: 10.5194/hess-19-4345-2015.

Sheffield, J. et al. (2018). "Satellite remote sensing for water resources management: Potential for supporting sustainable development in data-poor regions". In: *Water Resources Research* 54.12, pp. 9724–9758. DOI: 10.1029/2017WR022437.

Shin, Sanghoon et al. (2020). "High resolution modeling of river-floodplain-reservoir inundation dynamics in the Mekong River Basin". In: *Water Resources Research* 56.5, e2019wr026449. DOI: 10.1029/2019wr026449.

Siala, Kais et al. (2021). "Solar energy and regional coordination as a feasible alternative to large hydropower in Southeast Asia". In: *Nature Communications*. DOI: 10.1038/s41467-021-24437-6.

Soukhaphon, Akarath, Ian G. Baird, and Zeb S. Hogan (2021). "The impacts of hydropower dams in the Mekong River Basin: A review". In: *Water* 13.3, p. 256. DOI: 10.3390/w13030265.

Steyaert, Jennie C. et al. (2022). "ResOpsUS, a dataset of historical reservoir operations in the contiguous United States". In: *Scientific Data* 9.1, pp. 1–8. DOI: 10.1038/s41597-022-01134-7.

Sun, Wenchao et al. (2018). "Calibrating a hydrological model in a regional river of the Qinghai–Tibet plateau using river water width determined from high spatial resolution satellite images". In: *Remote Sensing of Environment* 214, pp. 100–114. DOI: 10.1016/j.rse.2018.05.020.

Tadono, Takeo et al. (2015). "Status of "ALOS World 3D (AW3D)" global DSM generation". In: *2015 IEEE International Geoscience and Remote Sensing Symposium (IGARSS)*, pp. 3822–3825. DOI: 10.1109/IGARSS.2015.7326657.

Tarpanelli, Angelica et al. (2022). "Water resources in Africa: The role of earth observation data and hydrodynamic modeling to derive river discharge". In: *Surveys in Geophysics*, pp. 1–26. DOI: 10.1007/s10712-022-09744-x.

Tiezzi, Shannon (2016). *Facing Mekong drought, China release water from Yunnan Dam*. The Diplomat. last access: 20 January 2022. URL: https://thediplomat.com/2016/03/facing-mekong-drought-china-to-release-water-from-yunnan-dam/.

Todini, E. (1996). "The ARNO rainfall—runoff model". In: *Journal of Hydrology* 175.1-4, pp. 339–382. DOI: 10.1016/S0022-1694(96)80016-3.

Tortini, Riccardo et al. (2020). "Satellite-based remote sensing data set of global surface water storage change from 1992 to 2018". In: *Earth System Science Data* 12.2, pp. 1141–1151. DOI: 10.5194/essd-12-1141-2020.

Turner, Sean W. D., Kenji Doering, and Nathalie Voisin (2020). "Data-driven reservoir simulation in a large-scale hydrological and water resource model". In: *Water Resources Research* 56.10, e2020WR027902. DOI: 10.1029/2020wr027902.

UN (2023). *Status of treaties: Convention on the aw of the Non-Navigational Uses of International Watercourses*. United Nations Treaty Collection. last access: 20 February 2023. URL: https://treaties.un.org/Pages/ViewDetails.aspx?src=IND%5C&mtdsg_no=XXVII-12&chapter=27.

— (n.d.). *UNWC's global relevance in South and East Asia*. UN Watercourses Convention Online User's Guide. last access: 20 February 2023. URL: https://www.unwatercoursesconvention.org/global-relevance/south-and-east-asia/.

UNEP (2002). *Atlas of international freshwater agreements*. United Nations Environment Programme. last access: 20 February 2023. URL: https://wedocs.unep.org/20.500.11822/8182.

USGS (2009). *Shuttle Radar Topography Mission (SRTM)*. USGS Publications Warehouse. DOI: 10.3133/fs20093087.

Vegad, Urmin and Vimal Mishra (2022). "Ensemble streamflow prediction considering the influence of reservoirs in India". In: *Hydrology and Earth System Sciences* 26.24, pp. 6361–6378. DOI: 10.5194/hess-26-6361-2022.

Vignudelli, Stefano et al. (2019). "Water surface elevation in coastal and inland waters using satellite radar altimetry". In: *Extreme hydroclimatic events and multivariate hazards in a changing environment*. Ed. by Viviana Maggioni and Christian Massari. Newyork: Elsevier, pp. 87–127. DOI: 10.1016/B978-0-12-814899-0.00004-3.

Vliet, Michelle T. H. van et al. (2016). "Power-generation system vulnerability and adaptation to changes in climate and water resources". In: *Nature Climate Change* 6.4, pp. 375–380. DOI: 10.1038/nclimate2903.

Vu, Dung Trung et al. (2022). "Satellite observations reveal 13 years of reservoir filling strategies, operating rules, and hydrological alterations in the Upper Mekong River basin". In: *Hydrology and Earth System Sciences* 26.9, pp. 2345–2364. DOI: 10.5194/hess-26-2345-2022.

Wagener, Thorsten and Francesca Pianosi (2019). "What has Global Sensitivity Analysis ever done for us? A systematic review to support scientific advancement and to inform policy-making in earth system modelling". In: *Earth-Science Reviews* 194.0012-8252, pp. 1–18. DOI: 10.1016/j.earscirev.2019.04.006.

Wang, Jida et al. (2022). "GeoDAR: Georeferenced global Dams And Reservoirs dataset for bridging attributes and geolocations". In: *Earth System Science Data* 14, pp. 1869–1899. DOI: 10.5194/essd-14-1869-2022.

Warner, Jeroen and Neda Zawahri (2012). "Hegemony and asymmetry: Multiple-chessboard games on transboundary rivers". In: *International Environmental Agreements: Politics, Law and Economics* 12.3, pp. 215–229. DOI: 10.1007/s10784-012-9177-y.

Wei, Jing et al. (2021). "News media coverage of conflict and cooperation dynamics of water events in the Lancang-Mekong River Basin". In: *Hydrology and Earth System Sciences* 25.3, pp. 1603–1615. DOI: 10.5194/hess-25-1603-2021.

Wi, Sungwook et al. (2017). "A user-friendly software package for VIC hydrologic model development". In: *Environmental Modelling & Software* 98, pp. 35–53. DOI: 10.1016/j.envsoft.2017.09.006.

Williams, Jessica M. (2020). "Is three a crowd? River basin institutions and the governance of the Mekong River". In: *International Journal of Water Resources Development*. DOI: 10.1080/07900627.2019.1700779.

Winemiller, K. O. et al. (2016). "Balancing hydropower and biodiversity in the Amazon, Congo, and Mekong". In: *Science* 351.6269, pp. 128–129. DOI: 10.1126/science.aac7082.

WLE Mekong (2016). *Dams in the Irrawaddy and Salween River Basins: Commissioned, under Construction and planned dams*. Vientiane, Lao PDR: CGIAR Research Program on Water, Land and Ecosystems. last access 22 February 2023. URL: https://hdl.handle.net/10568/83002.

— (n.d.). *Greater Mekong dam observatory*. last access 22 December 2022. URL: https://wle-mekong.cgiar.org/changes/our-research/greater-mekong-dams-observatory/.

Wolf, Aaron T., Annika Kramer, et al. (2005). "Managing water conflict and cooperation". In: *State of the World 2005: Redefining global security*. Ed. by Linda Starke. Newyork: W. W. Norton & Company, pp. 80–99.

Wolf, Aaron T., Kerstin Stahl, and Marcia F. Macomber (2003). "Conflict and cooperation within international river basins: The importance of institutional capacity." In: *Water Resources Update* 125, pp. 31–40.

Wu, Mingquan et al. (2016). "An improved high spatial and temporal data fusion approach for combining Landsat and MODIS data to generate daily synthetic Landsat imagery". In: *Information Fusion* 31, pp. 14–25. DOI: 10.1016/j.inffus.2015.12.005.

Xue, Xianwu et al. (2015). "New multisite cascading calibration approach for hydrological models: Case study in the Red River Basin using the VIC model". In: *Journal of Hydrologic Engineering* 21.2, p. 05015019. DOI: 10.5194/hess-23-3735-2019.

Yeste, Patricio et al. (2020). "Integrated sensitivity analysis of a macroscale hydrologic model in the north of the Iberian Peninsula". In: *Journal of Hydrology* 590.0022-1694, p. 125230. DOI: 10.1016/j.jhydrol.2020.125230.

Yu, Yang et al. (2019). "Effects of hydrologic conditions and reservoir operation on transboundary cooperation in the Lancang-Mekong River Basin". In: *Journal of Water Resources Planning and Management* 145.6, p. 04019020. DOI: 10.1061/(asce)wr.1943-5452.0001075.

Yu, Yuanhe et al. (2020). "Drought monitoring in Yunnan Province based on a TRMM precipitation product". In: *Natural Hazards* 104.3, pp. 2369–2387. DOI: 10.1007/s11069-020-04276-2.

Yun, Xiaobo et al. (2020). "Impacts of climate change and reservoir operation on streamflow and flood characteristics in the Lancang-Mekong River Basin". In: *Journal of Hydrology* 590, p. 125472. DOI: 10.1016/j.jhydrol.2020.125472.

Zaniolo, Marta et al. (2021). "When timing matters—misdesigned dam filling impacts hydropower sustainability". In: *Nature Communications* 12.1, p. 3056. DOI: 10.1038/s41467-021-23323-5.

Zhai, Ke et al. (2015). "Comparison of surface water extraction performances of different classic water indices using OLI and TM imageries in different situations". In: *Geospatial Information Science* 18.1, pp. 34–42. DOI: 10.1080/10095020.2015.1017911.

Zhang, Shuai and Huilin Gao (2020). "Using the digital elevation model (DEM) to improve the spatial coverage of the MODIS based reservoir monitoring network in South Asia". In: *Remote Sensing* 12.5, p. 745. DOI: 10.3390/rs12050745.

Zhang, Shuai, Huilin Gao, and Bibi S. Naz (2014). "Monitoring reservoir storage in South Asia from multisatellite remote sensing". In: *Water Resources Research* 50.11, pp. 8927–8943. DOI: 10.1002/2014wr015829.

Zhang, Ying, Solomon Tassew Erkyihum, and Paul Block (2016). "Filling the GERD: Evaluating hydroclimatic variability and impoundment strategies for Blue Nile riparian countries". In: *Water International* 41.4, pp. 593–610. DOI: 10.1080/02508060.2016.1178467.

Zhao, Gang and Huilin Gao (2018). "Automatic correction of contaminated images for assessment of reservoir surface area dynamics". In: *Geophysical Research Letters* 45.12, pp. 6092–6099. DOI: 10.1029/2018gl078343.